Distribution Agreement

Signature:

Christella K. Gordon

Date

Nucleation Pathways of Peptide Assemblies and Their Context in Alzheimer's Disease

By

Christella K. Gordon

Doctor of Philosophy

Chemistry

David G. Lynn, PhD
Advisor

Christine M. Dunham, PhD
Committee Member

Vince Conticello, PhD
Committee Member

Accepted:

Kimberly Jacob Arriola, Ph.D.
Dean of the James T. Laney School of Graduate Studies

Date

Nucleation Pathways of Peptide Assemblies and Their Context in Alzheimer's Disease

By

Christella K. Gordon

B.Sc., Emory University, 2017

Advisor: David G. Lynn, PhD

An abstract of A dissertation submitted to the Faculty of the James T. Laney School of Graduate Studies of Emory University in partial fulfillment of the requirements for the degree of

Doctor of Philosophy in Chemistry

2023

Abstract

Nucleation Pathways of Peptide Assemblies and Their Context in Alzheimer's Disease

By

Christella K. Gordon

As of 2022, more than 1 in 10 Americans who are 65 years of age or older suffer from AD-related dementia, and a long-term, multinational study spanning 3 decades revealed that the incidence of Alzheimer's Disease (AD) -related dementia diagnosis has more than doubled within the time range in which the study was conducted.[1-3] The increased prevalence will ultimately put an immense strain on healthcare systems at a global scale; however, despite the vast research to inform how the disease is initiated and spread across the brain, little improvements on therapeutic solutions have been made. Conflicting observations of otherwise potential AD biomarkers, namely Aβ42 and tau plaques, in animals excluding humans, studying the pathogenic transformation in nonhuman primates and other mammals could leave an incomplete picture of a disease model.

The works described here sought to eliminate the discrepancy between animal models and humans with respect to modeling AD from its earliest manifestation by using brain organoids and to elucidate disease-relevant biopolymer associations that result in AD-linked paracrystalline assemblies. Organoids are an emerging tool that could mimic biological functions of their designated target organ and could be derived from human somatic cells, retaining all of the human donor's genes. This full genetic retention makes organoids a promising modeling tool which could bridge the gap between animal and human studies. Brain organoids were grown alongside protease- and detergent-resistant AD brain tissue-derived isolates, resulting in both genotypic and phenotypic alterations that mirrored AD-like changes in the brain. Further analysis of these isolates revealed that there were strong mutualistic associations between Aβ42 and tau, which further support the amyloid cascade hypothesis.

Lastly, the observations made in assemblies consisting of minimal Aβ42 and tau models revealed that cross-strand peptide associations could be modulated by introducing small amounts of mature assemblies as seed. The overall interactions are also highly sensitive to structural intricacies within the seed. Similarly, while charge complementarity is a main driver of cooperative, template-directed peptide-DNA interactions, the charge-ordering of a DNA template could dictate the entire assembly pathway, which produced distinct paracrystalline morphologies.

1. *2022 Alzheimer's disease facts and figures.* Alzheimer's & Dementia, 2022. **18**(4): p. 700-789.
2. Tahami Monfared, A.A., et al., *Alzheimer's Disease: Epidemiology and Clinical Progression.* Neurology and Therapy, 2022. **11**(2): p. 553-569.
3. Li, X., et al., *Global, regional, and national burden of Alzheimer's disease and other dementias, 1990–2019.* Frontiers in Aging Neuroscience, 2022. **14**.

Nucleation Pathways of Peptide Assemblies and Their Context in Alzheimer’s Disease

By

Christella K. Gordon

B.Sc., Emory University, 2017

Advisor: David G. Lynn, PhD

A dissertation submitted to the Faculty of the James T. Laney School of Graduate Studies of Emory University in partial fulfillment of the requirements for the degree of

Doctor of Philosophy in Chemistry

2023

Acknowledgements

I do not know where to begin, but I know I have so many people to thank. While my journey through graduate school was not easy (not everyone can say they went through graduate school during a global pandemic and finish at the precipice of a potential economic collapse after all), I was fortunate to have a huge support network from all around the world. Having a global distribution of supportive friends allowed me the opportunity to complain about graduate school and contemplate back-up plans 24/7. Jokes aside, the following paragraphs are not an exhaustive list of everyone who has contributed to my success, but it is a start.

First and foremost, I would like to thank Dr. David "Dave" Lynn for believing in me since my undergraduate years in his lab. Through the 7 years we have had together, Dave has been one of my biggest supporters despite everything we have faced. I am so grateful for all the Twix, the advice to seek out mental health resources, and the investment that you have for my professional and personal development all these years.

Second, I would like to thank my committee members, Dr. Christine Dunham and Dr. Vince Conticello. Christine has served as a wonderful role model to look up to, and Vince always seems to give unique insight to peptide assembly pathways during my annual exams.

Third, I want to thank all my former and current undergraduate students (Seth Young, Nicolas Ingle, Regina Luu, Alexis Roberson, George Poppitz, Ethan Veinbachs) for allowing me to be a part of their journeys. It has been an honor to mentor you all, and I am so excited to see where you go next.

I would also like to thank the late Dr. Arthur “Art” McCanna for teaching me all things electron microscopy. I am lucky to have been able to learn from such a talented microscopist, and I have missed catching up with him about our furry, four-legged friends.

While much of the last 5 years of my life was spent within the walls of the Emerson chemistry building, I have also built a colorful life outside of it, where I garnered a majority of the support I needed to accomplish this phase of my life.

I want to thank my husband, Yong Kim, for foregoing a lot of things because of my hectic schedule ruled by graduate school. I know we have had to put some of our lives on pause to accommodate my degree, and I am forever grateful. Thank you for making sure I don’t go to sleep hungry even though I am always too tired to take care of myself and for making sure our animals are happy and healthy. In that same vein, I would also like to thank my late mother-in-law, Myong Toups, for taking care of me the way a mother would with her daughter, from packing my lunches, preparing dinner, and even through my first encounter with COVID. 어머님 감사해요. 언젠가 꼭 만나고싶어요.

I also want to thank the best brothers I never had: Dr. Anthony Sementilli, Dr. Youngsun Kim, and Dr. Shengyuan Wang. Anthony, thank you for imparting so much knowledge on how to troubleshoot the HPLC as well as to survive graduate school. You have made science a lot less scary. Youngsun, thank you for always being willing to join in on my adventures, whether it was to eat at a different burger place every Friday or to go to a conference in Korea. Thank you for always giving me a reality check any time I complain about being a baby. Sheng, thank you for all your sage advice, as my biochemistry TA, my colleague, and my friend. I’m so grateful to be your powerlifting partner and your troubleshooting buddy all these years.

Additionally, I want to thank Alexis Blake, Alexia Prokopik, Sara Gebre, and Victoria “Torie” Snider. Alexis, thank you for always being positive and willing to bounce ideas together. Some of my fondest memories was to have ideation sessions with you, whether it was for my annual exams or yours. You are such a stellar scientist and a beautiful woman, and I wish I could give you the world. Alexia, thank you for sticking by me since college. It is so rare for two friends to go through college and graduate school together. While time and circumstances have definitely tested our relationship, I am still excited for you and your success, in spite of all the things that you have faced. We both know our lives are more complicated than they should have been, but here we are! Sara, thank you for all the light and laughter that you have brought throughout our friendship. Graduate school, as you and I both know, is tough and has many dark paths, but you somehow always bring out the best in me when we are together, between binging Korean drama and going to seminars for free food. Torie, thank you for being such a great big sister that I wish I had. I always walk away with a feeling of reassurance whenever I come to you with my problems, and I can’t thank you enough.

I also want to thank Drs. Phil and Raquel Segre for being my surrogate parents. Not everyone gets to say that their professor and his family witnessed their elopement! Thank you for letting Yong and me be a part of your lives. Thank you as well to Dr. Nichole Powell for being the best cheerleader an academic could ever wish for. I am so grateful for all the academic opportunities you have offered me throughout my career!

Thank you to everyone at Vertical Joe's and Stone Summit Climbing Gym for keeping me mentally and physically healthy.

Lastly, thank you to my furry friends – Daisy, Nori, and Goliath. Daisy, especially, has gone through so much with me and has been a consistent light in even my darkest nights. I could not have asked for better companions.

Table of Contents

Chapter 1: Development of alternative, minimalistic model for Alzheimer's Disease....... 1

Chapter 1.1: Nucleation in the context of Alzheimer's Disease 4

Chapter 1.2: Challenges to modeling disease – finding an animal model 5

Chapter 1.3: Understanding general rules that drive biopolymer interactions 7

Chapter 1.4: Modeling AD pathology using iPSC technology 8

Chapter 1.5: Cortical organoids could recapitulate AD-like phenomena 11

Chapter 1.6: Characterization of tissue-derived aggregates.. 15

Chapter 1.9: Probing possible Aβ/tau interactions *in vitro* 17

Chapter 1.10: Identification of possible apolipoprotein complexes in brain aggregates 24

Conclusion 27

Materials and Methods 28

References 37

Chapter 2: Two-step nucleation in paracrystalline assemblies 43

Chapter 2.1: Intrinsically disordered proteins as an extension of Anfinsen's Dogma . 43

Chapter 2.2: Limiting conformational space for sampling 46

Chapter 2.3: Stabilizing a nucleus 47

References 53

Chapter 3: Generalized rules for peptide assemblies as informed by disease-relevant peptides 55

Chapter 3.1: Energetic contributions regulating cross-β assembly 55

Chapter 3.2: The assembly pathway 57

Chapter 3.3: Template-directed co-assembly 59

Chapter 3.4: Generalization of electrostatic complementarity at the leaflet interface 62

Conclusion 66

Materials and methods 67

Chapter 4: Polyanion order controls liquid-to-solid phase transition in peptide/nucleic acid co-assembly 74

Chapter 4.1: Oligonucleotide diversity in biomolecular condensates 74

Chapter 4.2: Double-stranded DNA more effectively templates cross-β peptide assembly 77

Chapter 4.3: Electrostatic ordering underlies template effectiveness 80

Chapter 4.4: Propagation of cross-β co-assemblies is sensitive to electrostatic interference 82

Chapter 4.5: Seeding with quadruplex DNA/peptide chimeras 84

Conclusion 90

Materials and Methods 91

Supplementary figures 97

References 102

Chapter 5: Concluding remarks 108

References 112

Table of Figures

Figure 1.1 Different pathways of APP processing by various secretase complexes 2

Figure 1.2 Immunostaining revealing Aβ plaque deposition 5

Figure 1.3 Immunostaining which identifies doubly phosphorylated tau (Ser202/Thr205) 6

Figure 1.4 Differentiation of a human-derived iPSC 10

Figure 2.1 Illustration of the variety of binding partners p53 45

Figure 2.2 Ac-KLVFFAE-NH_2 (E22) nucleation is impacted by pH. 48

Figure 2.3 pH influences E22 sheet orientation. 49

Figure 2.4 Different E22 congeners can adopt distinct sheet orientation 50

Figure 2.5 β-sheet configurations adopted by different truncated Aβ congeners produce distinct IR profiles 52

Figure 3.1 TEM micrographs of, A, Ac-KLVFFAE-NH2 and, B, Ac-KLVFFAV-NH2 peptides 56

Figure 3.2 Proposed model for two-step amyloid nucleation 59

Figure 3.3 Molecular structure of pep-RG or pep-KG 60

Figure 3.4 MD simulations of peptide/RNA interface 61

Figure 3.5 TEM micrographs of Ac-HLVIIAG-NH_2 assembly 64

Figure 3.6 Structural probing of Ac-HLVIIAG-NH_2 at early timepoints 65

Figure 4.1 Cross-β architecture allows for packing of other polymers in between the leaflets 75

Figure 4.2 Pep-KG assembly rate is accelerated when templated with dsDNA 78

Figure 4.3 Proposed energy diagram of distinct pathways that Pep-KG may undergo through context-dependent co-assemblies. 79

Figure 4.4 TMP and PolydA$_3$ nucleate Pep-KG assembly differently........................... 81

Chapter 1: Development of alternative, minimalistic model for Alzheimer's Disease

Original text: Li, N.[1], Gordon-Kim, C.[1], et al, Propagation of Alzheimer's Disease strains in human brain organoids. *In preparation*.

Alzheimer's Disease (AD) is the leading cause of all dementia cases. According to Alzheimer's Disease Society 2023 special report, approximately 11% of all Americans who are 65 years of age and older are affected by AD.[3] Given that this number is actively growing year over year, it is no surprise that the disease is increasingly becoming a public health issue. While the cause of the disease is not yet known, there have been certain gene mutations that are linked to an increased probability of developing the disease. These genes include *APP*, *PSEN1*, and *APOE*, which code for amyloid precursor protein (APP), presenilin-1, and apolipoprotein E, respectively.[5-12] Although the function of the membrane-bound protein APP is currently hotly debated, its direct interactions with various secretases, including γ-secretase, produces several peptide products. APP processing by α- and γ-secretases results in soluble, non-amyloidogenic peptides involved in cellular processes, while APP processing by β- and γ-secretases results in insoluble, amyloidogenic peptides, like amyloid beta 42 (Aβ42), that may be responsible for the hallmark proteinaceous plaques associated with Alzheimer's Disease, as illustrated in Figure 1.1.[12] As an aside, although not much is known about what regulatory function, if any, Aβ42 could possess, we do know that the peptide is prone to self-assembly to highly stable cross-β architecture. Cleavage by γ-secretase is catalyzed by its presenilin-1 subunit. Certain mutations on presenilin-1, which include Y115H, L435F, and C410Y, severely compromise γ-secretase activity and are linked to increased production of insoluble Aβ42 peptides which may be involved in plaque deposition.[2]

Amyloidogenic processing of APP has been the focus of the amyloid cascade hypothesis, which was the idea that clinical Alzheimer's Disease symptoms like mild cognitive impairments and dementia are preceded by Aβ-rich plaque formation. The manner in which these peptides are deposited is still unclear, and what roles these plaques play in the disease pathology is also highly contested, especially considering that anti-amyloid therapeutics that target amyloid plaques generally fail to recover or improve cognitive defects in AD patients.[14, 15] Furthermore, mammals other than humans seem

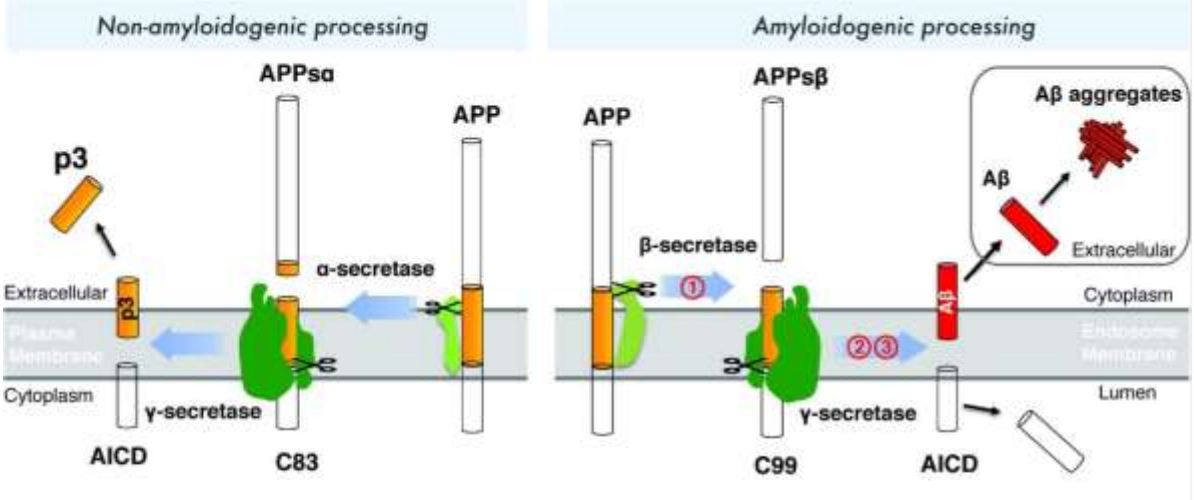

Figure 1.1 Different pathways of APP processing by various secretase complexes. Non-amyloidogenic APP processing by α- and γ-secretases results in soluble peptide products that may play a role in cellular regulation, while amyloidogenic APP processing by β- and γ-secretases results in insoluble peptide products that contribute to plaque deposition associated with Alzheimer's Disease. Modified from Zhao, J. et al.[12]

to be capable of withstanding high levels of Aβ-related plaques without succumbing to AD pathology, further loosening the strict connection between the peptide product and AD.

Recent literature suggests that the polymorphic *APOE* gene could be linked to higher probability of developing AD. *APOE* exists as 3 distinct polymorphs: *ε2, ε3*, and *ε4*, with *ε3* being the most widely distributed allele worldwide.[16] Individuals can carry 2 copies of *APOE*, and while approximately 15% of the population may carry 1 copy of *ε4*, only up to 3% carry 2 copies. Strikingly, the incidence of the seemingly rare homozygous *ε4* increases to over 40% in individuals with Alzheimer's Disease, suggesting a positive association between the *ε4* allele and the disease.[5-7, 17] Although direct interactions between apolipoprotein E and Aβ42 have not been observed, there have been studies that demonstrate co-localization of apolipoprotein E and pathological proteinaceous plaques, suggesting that the two biopolymers are within proximity in a disease-relevant context.[18, 19]

The many unknown variables and intricate dynamics amongst possible routes for pathological initiation make this disease particularly difficult to study. This thesis is an attempt to better understand the mechanistic details of Alzheimer's Disease initiation in a broader sense by developing an organoid model and in a stepwise fashion by generating minimalistic peptide models to uncover generalizable rules that dictate biopolymer interactions that result in paracrystalline assemblies that are not dissimilar from the disease-relevant plaques.

Chapter 1.1: Nucleation in the context of Alzheimer's Disease

AD progression is often discussed as a continuum, beginning with the preclinical stage, which is often accompanied by proteinaceous plaque and neurofibrillary tau tangle (NFT) accumulation.[20, 21] However, the buildup of these biomarkers is often observed after pathological changes in the brain structure, precisely within the locus coeruleus.[22, 23] The locus coeruleus (LC) is a small section of the brain, adjacent to the brain stem, and is a major contributor to the neurotransmitter norepinephrine; thus, LC is often thought to control not only mood and behavioral attributes but also overall neuroinflammatory pathways.[23, 24] There have now been many studies demonstrating that LC dysfunction, which includes overall LC shrinkage and significant reduction in norepinephrine production, precedes amyloid plaque deposition and tau tangles and even accelerates cognitive decline after amyloid plaque accumulation has been observed.[22-24]

Although many external factors could induce LC damage, significant tau tangle accumulation is consistently found in LC more so than any other parts of the brain, giving strong evidence that LC could be the nucleation site for pathological changes associated with AD.[25, 26] Tau, an intrinsically disordered protein whose function is to bind and organize microtubules, is a protein that experiences high levels of post-translational modifications, especially phosphorylation. These modifications affect tau's affinity to microtubules substantially. Excess phosphorylation around the protein's proline-rich region, known to bind actin, and the microtubule binding region reduces tau ability to bind microtubules – instead, this hyperphosphorylation scheme increases the protein's affinity to other tau proteins, potentially resulting in tau tangles.[25-28]

Much like amyloid plaque deposition, which accumulates extracellularly, the mostly intracellular tau tangle accumulation and its role in AD pathology is still often debated. However, the two biopolymers are still some of the most integral biomarkers that can be clinically tracked as they spread across the brain. It is still unknown how amyloid deposits and tau tangles could achieve such infectious cell-to-cell spreading.

Chapter 1.2: Challenges to modeling disease – finding an animal model

As previously mentioned, although accumulation of Aβ deposits often precedes AD pathology in humans, such accumulation has been observed in other mammals which do not exhibit cognitive impairments like their human counterparts. Ignoring other possible biopolymer interactions, such a discrepancy in disease phenotype across species could be credited to minute amino acid substitutions that destabilize cross-β formation in

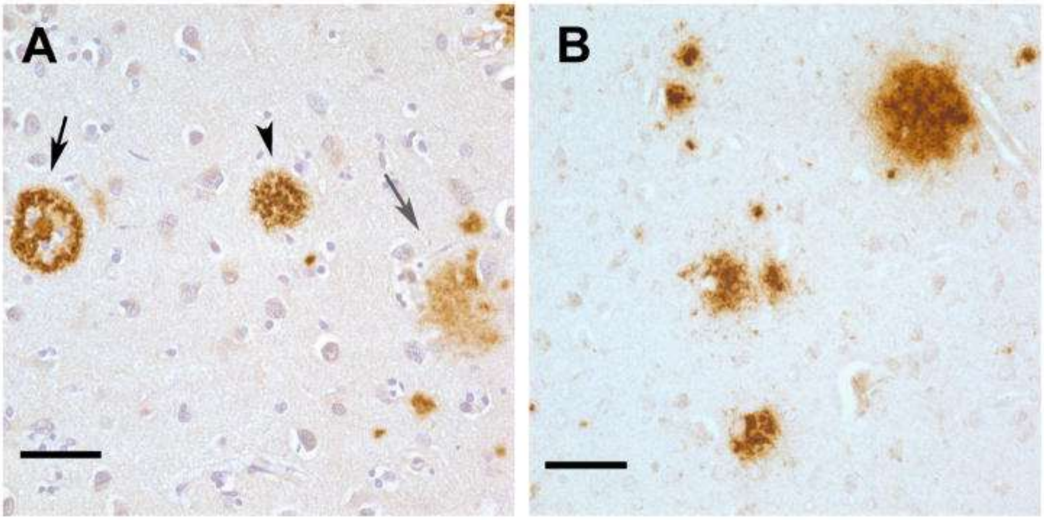

Figure 1.2 Immunostaining revealing Aβ plaque deposition in human AD patient (A) and in a 35 year old rhesus macaque (B), which shows plaque deposition at all stages, from diffuse aggregates (gray arrow in A), proto-aggregate (arrowhead in A), to dense aggregates (black arrow in A). Scale bar = 50 μm. Taken from Heuer, E., et al.[1, 2]

Aβ42.[10] For example, while the human Aβ42 sequence has high propensity for β-sheet, murine Aβ42 adopts a more helical structure instead. Human Aβ42 can self-associate due to the hydrophobic region Aβ42$_{16\text{-}23}$, which could template an extended, intramolecular cross-β structure along Aβ42$_{30\text{-}42}$ and Aβ42$_{1\text{-}7}$. However, because of mutations from polar, charged residue to nonpolar residues along the N-terminus, β-sheet formation in murine Aβ42 is destabilized.[10]

Such mutations, however, cannot explain nonhuman primates that do not ever develop dementia despite having large accumulations of Aβ plaques and 100% sequence homology in chimpanzees.[1, 29, 30] Immunostaining of human Aβ plaques and of a 35 year old rhesus macaque Aβ plaques reveal little difference in the proteinaceous deposition (Figure 1.2).[1] Similarly, immunostaining comparing intracellular tau tangles in the neurons of a human AD patient with their 41 year old chimpanzee counterpart also

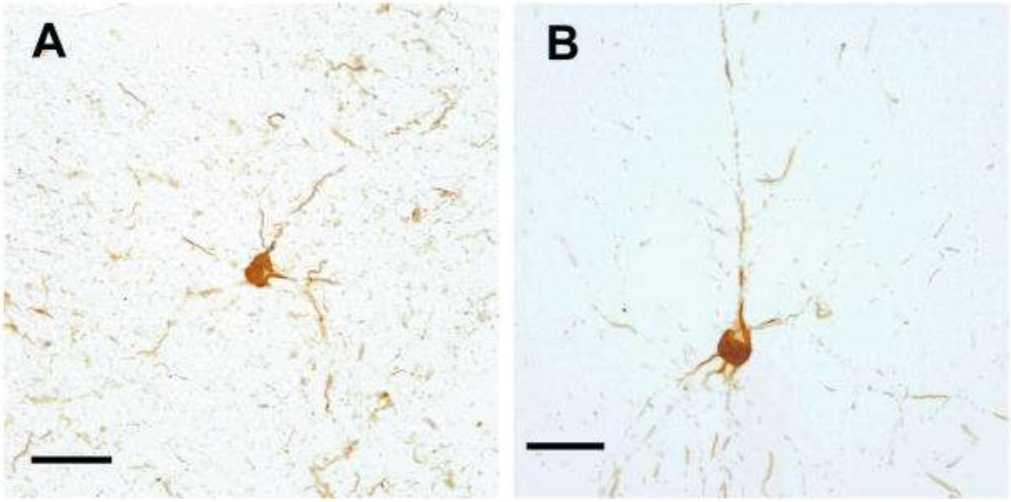

Figure 1.3 Immunostaining which identifies doubly phosphorylated tau (Ser202/Thr205) in human AD patient (A) and a 41 year old female chimpanzee (B) suggest identical generalized tau tangle accumulation in the two subjects. Scale bar = 50

show the same patterns of generalized hyperphosphorylated tau accumulation across the entire neuron (Figure 1.3).

Given that both human and nonhuman primates seem to share biomarker accumulation but diverge in the biomarker-associated cognitive impairments which are present in humans but absent in nonhuman primates, it is then not unreasonable to question whether there are other missing links that give rise to such neurodegeneration that only occur in humans. This divergence also brings into question whether nonhuman primates are a good model to study pathological development, aside from the high costs of maintaining such animals for long-term study. Thus, the search for a better model organism to study AD is a large motivation for the overall theme of this thesis and the main reason for exploring brain organoids as one such avenue.

Chapter 1.3: Understanding general rules that drive biopolymer interactions

Using brain organoids as a tool to shed light on AD pathology is important in understanding the disease overall. Further analyzing differentially expressed genes in disease-prone organoids relative to control organoids could certainly untangle what pathways may be directly affected throughout the pathological progression. Within these pathways, there exists a multitude of biopolymer interactions that need to be further elucidated- after all, these interactions are what gives rise insoluble, pathogenic plaques. Additional to developing a model for mapping out AD, developing a model to unravel the drivers for biopolymer interactions is also important, not only in a disease-relevant context, but also in a biomaterials perspective.

Generalized rules like the “sticker-spacer” model have been used to predict intrinsically disordered protein structures. The model characterizes charged and aromatic amino acids as “stickers” that drive cross-linking either through salt bridges, π-π, and cation-π complementarity, or charge-neutral and small amino acids as “spacers” which modulate space which the protein occupies, relative to the crosslinks.[31] However, rules that drive distinct biopolymer interactions, like protein-DNA interactions, have not yet been defined. Yet, such interactions are so commonplace in cellular processes like DNA replication and ribosome assembly. Here, minimalistic peptide and DNA models were used to study this phenomenon to seek out an overarching theme that may govern protein-DNA interactions.

Chapter 1.4: Modeling AD pathology using iPSC technology

iPSCs or induced pluripotent stem cells are an emerging biomolecular tool that involves the reverting of an already differentiated cell to its pluripotent state for the purpose of inducing differentiation to a different cell type.[32] In human-derived iPSCs (hiPSCs), somatic cells are collected in a non-invasive manner, typically through simple blood collection, where peripheral blood mononuclear cells are isolated to be reprogrammed for the induction of pluripotency. This induction process involves the use of a retrovirus to express genes which encode transcription factors, often dubbed as Yamanaka factors, involved in maintenance of embryonic stem cell phenotype. Upon retroviral gene integration to the host cell genome, the cells will express these transcription factors and become pluripotent as verified by expression of pluripotent cell markers like SOX2.[4, 32] Once pluripotency is achieved, the cells can now be introduced to transcription factors that will allow them to differentiate into progenitor cells for a cell type of interest. In this case, hiPSC differentiation into the forebrain can be induced by introducing the cell colonies to dorsomorphin.[4] Much like natural differentiated cells, iPSCs will also grow in a 3-dimensional space, as shown in Figure 1.4, which could more accurately reflect biological processes compared to other 2-dimensional cell culture studies.

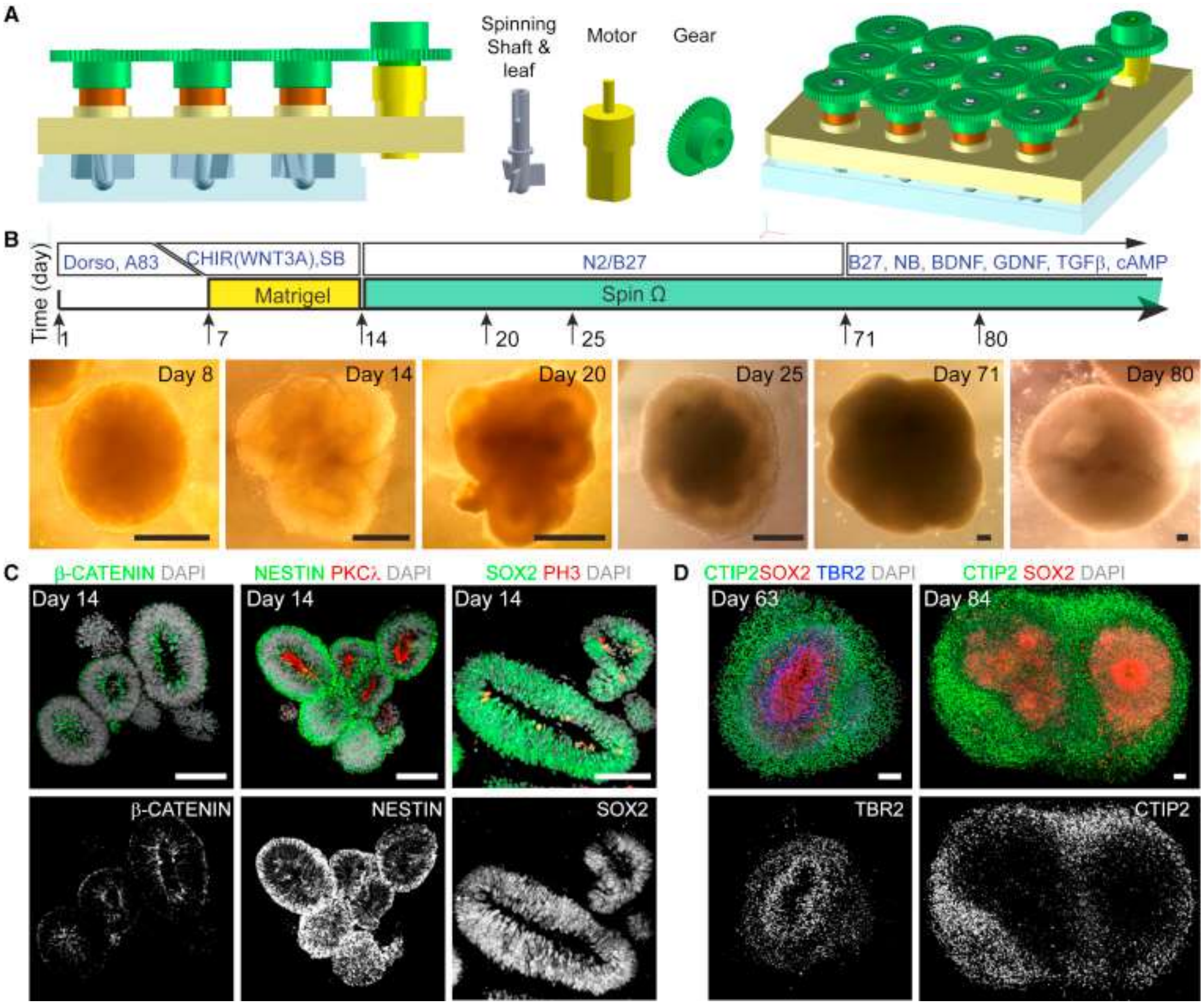

Figure 1.4 Differentiation of a human-derived iPSC. (A) Re-differentiated iPSCs are incubated in a perpetually tumbling environment in individual chambers of a bioreactor to maximize all cell exposure to oxygen and nutrients in the media, resulting in 3D organoids. (B) After iPSC pluripotency is achieved, a single colony is isolated and exposed to dorsomorphin for a week prior to passage to a Matrigel to allow for differentiation. Once iPSCs have shown signs of differentiation, the colony is treated with collagenase and passaged to fresh induction media and incubated in a bioreactor. (C) Fluorescence imaging of organoids show the distinct cortical layers into which successfully differentiated iPSCs can self-organize. Figure adapted from Qian, X., et al.[4]

Because organoids retain 100% of genetic information as the original donor cells, they could serve as a tool to model biomolecular interactions *ex vivo*, making them not only a promising technique for modeling disease initiation but also for personalized and regenerative medicine.[33] Here, brain organoids are used to test whether a cell-to-cell spread of AD pathology could be recapitulated *ex vivo*. If so, the isolation of such a propagating agent, or a propagon, from a diseased brain tissue could then be achieved.

Chapter 1.5: Cortical organoids could recapitulate AD-like phenomena

In collaboration with Alzheimer's Disease Research Center, four individuals were identified for the generation of 2 classes of organoids – familial AD (fAD) and healthy control (CTRL) organoids. Two individuals who do not exhibit dementia and possess wildtype *APP* and *PSEN1* genes served as donors for the control organoid development. Two individuals who have been diagnosed with dementia, one carries a V717I *APP* mutation and the other carries a Y115H *PSEN1* mutation, served as donors for fAD organoid development.[34-37] All four organoids were then incubated with propagons isolated from AD brain tissues as described below.

AD affected individuals carrying the *APOE* alleles ε3/ε4 were identified, and sections of their brain tissue were acquired for isolation of a potential propagon. These individuals were diagnosed with possible AD symptoms at different ages, and their pathological manifestations, as measured by the mini-mental state exam (MMSE), were also different. Samples were then categorized as either rapidly-progressing AD (rapid) or slowly-progressing AD (slow) based on the duration of AD diagnosis as well as the rate of cognitive decline year over year. The "rapid" samples were classified as those who died within 2 years of clinical AD diagnosis as well as MMSE score decline of greater than 5 points per year, while the "slow" samples consisted of those who died greater than 2 years after their AD diagnosis and MMSE score decline of fewer than 5 points per year.

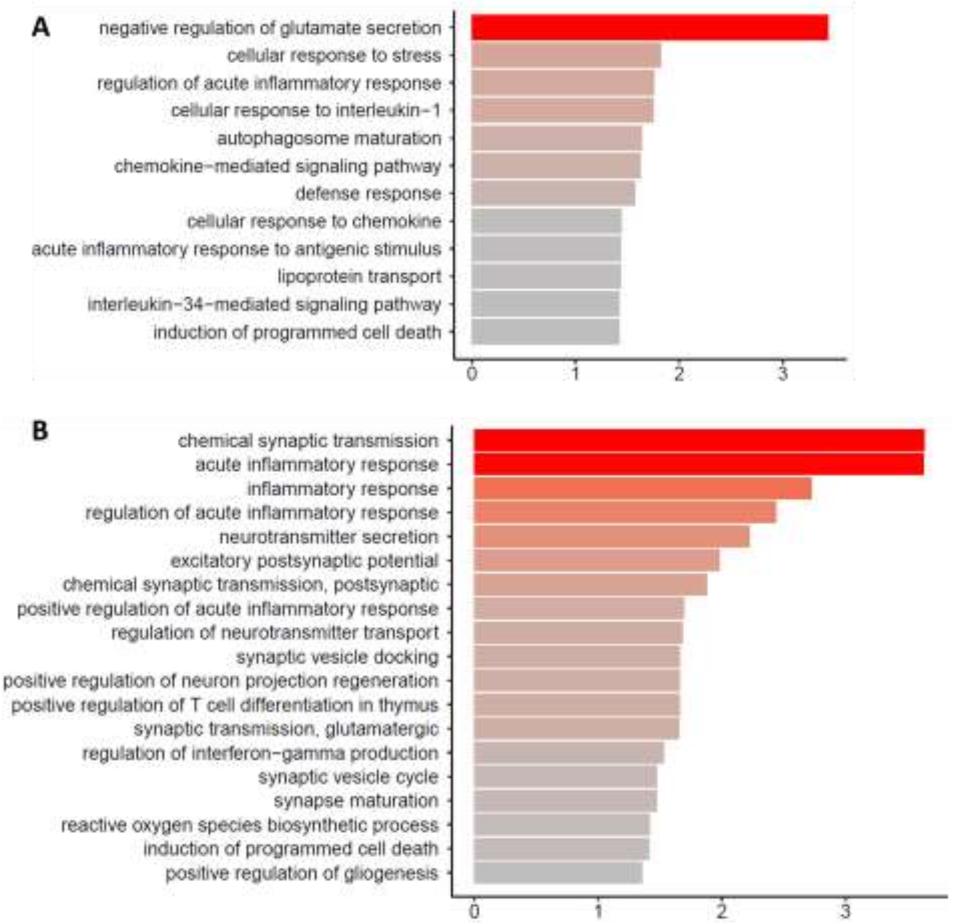

Figure 1.5 RNAseq analysis of differentially expressed genes in aggregate-treated healthy control organoids relative to untreated healthy control organoids. Organoids treated with both rapid AD nucleus (A) and slow AD nucleus (B) show increased upregulation of inflammatory response pathways.

Considering that possible pathogenic aggregates like amyloid plaques are especially insoluble and highly stabilized by their cross-β architecture, they should then be protease- and detergent-resistant. Techniques used to isolate high-titer prion extracts from brain tissue as established by Wenborn, A., et al were then used to isolate propagons from both AD and non-demented (ND) brain tissues, where the latter served as a healthy tissue control.[38-40]

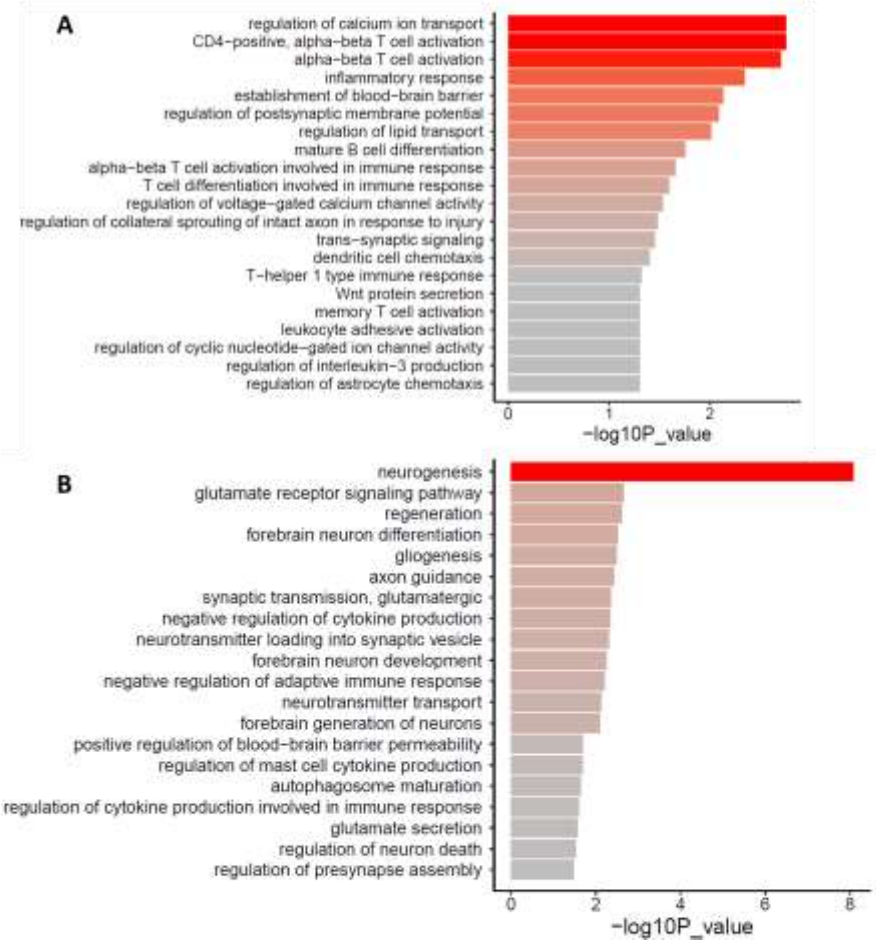

Figure 1.6 RNAseq analysis of differentially expressed genes in aggregate-treated fAD organoids. fAD organoids treated with rapid AD nucleus (A) and slow AD nucleus (B) show overall upregulated inflammatory response, but only fAD organoids treated with the slow AD nucleus exhibit intense activation of neurogenesis, which surpassed the organoid's inflammatory response.

Aggregate-treated organoids displayed distinct genotypic and phenotypic changes relative to untreated organoids. These genotypic changes, which are reflected in both fAD and control organoids, include overall upregulation of genes involved in inflammatory pathways in aggregate-treated organoids, as shown in Figures 1.5 and 1.6. One deviation in upregulation was observed in fAD organoids treated with the "rapid" tissue-derived aggregates, where not only is inflammatory response highly activated, but neurogenesis signaling is also significantly stimulated, as shown in Figure 1.6. Since AD is known as a neurodegenerative disorder, neurogenesis is typically not a phenomenon commonly associated with the disease. However, recent studies both *in vitro* and in transgenic

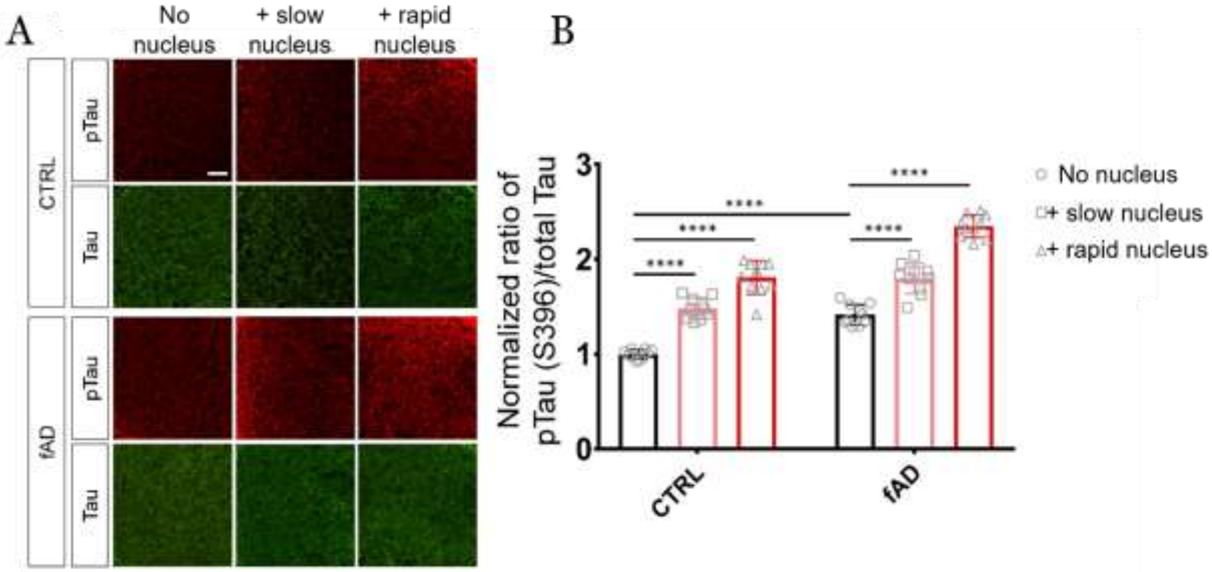

Figure 1.7 Differential pTau expression in nucleus-treated organoids. Immunostaining for pTau in organoids revealed distinct pTau expression profiles in aggregate-treated organoids relative to untreated organoids. (A) Fluorescence tagged anti-pTau (red) exhibited higher fluorescence intensity relative to anti-tau (green) in both healthy and fAD aggregate-treated organoids. Scale bar = 50 µm. (B) The ratio of pTau : tau fluorescence intensity was quantified to further disclose the discrepancy in global tau levels between healthy and fAD organoids when untreated (circle), treated with "slow" tissue-derived aggregates (square), and treated with "rapid" tissue-derived aggregates (triangle).

mouse models, have observed increased levels of neurogenesis, with some suggesting that this stimulation is directly linked to the presence of oligomeric Aβ42.[41, 42]

Given the exciting initial RNAseq data which seem to broadly recapitulate some AD-associated genotypic changes, further analyses of the organoids were then done to look for other AD-like phenomena. Immunostaining of all organoid samples with hyperphosphorylated tau (anti-pTau S396) antibodies revealed distinct pTau profiles when organoids are treated with brain-derived aggregates. Compared to untreated organoids, all aggregate-treated organoids, both healthy and fAD types, exhibited drastically higher levels of pTau relative to tau across the board, as shown in Figure 1.7. Interestingly, this difference in expression is even more significant in both healthy and fAD organoids treated with rapid AD nucleus. This finding is in agreement with current literature which suggests that excessive tau phosphorylation, which results in neurofibrillary tangles, coincides with AD symptoms.

Chapter 1.6: Characterization of tissue-derived aggregates

The AD-like changes induced in the organoids studies by the AD brain tissue-derived aggregates have so far faithfully reflected the literature consensus that describes the neuroinflammation and paracrystalline accumulations in initial AD manifestation.[23, 24, 26] The *ex vivo* studies even recapitulated the same, distinct pathological pTau expression that is commonly associated in AD brains, raising the question of whether this accumulation is due to interactions that could be intrinsic to tau and the tissue-derived aggregates. To test this, further characterization of tissue-derived aggregates was done to probe any possible interactions with other known AD biomarkers such as Aβ42. As Aβ42 accumulation as plaques is found in all instances of AD patients and that the tissue-derived aggregates were found to initiate AD-like symptoms in the organoid experiments, identifying possible cross-talk between the two species is an immediate first question. To test this, both AD and ND brain tissue-derived aggregates were treated with synthetic Aβ42 peptides and incubated at 37°C. After one month, the assemblies were viewed via electron microscopy and can be found in Figure 1.8.

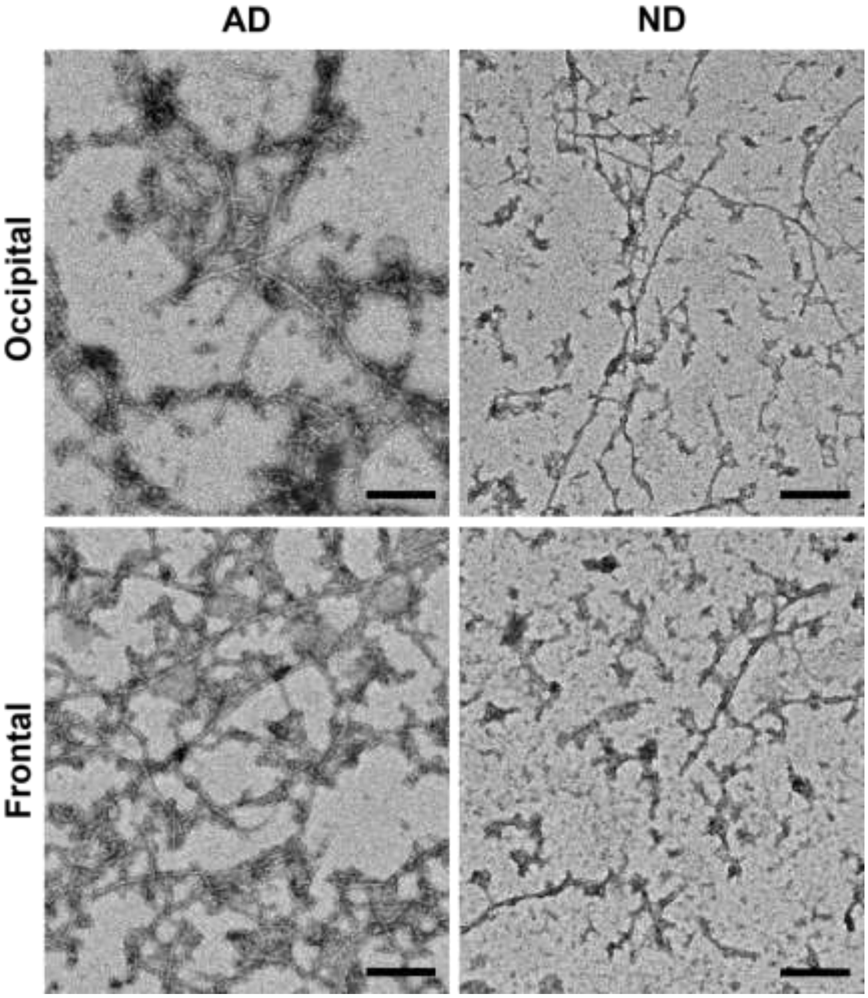

Figure 1.8 Electron micrographs of tissue-derived aggregates treated with synthetic Aβ42. Both frontal and occipital brain sections of AD individuals are shown against their ND counterparts as labeled. Scale bar = 200 nm.

Unsurprisingly, microscopy grids occupied by Aβ42-treated AD tissue-derived samples were more densely populated with higher order fibril assemblies compared to the Aβ42-treated ND samples. While Aβ42 on its own is known to self-assemble into fibrils identical to those found in Figure 5, the difference in fibril populations between the AD and ND samples suggests that Aβ42 may be accelerating the formation of highly ordered structures which could be disease relevant.

Chapter 1.9: Probing possible Aβ/tau interactions *in vitro*

Individually characterizing each biomarker interaction, tau and Aβ42, with tissue-derived aggregates has helped clarify possible routes of pathological initiation. However, little is known about the cell-to-cell spread of these paracrystalline assemblies. One interesting observation about these assemblies is that although they localize in distinct spaces, with Aβ42 being concentrated extracellularly and tau intracellularly, their pathogenic accumulation is often simultaneous. Could this concurrent accumulation result in cross-species interactions? To test this, full length Aβ42 was assembled at 37°C to achieve homogeneous fibrillar morphology, as shown in Figure 6, and was then allowed to interact with PHF6 peptides. PHF6 is a hexapeptide, VQIVYK, within the third sub-domain of the tau 4 repeating domains and is relevant because it is the site for microtubule binding in full-length tau.[26-28, 43] Additionally, this sequence also serves as a β-sheet forming motif that facilitates intramolecular association with another β-sheet forming motif, PHF6* or VQIINK, in the second sub-domain within the repeating domains. Tau and its isoforms often differ in the number of repeating sub-domains, with the second sub-domain often excluded.[43-46] For this reason, the following experiments will exclusively look at PHF6 interactions.

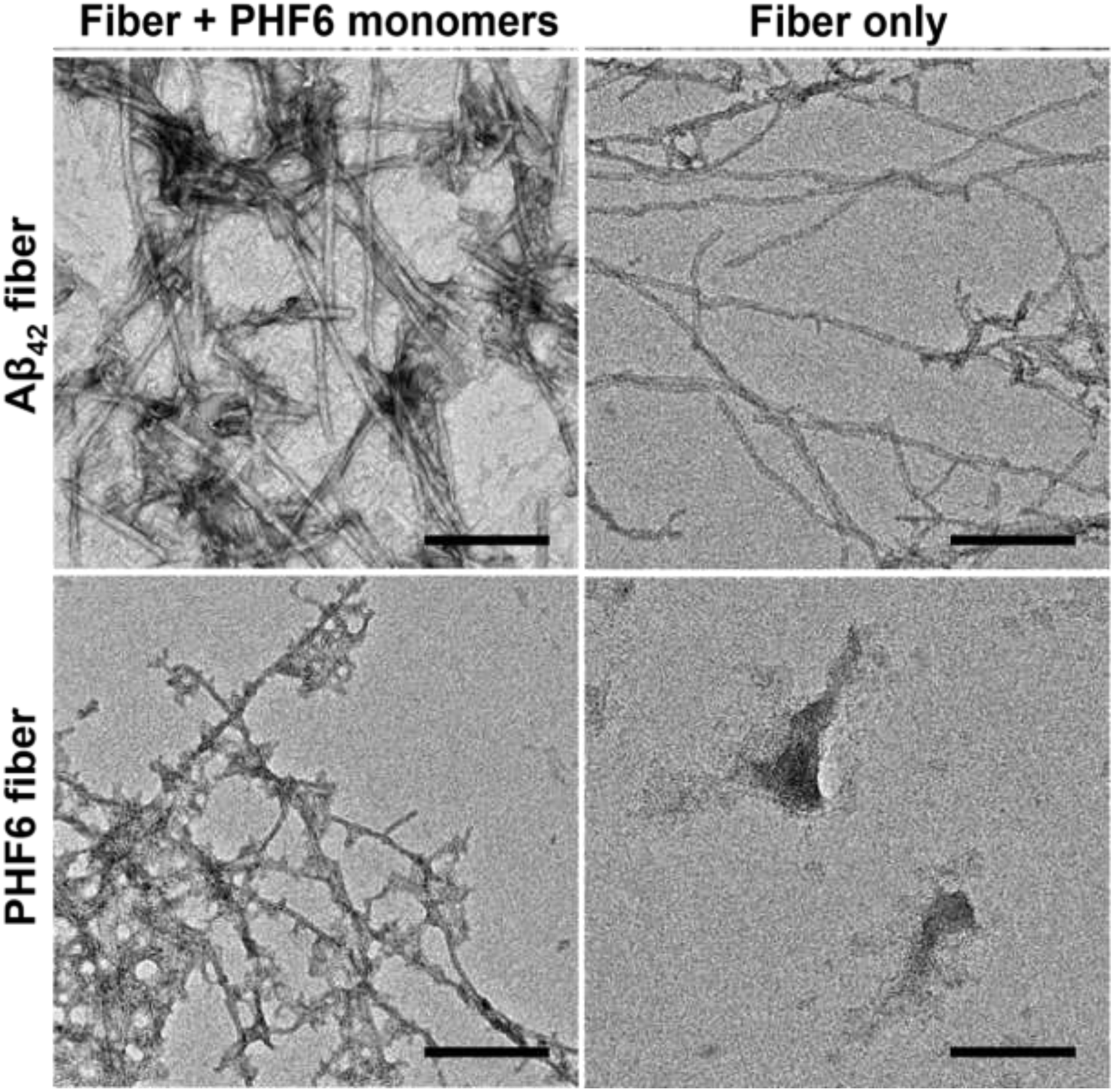

Figure 1.9 Electron micrographs of Aβ42-seeded and unseeded PHF6 assemblies. Scale bar = 200 nm.

Fresh PHF6 monomers were then added to a pre-sonicated 1% solution of mature Aβ42 and allowed to assemble for 1 month, and this cross-seeded sample was compared against an unseeded PHF6 sample that was assembled at the same time. Electron micrographs in Figure 1.9 indicate that the Aβ42-seeded PHF6 sample had higher fibrillar population relative to the unseeded sample. Like the previous cross-seeding experiment with tissue-derived aggregates, this finding also suggests that Aβ42 accelerates paracrystalline assemblies in PHF6 which exhibits lower propensity for self-assembly.

With the noticeable difference in overall paracrystalline ordering in the PHF6 and Aβ42 seeds, with mature PHF6 showing low level of order as marked by the nondescript aggregates, we then questioned whether the amplification of fresh PHF6 fibrillization is sensitive to the initial ordering of the nucleus. Thus, further experiments were done by seeding fresh PHF6 with a 1% solution of mature Aβ42 or PHF6 (1% Aβ42 fibers + PHF6 or 1% PHF6 fibers + PHF6, respectively) and by seeding fresh PHF6 with a 1% solution of freshly prepared Aβ42 or PHF6 (1% Aβ42 seeds + PHF6 or 1% PHF6 seeds + PHF6, respectively). The growth of PHF6 assemblies was monitored via thioflavin T (ThT) fluorescence assays. ThT is a small molecule that fluoresces upon intercalation between β-sheet interfaces within a cross-β structure; thus, ThT fluorescence intensity is directly correlated to the presence of highly stabilized β-sheets. Tracking of ThT fluorescence intensity over time in Figure 1.10 corroborates the earlier finding that, overall, Aβ42 amplifies PHF6 assembly compared to PHF6-seeded PHF6 assembly. A closer inspection reveals that fresh PHF6 growth seeded by the two distinct Aβ42 nuclei diverges early on, with the mature Aβ42-seeded sample lagging behind fresh Aβ42-seeded sample. This suggests that PHF6 assembly is indeed sensitive to the initial nucleus ordering to achieve paracrystalline structures. Overall, these findings support the hypothesis that Aβ42 and tau could have mutualistic, disease-relevant interactions while also corroborating evidence that suggest these aggregates may be complementary with Aβ42.

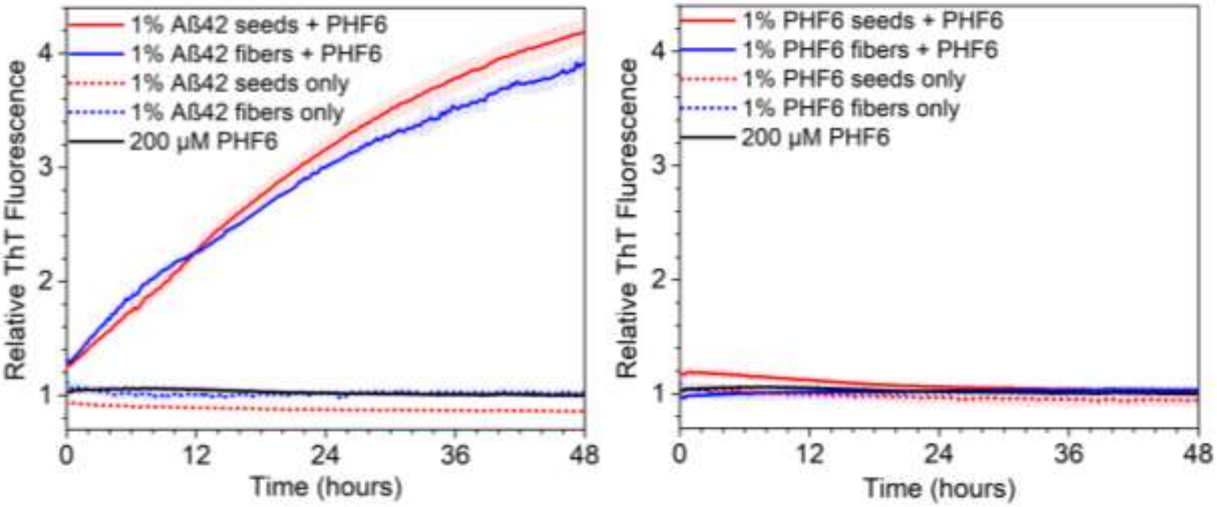

Figure 1.10 Kinetics analysis by thioflavin T of cross-seeded PHF6 assemblies. The left panel shows thioflavin T fluorescence intensities in differently seeded PHF6 assemblies by Aβ42. The right panel shows thioflavin T fluorescence intensities in differently seeded PHF6 assemblies by PHF6.

Decades of experimental studies have shown that both biopolymers tend to form β-sheets.[10, 25, 27, 45-50] In Aβ42, this propensity is owed to its hydrophobic domain along its 16th and 22nd residues KLVFFAE (Aβ$42_{16\text{-}22}$ or E22), and in tau it is owed to 2 motifs: VQIINK (PHF6*) and VQIVYK (PHF6). Could a shared β-sheet motif, then, be enough to facilitate polypeptide interactions between the two species? Cross-seeding of PHF6 with full-length Aβ42 did not reveal whether their interactions were due to β-sheet complementarity, so to probe motif-specific interactions, PHF6 was assembled with congeners, or variants, of the minimal Aβ42 model E22. As β-sheets could exist in either parallel or antiparallel fashion, could PHF6 assembly be sensitive to β-sheet configuration exhibited by the seed? Studies which involve single residue substitutions on E22 that give rise to E22Q (KLVFFAQ) and E22L (KLVFFAL) have shown that these peptide congeners adopt parallel and antiparallel β-sheet configurations, respectively.[51-53] These two peptides were then used as a basis set for establishing any selection rules with respect to PHF6 assembly.

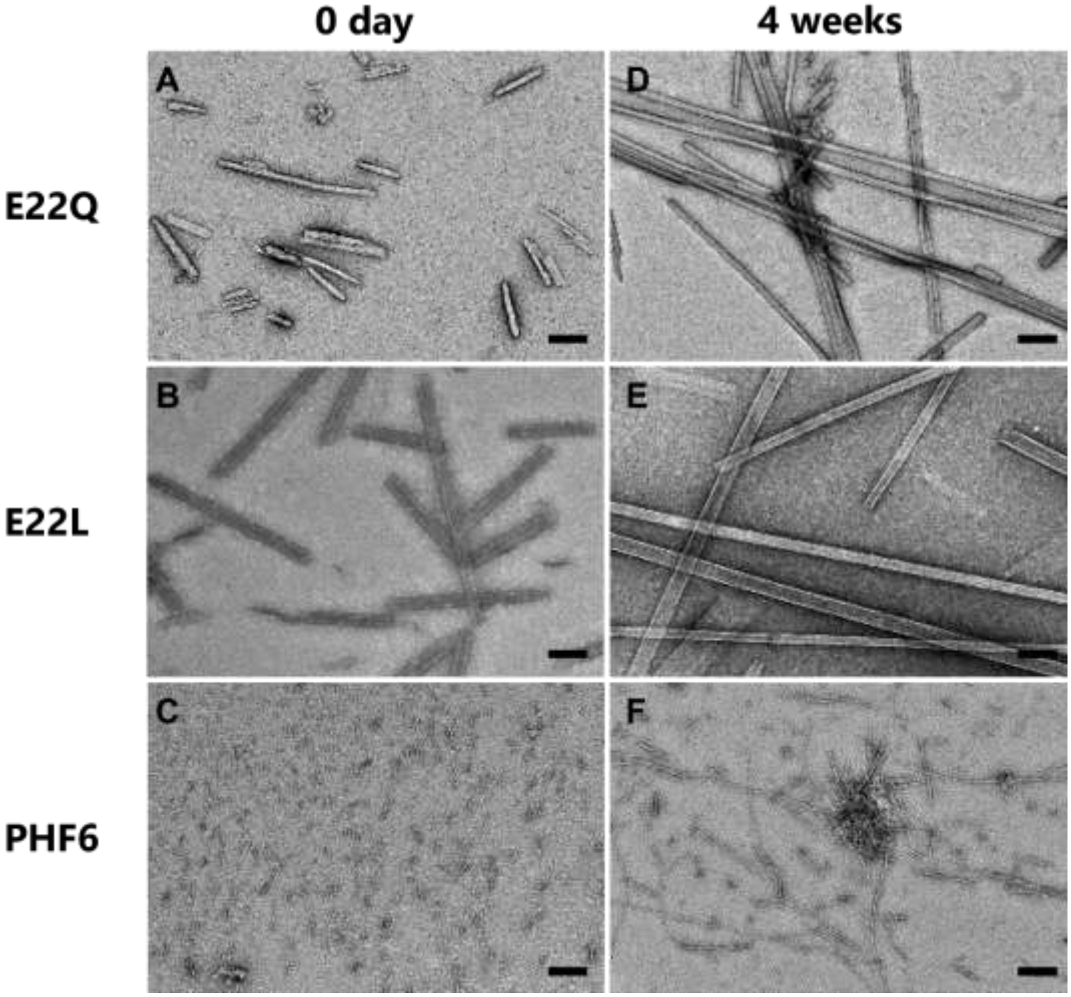

Figure 1.11 Electron micrographs reveal the distinct morphologies of E22 congener seeds. E22Q (A, D) and E22L (B, E) quickly assembled into fibrils and nanotubes, respectively, within 24 hours of peptide dissolution, while PHF6 (C, F) took considerably longer to mature into the long fibril morphology exhibited at maturity. Scale bar = 200 nm.

E22Q, E22L, and PHF6 seeds were assembled to maturation. Since PHF6 assembles slowly, all peptide samples were incubated for 1 month prior to

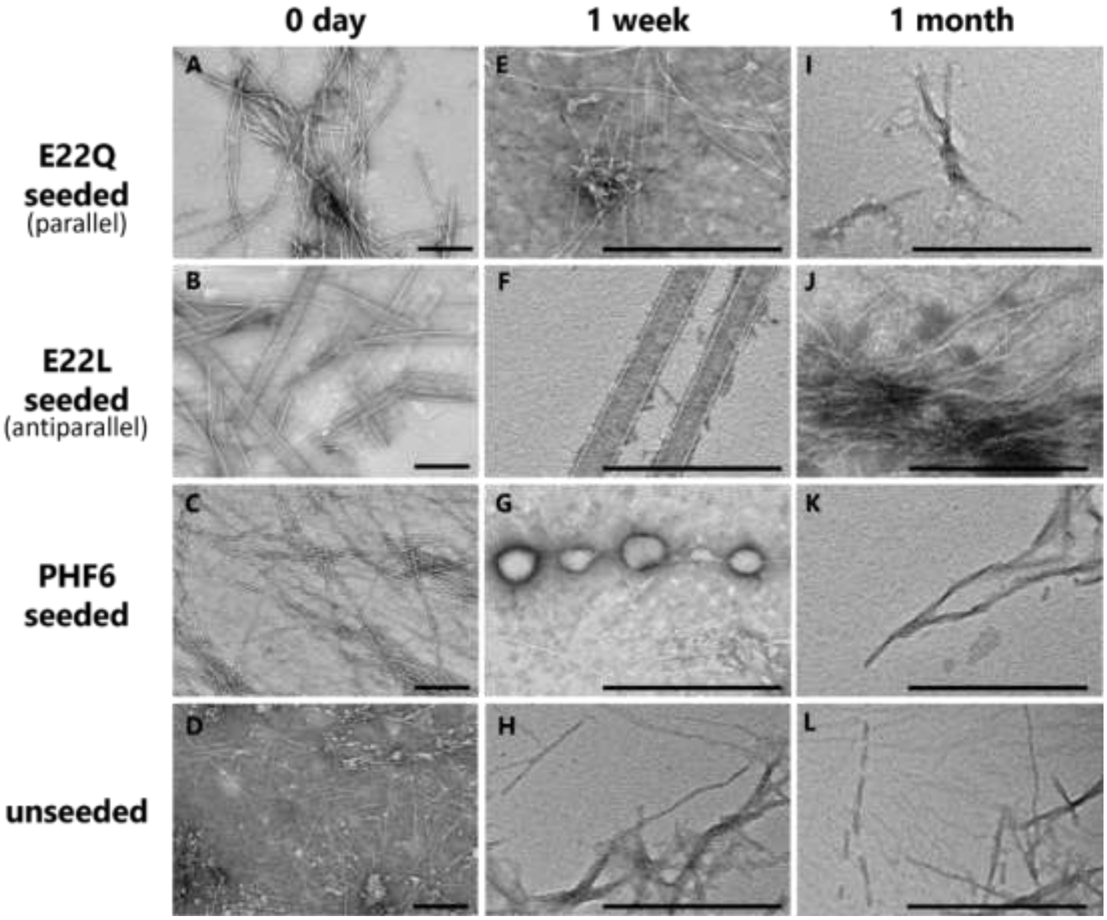

Figure 1.12 Electron micrographs of both seeded and unseeded PHF6 assemblies. E22Q-seeded PHF6 assemblies (A, E) were densely populated with fibrils but were sparse at 1 month (I). E22L-seeded PHF6 assemblies (B, F) retained the seed nanotube morphology up to 1 week but then transformed into fibril morphology at 1 month (J). PHF6-seeded PHF6 assemblies (C) retained the seed fibril morphology, but large particles were found at 1 week (G), and only fibrils were observed at 1 month (K). Unseeded PHF6 assemblies (D) showed highly heterogeneous assemblies of fibrils and less ordered aggregates but exhibited homogeneous fibril morphology after 1 week (H, L). Scale bars = 200 nm

seed generation. E22Q and PHF6 were both found to assemble into fibrils, while E22L formed bilayer nanotubes (Figure 1.11), which agree with literature data.[51-53] Fresh PHF6 peptides were then added to each seed solution at a PHF6 : seed ratio of 4 : 1, where the seed concentration was set to 0.25 mM – well below the generalized 0.5 mM critical aggregating concentration for E22 and its congeners to discourage exclusive seed proliferation and encourage PHF6-seed mutualistic interactions. The cross-seeded samples were allowed to mature for 1 month, and their morphologies were characterized via electron microscopy as shown in Figure 1.12. Within 24 hours, all cross-seeded PHF6 assemblies (Figures 1.12 A, B, and C) were found to still exhibit the same morphology as their seeds – fibrils for both E22Q- and PHF6-seeded samples and nanotubes for E22L-seeded samples. However, at 1 week, both E22Q- and PHF6-seeded samples showed morphological discrepancies (Figures 1.12 E and G). Grids with the former sample displayed noisy, or less clear, backgrounds that were due to small, disordered aggregates, while the latter displayed large particle formation along co-existing fibrils. However, E22L-seeded samples (Figure 1.12 F) still showed the seed nanotube morphology. At 1 month, all cross-seeded samples showed fibril morphologies (Figures 1.12 I, J, and K). In particular, E22L-seeded PHF6 assembly (Figure 1.12 J) showed significantly more fibrils than other seeded samples, suggesting that the antiparallel E22L seeds were complementary to PHF6 assembly. These micrographs suggest that not only are shared β-sheet motif enough to template PHF6 assembly, but that the overall assembly pathway is also sensitive to the β-sheet ordering within the seed.

Chapter 1.10: Identification of possible apolipoprotein complexes in brain aggregates

The above findings suggest that Aβ42 could amplify highly ordered fibril morphology in tissue-derived aggregates. However, there were also other ordered structures that survived harsh treatments to which the tissues were subjected. The extraction protocol, initially designed to extract high-titer prions, involved the use of a metal chelator, nucleases, proteases, and a non-denaturing detergent. So, any surviving ordered structures are certainly an interesting object to study. Raw tissue-derived

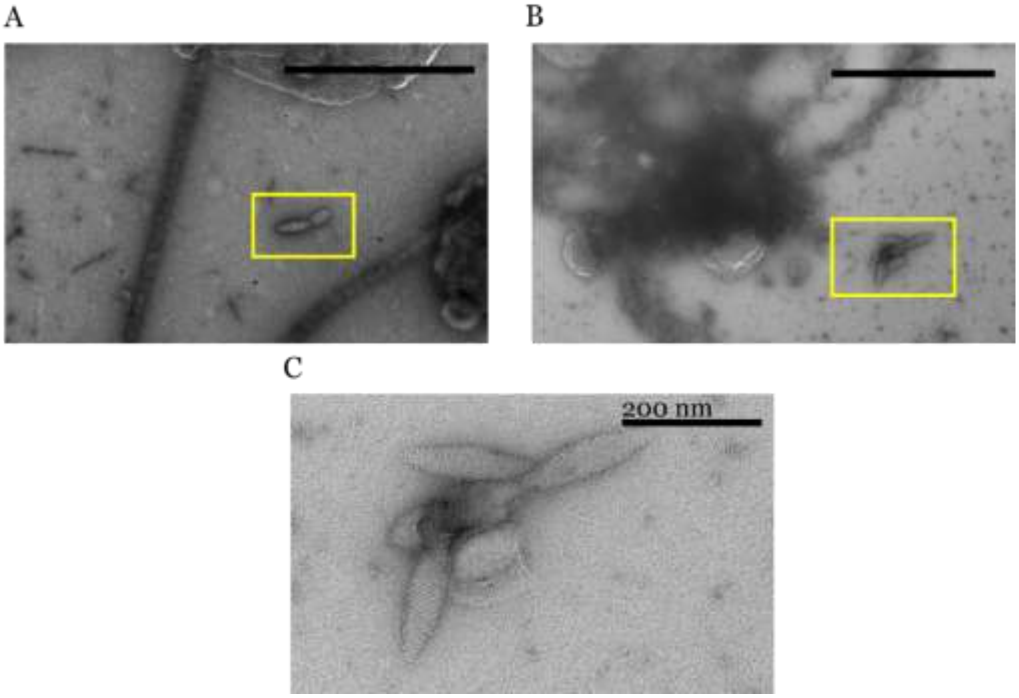

Figure 1.13 Highly laminated structures observed in untreated AD brain tissue samples. Collagen (A), short fibrils, and possibly apolipoprotein E complex (yellow boxes in A and B) were observed in all samples. (C) A zoomed-in view of the possible apolipoprotein E complex. Scale bar = 1 µm unless otherwise noted.

aggregates were imaged immediately after the last pelleting step as described in the methods section below. These samples showed very little traces of fibrils and a multitude of structures with varying degrees of lamination (Figure 1.13). Some of these laminated structures were collagen, as they showed alternating dark and light bands; however, there were shorter, pointed oblong-shaped or football-like, morphologies that were also highly laminated but do not match the same striation patterns as collagen as noted by yellow outlines in Figure 1.13.

An extensive literature search revealed an exciting potential candidate for what these football shapes could be. Apolipoprotein E (ApoE), a protein often found complexed with lipids and is involved in lipid transport, has previously been linked to AD pathology. ApoE, upon interaction with lipids, forms vesicles, where phospholipid heads are solvent exposed at the membrane, where ApoE is embedded all throughout.[5-8, 16-19, 54] Coincidentally, studies in 2011 and 2013, which sought to optimize isolation conditions specifically for ApoE complexes not only found the same highly laminated oblong-shaped structures (Figure 12), the method also used the same salt, sodium phosphotungstic acid (NaPTA), that was used for the purpose of pelleting proteinaceous aggregates from brain tissues as described in this dissertation.[13, 55] These studies suggest that, while ApoE complexes exist as vesicles *in vivo*, interaction with large salts like NaPTA allowed for charge passivation of the largely positively charged ApoE complex surface, where the positive charges are attributed to protonated amines at the phospholipid heads. This charge passivation not only directly results in the joining of adjacent vesicles but also in the flattening of the vesicle surface to maximize charge complementarity, a phenomenon known as the rouleau artifact, as illustrated in Figure 1.14 F.[55] While direct interactions of ApoE and AD-associated proteins have not yet been characterized *in vivo*, there have been studies that suggest that ApoE and a 40-residue Aβ species could have direct interactions via salt bridges.[54] The presence of these laminated football morphologies could serve as one of the earliest preliminary evidence for a real involvement of ApoE from AD brains.

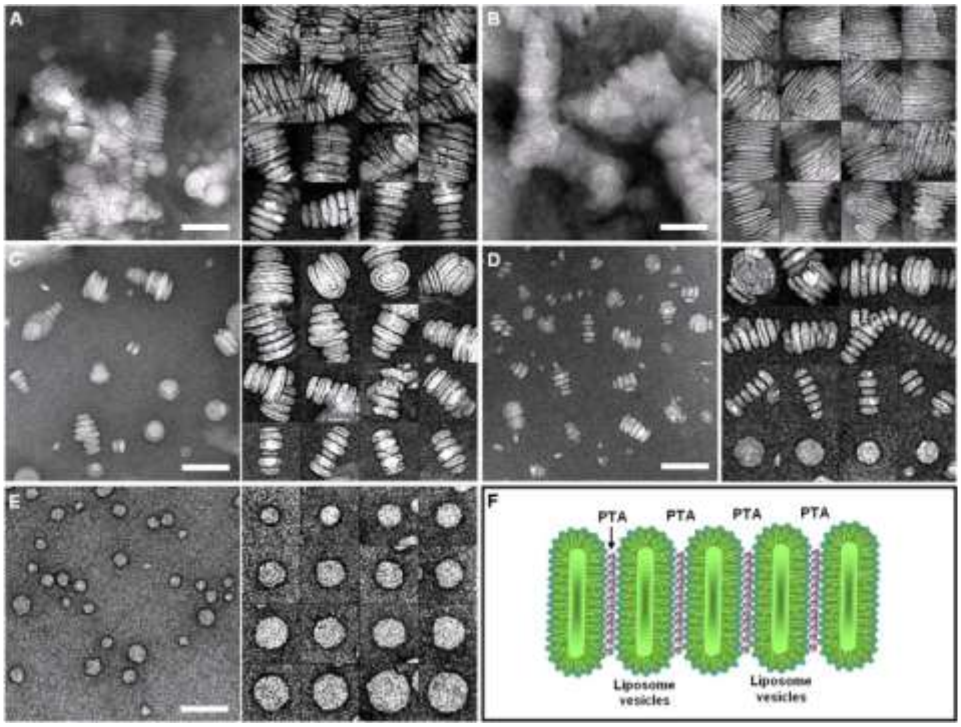

Figure 1.14 Effect of NaPTA addition to ApoE complexes. (A) Rouleau artifact in ApoE complexes was first discovered with conventional negative staining of ApoE using 2% NaPTA solution. (B) Higher NaPTA concentrations lead to higher degree of lamination and flattening of ApoE complex, while (C) lower NaPTA concentrations lead to the opposite effect. (D) Substituting NaPTA with uranyl formate, leaves the ApoE complex shape as more rounded and less laminated than NaPTA-stained samples. (F) Illustration of charge passivation along the surface of ApoE (green) by phosphotungstate ions (purple). Scale bar = 100 nm. Adapted from Zhang, L., et al.[13]

Conclusion

The challenges posed by AD make it difficult to understand the disease at its earliest timepoints. Given that the most similar animals, nonhuman primates, could exhibit biomarkers most associated with the disease but not display cognitive dysfunction, such animal models, so far, have not yet been able to fully recapitulate AD-like symptoms as they present in humans. Above all, the high cost and duration of time in maintaining and observing primate models over the course of their lives make for a nearly impossible case of gathering enough data points to generate any conclusive results. To bypass these issues, the development of brain organoids, generated from real AD patients, were used in an attempt to recapitulate AD-like phenomena. These phenomena, which were successfully reproduced by the organoids, included overall upregulation of inflammatory response and highly expressed phosphorylated tau, a post-translationally modified tau often linked to neurofibrillary tangles.

Moreover, another AD biomarker, Aβ42, was shown to amplify highly ordered paracrystalline assemblies when incubated with protease- and detergent-resistant species isolated from AD brain tissues. These studies also explored the possible entanglement of the two biomarkers by cross-seeding Aβ42 and the tau fragment PHF6. Considering that both Aβ42 and PHF6 share the same propensity for β-sheet formation, it was then shown that this shared motif alone is enough to amplify PHF6 assembly, which otherwise is slower to assemble into fibril morphology. Furthermore, not only is β-sheet complementarity enough to nucleate such a morphology, PHF6 assembly pathway is sensitive to the orientation of β-sheets that exist in the seeds, preferring the antiparallel configuration.

Finally, the raw isolates from AD brain tissues were directly imaged with electron microscopy to reveal a variety of structures of varying order. Among the structures that survived protease, nuclease, and non-denaturing detergent treatment were short fibrils, collagen, and highly laminated, football-like morphologies. A comparison of these footballs was made to several studies that sought to better isolate apolipoprotein E complexes in their native structures. These studies and the isolation of these footballs both use sodium phosphotungstic acid, or NaPTA, which was found to effectively passivate the surfaces of apolipoprotein E vesicles, which were mostly populated by protonated phospholipid heads. Together, these observations seem to not only shed light on biomarker interactions but also reveal a real link between apolipoprotein E and AD brains – a connection that had been mainly studied *ex vivo*.

Materials and Methods

Methods with underlined texts were performed by Noel Li and me in the Lynn group. Methods indicated otherwise were performed by members of the Wen group.

Peptide synthesis and purification

Aβ_{42} peptide was synthesized on a CEM Liberty automated microwave peptide synthesizer. Fmoc-Val-PAL-PEG-PS resin (0.19 mmol/g, Applied Biosystems). Fmoc-Ala-PAL-PEG-PS resin or Fmoc-Ala-TentaGel R PHB resin were used. Resins were swollen in 50% DMF/ 50% DCM for at least 15 min before the first deprotection reaction. Deprotections were performed with 20% v/v piperidine) in DMF at 75°C for 3 min, and couplings were performed with 1 M HOBt in DMF and 0.5 M N, N′-Diisopropylcarbodiimide (DIC, Aapptec, Louisville, KY) in DMF at 75°C for 5.5 min.

However, histidine was double-coupled at 50°C for 8 min and arginine was double-coupled at 75°C for 10 min.

For PHF6, E22Q and E22L, Fmoc-rink amide MBHA resin (Anaspec, Fremont, CA) was used. Deprotections were performed in 20% v/v piperidine, and activations were done with N,N′-diisopropyl carbodiimide (DIC; CAS# 693-13-6 AAPPTEC) as the activator, Oxyma Pure (CAS# 3849-21-6 CEM) as the activator base. N-termini were acetylated by the addition of 20% v/v acetic anhydride in DMF.

The resins were then filtered, washed with dichloromethane (DCM) and dried overnight in a desiccator. Peptide cleavage was performed using 10 mL of TFA/thioanisole/1,2-ethanedithiol/anisole (90:5:3:2% v/v/v/v) at room temperature for 3 hours. Then the mixture was filtered drop-wise into cold (-20°C) diethyl ether, and the precipitated peptide was collected by centrifugation at 4,000 rpm, 4°C for 10 min. The pellet was washed three times with cold diethyl ether by resuspension and centrifugation, and then dried in a desiccator overnight.

The crude peptide was then dissolved in a minimal amount of 15% MeCN + 0.1% trifluoroacetic acid and purified by RP-HPLC using a semipreparative C18 column (Waters Corp., Milford, MA) with a 1%/min acetonitrile-water + 0.1% formic acid gradient. Due to polymorphism, Aβ42 often elutes at distinct times, so all fractions were collected for MALDI-MS analysis with α-cyano-4-hydroxycinnamic acid (Sigma-Aldrich) as the matrix. Fractions containing peptides were pooled and acetonitrile was removed by rotary evaporation. The peptides were then lyophilized to dryness.

Quantification of peptide content in Aβ42

Since the lyophilized peptides contain residual salts and water of hydration, the peptide content of each Aβ_{42} batch was determined by dissolving a small amount of peptide in water (~0.2 mg in 1 ml) and measuring the concentrations of serially diluted peptides with the BCA (bicinchoninic acid) assay (Thermo Fisher Scientific). By correcting for the peptide content each time, the lyophilized powders were weighed out, batch-to-batch variations in concentrations were minimized.

Disaggregation of purified peptides before assembly or seeding

A$\beta_{16\text{-}22}$ E22Q, A$\beta_{16\text{-}22}$ E22L and PHF6 peptides were dissolved in 1,1,1,3,3,3-hexafluoro-2-propanol (HFIP) in glass vials to 0.5 mg/ml, then bath-sonicated for 30 min before the solvent was evaporated under a stream of N_2 to form a thin film. Peptides were reconstituted either by adding 20% MeCN/80% water + 0.1% TFA or 50 mM Tris-HCl (pH 7.4) to the vials, and then bath-sonicated until the films were dissolved.

Aβ_{42} was treated with NH_4OH according to Ryan et. al.[56] Briefly, the Aβ peptide was dissolved to 0.5 mg/ml in 10% w/v NH_4OH for 10 min on the bench before a 5-min bath-sonication. The solution was then divided into 1 ml aliquots in low-retention microfuge tubes, flash-frozen in liquid N_2, and lyophilized. The lyophilized peptide was dissolved in 1 mM NaOH (pH ~ 10.8, 90% of the volume to make a 100 µM or 20 µM solution) until the solution was visibly clear of white powder. 10X sodium phosphate buffer with 0.2% NaN_3, pH 7.1 (the remaining 10% volume) was then added, bringing the final concentration to 20 µM Aβ_{42} in 10 mM sodium phosphate with 0.02% NaN_3 at pH 7.4. Finally, large aggregates were removed by filtration through a pre-rinsed, 0.22 µm filter before the sample was ready for use.

Cross-seeding of A$\beta_{16\text{-}22}$ E22Q and E22L with PHF6 monomers

Parent assemblies were prepared by incubating the monomers at a 0.5 mM peptide concentration in 20% MeCN + 0.1% TFA at room temperature for at least one month, at which time the presence of fibers or nanotubes as confirmed by TEM. Seeds were generated from the parent assemblies by probe-sonication for 30 sec (30% amplitude, Cole-Parmer CPX 750), before a four-fold volume of HFIP-treated PHF6 monomers at 0.5 mM in 20% MeCN + 0.1% TFA was added. The cross-seeded PHF6 assemblies were then incubated at room temperature for one month.

Transmission electron microscopy

Peptide solutions were deposited on TEM grids (200 mesh formvar/carbon-coated copper grids, Electron Microscopy Sciences) and incubated for 1.5 - 2 min on the grids. The excess solution was then wicked away with filter paper before the grid was stained with 2% w/v uranyl acetate in water for 1.5 min. Grids were imaged with a Hitachi HT7700 transmission electron microscope with a tungsten filament at an accelerating voltage of 80 kV, and the pixel input ranges of the image files were adjusted in GIMP 2 (GNU Image Manipulation Program) for clarity.

Brain extract amyloid enrichment

Autopsy-derived, fresh-frozen samples of frontal (F) and occipital (O) neocortex from AD and non-demented healthy control (ND) patients were acquired from the Emory Alzheimer's Disease Research Center. AD patients carry 2 copies of *APOE* ε3, and ND patients carry 2 copies of *APOE* ε4. This study was conducted under the auspices of the Emory ADRC and was approved by the Emory Institutional Review Board. Informed consent for tissue donation was obtained from the subjects or their family members.

We used a modified enrichment protocol, originally developed by Wenborn et.al.[38] for isolating prion strains from mice, to generate high-titre extracts of protease- and detergent-resistant proteinaceous seeds from the AD cortical samples. Incubations were performed at 400 rpm in a 37°C shaking incubator and centrifugations at 37°C. 360±12 mg of frozen brain tissue was homogenized in 9 parts cold PBS with a Dounce homogenizer by plunging both plungers A and B 25 times each in succession, after which 200 µl aliquots of the 10% (w/v) brain homogenate were dispensed into 1.5 ml microfuge tubes. For each aliquot, 2 µl of 10 mg/ml pronase E (Sigma-Aldrich) in water was added and incubated for 30 min. 4.1 µl of 0.5 M EDTA in water (pH 8.0) 206 µl of 4% (w/v) sarkosyl in Dulbecco's phosphate-buffered saline (D-PBS) lacking Ca^{2+} and Mg^{2+} (Life Technologies), and 0.83 µl of 25 U/µl benzonase nuclease (EMD Millipore) were then added. After incubating for 10 min, 33.5 µl of 4% (w/v) NaPTA (sodium phosphotungstate hydrate, Sigma-Aldrich) in water (pH 7.4) was added and incubated for 30 min. 705.3 µl of 60% (w/v) iodixanol (Optiprep™, Cosmo Bio USA) and 57. 2 µl of 4% NaPTA were added and thoroughly mixed. The sample was then centrifuged at 16,100 g for 90 min, where it yielded a small translucent pellet (P1), supernatant (SN1), and a yellowish, flocculated surface layer (SL). 1 ml of SN1 was carefully isolated from each tube and filtered through a pair of centrifugal filter units (0.45 µm pore size Durapore membrane, EMD Millipore Cat. No. UFC30HV00) at 12,000 g for 1 min. Each filter was pre-washed thrice with HPLC water by centrifugation and was used for filtering up to 1 ml of SN1. The filtered SN1 aliquots were transferred to new 1.5 ml microfuge tubes and well-mixed with an equal volume of 2% (w/v) sarkosyl in D-PBS containing 0.3% (w/v) NaPTA (pH 7.4). Following a 10 min incubation at 37°C, the samples were centrifuged for 90 min at 16,100 g. The supernatant SN2 was carefully removed and discarded, after which P2 was resuspended in 5 µl of wash buffer (17.5% (w/v) iodixanol and 0.1% (w/v) sarkosyl in D-PBS). The resuspended P2 pellets were pooled, re-dispensed into four aliquots of equal volume (~90 µl) and frozen at -80°C while awaiting further processing.

Upon thawing, 720 µl of wash buffer and 64.8 µl of 4% NaPTA were added to each resuspended P2, and the solution centrifuged at 16,100 g for 30 min to generate supernatant SN3 and a translucent pellet P3. SN3 was carefully removed and discarded, after which P3 was resuspended in 800 µl of wash buffer followed by the addition of 64.8 µl of 4% NaPTA. Samples were centrifuged at 16,100 g for 30 min and SN4 was carefully removed and discarded. The final P4 pellets were frozen at -80°C.

Thioflavin T (ThT) fluorescence

Stock solutions of Thioflavin T (AnaSpec, ultrapure grade, Cat. No. AS-88306) were prepared by dissolution to 10 mM in 10 mM phosphate buffer (pH 7.4) and the aliquots frozen at -20°C. Kinetic assays were performed using black 96-well plates with clear, flat bottoms (Corning, Cat. No. 3631) in a Biotek Synergy HT plate reader controlled by KC4 software. HFIP-treated PHF6 was reconstituted to 220 µM in 50 mM tris-HCl (pH 7.4) buffer and filtered through a pre-rinsed 0.2 µm PES filter. 200 µl of PHF6 monomers were then added to each well containing 20 µl of 20 µM seeds or fibrils and 10 µl of 100 µM ThT. Control wells had the seeds/fibrils or monomers replaced with tris buffer. The plate was sealed with film and then incubated at 37°C for an hour before ThT fluorescence was measured at 15 min intervals, where the plate was shaken for 3 seconds with the intensity set at 3 before each reading. Fluorescence was measured at the bottom of the wells with 440/20 and 485/20 nm excitation and emission filters, respectively, and sensitivity at 50. Fluorescence intensities were then divided by the intensities of the ThT-only control wells at the respective time-points. Linear fits of fluorescence values from 10 to 64 hours were performed with instrumental weighting in Origin 9 (OriginLab, Northampton, MA).

Human forebrain-specific organoid cultures

All organoid-related work, including staining and fluorescence microscopy imaging, as described in this methods section were done in collaboration with and by the Wen lab. The human iPSC lines (provided by Dr. Chadwick Hales' laboratory at Emory University) were cultured on irradiated MEFs in human iPSC medium consisting of D-MEM/F12 (Invitrogen), 20% Knockout Serum Replacement (KSR, Invitrogen), 1X Glutamax (Invitrogen), 1X MEM Non-essential Amino Acids (NEAA, Invitrogen), 100 μM β-Mercaptoethanol (Invitrogen), and 10 ng/ml human basic FGF (bFGF, PeproTech) as described by Takahashi, K. and Yamanaka, S.[32] Cortical organoids were generated as previously described[4]. Briefly, human iPSC colonies were detached from the feeder layer with 1 mg/ml collagenase treatment for 1 hour and suspended in embryonic body (EB) medium, consisting of FGF-2-free iPSC medium supplemented with 2 μM Dorsomorphin and 2 μM A-83 in non-treated polystyrene plates for 4 days with a daily medium change. On days 5-6, half of the medium was replaced with induction medium consisting of DMEM/F12, 1X N2 Supplement (Invitrogen), 10 μg/ml Heparin (Sigma), 1X Penicillin/Streptomycin, 1X Non-essential Amino Acids, 1X Glutamax, 4 ng/ml WNT-3A (R&D Systems), 1 μM CHIR99021 (Tocris), and 1 μM SB-431542 (Tocris). On day 7, organoids were embedded in Matrigel (BD Biosciences) and continued to grow in induction medium for 6 more days. On day 14, embedded organoids were mechanically dissociated from Matrigel by pipetting up and down onto the plate with a 5ml pipette tip.

Typically, 10 - 20 organoids were transferred to each well of a 12-well spinning bioreactor (SpinΩ) containing differentiation medium, consisting of DMEM/F12, 1X N2 and B27 Supplements (Invitrogen), 1X Penicillin/Streptomycin, 100 μM β- Mercaptoethanol (Invitrogen), 1X MEM NEAA, 2.5 μg/ml Insulin (Sigma). At day 71, differentiation medium was exchanged with maturation medium, consisting of Neurobasal (Gibco), 1X B27 Supplement, 1X Penicillin/Streptomycin, 1X β-Mercaptoethanol, 0.2 mM Ascorbic Acid, 20 ng/ml BDNF (Peprotech), 20 ng/ml GDNF (Peprotech), 1 ng/ml TFGβ (Peprotech), and 0.5 mM cAMP (Sigma). All media were changed every other day.

Aβ seeding and organoid immunocytochemistry

Day 84 cortical organoids were incubated with aggregates extracted from AD postmortem brains, including slow-progression AD case (A10-169) and rapid-progression AD case (A10-64) which were diluted with organoid maturation medium. After 48-hour seeding, the media were changed back to the regular maturation medium and cortical organoids were continually cultured for two more weeks. Then the cortical organoids were processed for immunocytochemistry as previously described.[4] Briefly, whole organoids were fixed in 4% Paraformaldehyde in Phosphate Buffered Saline (PBS) for 30-60 min at room temperature. Organoids were washed 3 times with PBS and then incubated in 30% sucrose solution overnight. Organoids were embedded in tissue freezing medium and sectioned at 10 μm with a cryostat (Leica). For immunostaining, freezing medium was washed with PBS before permeabilization with 0.2% Triton-X in PBS for 1 hr. Tissues were then blocked with blocking medium consisting of 10% donkey serum in PBS with 0.1% Tween-20 (PBST) for 30 min. Primary antibodies diluted in blocking solution were applied to the sections overnight at 4°C. The following primary antibodies were used:

anti-pTau (S369) (Rabbit; 1:500; ThermoFisher), and anti-Tau (Mouse; 1:500; ThermoFisher). After washing with PBST, secondary antibodies diluted in blocking solution were applied to the sections for 1hr at room temperature. Finally, sections were washed with PBST and stained with DAPI. All images were captured by Nikon Eclipse Ti-E microscope with the same settings by researchers blind to experimental condition. Quantitative analyses were conducted on randomly picked cortical structures in a blind fashion using ImageJ software (NIH).[57] For pTau/Tau immunoreactivity, the mean intensity of pTau and total Tau of the entire image was measured, and the ratio of pTau/Tau was calculated and plotted as fold increase compared to control cortical organoids without brain aggregate treatment.

References

1. Heuer, E., et al., *Nonhuman primate models of Alzheimer-like cerebral proteopathy*. Curr Pharm Des, 2012. **18**(8): p. 1159-69.
2. Kelleher, R.J., 3rd and J. Shen, *Presenilin-1 mutations and Alzheimer's disease*. Proc Natl Acad Sci U S A, 2017. **114**(4): p. 629-631.
3. *2023 Special Report: Alzheimer's Disease Facts and Figures*. 2023.
4. Qian, X., et al., *Brain-Region-Specific Organoids Using Mini-bioreactors for Modeling ZIKV Exposure*. Cell, 2016. **165**(5): p. 1238-1254.
5. Barthel, H., et al., *Cerebral amyloid-β PET with florbetaben (18F) in patients with Alzheimer's disease and healthy controls: a multicentre phase 2 diagnostic study*. Lancet Neurol, 2011. **10**(5): p. 424-35.
6. Liu, C.C., et al., *Apolipoprotein E and Alzheimer disease: risk, mechanisms and therapy*. Nat Rev Neurol, 2013. **9**(2): p. 106-18.
7. Kanekiyo, T., H. Xu, and G. Bu, *ApoE and Aβ in Alzheimer's disease: accidental encounters or partners?* Neuron, 2014. **81**(4): p. 740-54.
8. Huang, Y. and R.W. Mahley, *Apolipoprotein E: structure and function in lipid metabolism, neurobiology, and Alzheimer's diseases*. Neurobiol Dis, 2014. **72 Pt A**: p. 3-12.
9. Tahami Monfared, A.A., et al., *Alzheimer's Disease: Epidemiology and Clinical Progression*. Neurology and Therapy, 2022. **11**(2): p. 553-569.
10. Johnstone, E.M., et al., *Conservation of the sequence of the Alzheimer's disease amyloid peptide in dog, polar bear and five other mammals by cross-species polymerase chain reaction analysis*. Brain Res Mol Brain Res, 1991. **10**(4): p. 299-305.

11. Chen, G.F., et al., *Amyloid beta: structure, biology and structure-based therapeutic development*. Acta Pharmacol Sin, 2017. **38**(9): p. 1205-1235.

12. Zhao, J., et al., *Targeting Amyloidogenic Processing of APP in Alzheimer's Disease*. Frontiers in Molecular Neuroscience, 2020. **13**.

13. Zhang, L., et al., *Optimized negative-staining electron microscopy for lipoprotein studies*. Biochim Biophys Acta, 2013. **1830**(1): p. 2150-9.

14. Haass, C. and D. Selkoe, *If amyloid drives Alzheimer disease, why have anti-amyloid therapies not yet slowed cognitive decline?* PLoS Biol, 2022. **20**(7): p. e3001694.

15. Shi, M., et al., *Impact of Anti-amyloid-β Monoclonal Antibodies on the Pathology and Clinical Profile of Alzheimer's Disease: A Focus on Aducanumab and Lecanemab*. Front Aging Neurosci, 2022. **14**: p. 870517.

16. CORBO, R.M. and R. SCACCHI, *Apolipoprotein E (APOE) allele distribution in the world. Is APOE*4 a 'thrifty' allele?* Annals of Human Genetics, 1999. **63**(4): p. 301-310.

17. Frisoni, G.B., et al., *The prevalence of apoE-ε4 in Alzheimer's disease is age dependent*. Journal of Neurology, Neurosurgery & Psychiatry, 1998. **65**(1): p. 103-106.

18. LaDu, M.J., et al., *Apolipoprotein E and apolipoprotein E receptors modulate A beta-induced glial neuroinflammatory responses*. Neurochem Int, 2001. **39**(5-6): p. 427-34.

19. Lynch, J.R., et al., *Apolipoprotein E modulates glial activation and the endogenous central nervous system inflammatory response*. J Neuroimmunol, 2001. **114**(1-2): p. 107-13.

20. Petkova, A.T., et al., *Self-Propagating, Molecular-Level Polymorphism in Alzheimer's ß-Amyloid Fibrils*. Science, 2005. **307**(5707): p. 262-265.

21. Alberti, S., et al., *Granulostasis: Protein Quality Control of RNP Granules.* Front Mol Neurosci, 2017. **10**: p. 84.

22. Matchett, B.J., et al., *The mechanistic link between selective vulnerability of the locus coeruleus and neurodegeneration in Alzheimer's disease.* Acta Neuropathologica, 2021. **141**(5): p. 631-650.

23. Flores-Aguilar, L., et al., *Early loss of locus coeruleus innervation promotes cognitive and neuropathological changes before amyloid plaque deposition in a transgenic rat model of Alzheimer's disease.* Neuropathol Appl Neurobiol, 2022. **48**(6): p. e12835.

24. Feinstein, D.L., S. Kalinin, and D. Braun, *Causes, consequences, and cures for neuroinflammation mediated via the locus coeruleus: noradrenergic signaling system.* J Neurochem, 2016. **139 Suppl 2**: p. 154-178.

25. Braak, H. and K. Del Tredici, *The pathological process underlying Alzheimer's disease in individuals under thirty*. Acta Neuropathol, 2011. **121**(2): p. 171-81.

26. Satoh, A. and K.M. Iijima, *Roles of tau pathology in the locus coeruleus (LC) in age-associated pathophysiology and Alzheimer's disease pathogenesis: Potential strategies to protect the LC against aging*. Brain Res, 2019. **1702**: p. 17-28.

27. Li, D.-W., et al., *Formation and Growth of Oligomers: A Monte Carlo Study of an Amyloid Tau Fragment*. PLOS Computational Biology, 2008. **4**(12): p. e1000238.

28. Gong, C.X. and K. Iqbal, *Hyperphosphorylation of microtubule-associated protein tau: a promising therapeutic target for Alzheimer disease.* Curr Med Chem, 2008. **15**(23): p. 2321-8.

29. Walker, L.C. and M. Jucker, *The Exceptional Vulnerability of Humans to Alzheimer's Disease*. Trends Mol Med, 2017. **23**(6): p. 534-545.

30. Edler, M.K., et al., *Aged chimpanzees exhibit pathologic hallmarks of Alzheimer's disease*. Neurobiol Aging, 2017. **59**: p. 107-120.

31. Martin, E.W., et al., *Valence and patterning of aromatic residues determine the phase behavior of prion-like domains*. Science, 2020. **367**(6478): p. 694-699.

32. Takahashi, K. and S. Yamanaka, *Induction of pluripotent stem cells from mouse embryonic and adult fibroblast cultures by defined factors*. Cell, 2006. **126**(4): p. 663-76.

33. Wen, Z., et al., *Synaptic dysregulation in a human iPS cell model of mental disorders*. Nature, 2014. **515**(7527): p. 414-418.

34. Goate, A., et al., *Segregation of a missense mutation in the amyloid precursor protein gene with familial Alzheimer's disease*. Nature, 1991. **349**(6311): p. 704-6.

35. *Molecular classification of Alzheimer's disease*. Lancet, 1991. **337**(8753): p. 1342-3.

36. Campion, D., et al., *Mutations of the presenilin I gene in families with early-onset Alzheimer's disease*. Hum Mol Genet, 1995. **4**(12): p. 2373-7.

37. Campion, D., et al., *Early-onset autosomal dominant Alzheimer disease: prevalence, genetic heterogeneity, and mutation spectrum*. Am J Hum Genet, 1999. **65**(3): p. 664-70.

38. Wenborn, A., et al., *A novel and rapid method for obtaining high titre intact prion strains from mammalian brain*. Scientific Reports, 2015. **5**(1): p. 10062.

39. Shaked, G.M., et al., *Protease-resistant and detergent-insoluble prion protein is not necessarily associated with prion infectivity*. J Biol Chem, 1999. **274**(25): p. 17981-6.

40. Yuan, J., et al., *Insoluble aggregates and protease-resistant conformers of prion protein in uninfected human brains*. J Biol Chem, 2006. **281**(46): p. 34848-58.

41. Jin, K., et al., *Enhanced neurogenesis in Alzheimer's disease transgenic (PDGF-APPSw,Ind) mice*. Proc Natl Acad Sci U S A, 2004. **101**(36): p. 13363-7.

42. López-Toledano, M.A. and M.L. Shelanski, *Increased Neurogenesis in Young Transgenic Mice Overexpressing Human APP Sw,Ind*. Journal of Alzheimer's Disease, 2007. **12**: p. 229-240.

43. Ganguly, P., et al., *Tau assembly: the dominant role of PHF6 (VQIVYK) in microtubule binding region repeat R3*. J Phys Chem B, 2015. **119**(13): p. 4582-93.

44. Buée, L., et al., *Tau protein isoforms, phosphorylation and role in neurodegenerative disorders*. Brain Res Brain Res Rev, 2000. **33**(1): p. 95-130.

45. von Bergen, M., et al., *Tau aggregation is driven by a transition from random coil to beta sheet structure*. Biochim Biophys Acta, 2005. **1739**(2-3): p. 158-66.

46. Daebel, V., et al., *β-Sheet Core of Tau Paired Helical Filaments Revealed by Solid-State NMR*. Journal of the American Chemical Society, 2012. **134**(34): p. 13982-13989.

47. Balbach, J.J., et al., *Amyloid fibril formation by A beta 16-22, a seven-residue fragment of the Alzheimer's beta-amyloid peptide, and structural characterization by solid state NMR*. Biochemistry, 2000. **39**(45): p. 13748-59.

48. Lu, K., et al., *Exploiting amyloid fibril lamination for nanotube self-assembly*. J Am Chem Soc, 2003. **125**(21): p. 6391-3.

49. Ladiwala, A.R., et al., *Conformational differences between two amyloid β oligomers of similar size and dissimilar toxicity*. J Biol Chem, 2012. **287**(29): p. 24765-73.

50. Passarella, D. and M. Goedert, *Beta-sheet assembly of Tau and neurodegeneration in Drosophila melanogaster*. Neurobiol Aging, 2018. **72**: p. 98-105.

51. Hsieh, M.C., et al., *Multistep Conformation Selection in Amyloid Assembly*. J Am Chem Soc, 2017. **139**(47): p. 17007-17010.

52. Li, X., et al., *Mechanistic insight into E22Q-mutation-induced antiparallel-to-parallel β-sheet transition of Aβ16−22 fibrils: an all-atom simulation study*. Physical Chemistry Chemical Physics, 2019. **21**(28): p. 15686-15694.

53. Li, S., et al., *Design of Asymmetric Peptide Bilayer Membranes*. J Am Chem Soc, 2016. **138**(10): p. 3579-86.

54. Bentley, N.M., et al., *Apolipoprotein E structural requirements for the formation of SDS-stable complexes with beta-amyloid-(1-40): the role of salt bridges*. Biochem J, 2002. **366**(Pt 1): p. 273-9.

55. Zhang, L., et al., *Morphology and structure of lipoproteins revealed by an optimized negative-staining protocol of electron microscopy*. J Lipid Res, 2011. **52**(1): p. 175-84.

56. Ryan, T.M., et al., *Ammonium hydroxide treatment of Aβ produces an aggregate free solution suitable for biophysical and cell culture characterization*. PeerJ, 2013. **1**: p. e73.

57. Schneider, C.A., W.S. Rasband, and K.W. Eliceiri, *NIH Image to ImageJ: 25 years of image analysis*. Nature Methods, 2012. **9**(7): p. 671-675.

Chapter 2: Two-step nucleation in paracrystalline assemblies

The liquid-to-solid phase transition is a phenomenon commonly referred to as crystallization, where external factors like temperature, pressure, and polarity can influence the solubility of a solute, and this continuous decrease in solubility results in the compaction of individual solute atoms to organize into highly organized crystal units. One model that has been developed to further describe this phenomenon is the two-step nucleation, where freely floating monomers associate through hydrophobic collapse, which result in these monomers to locally concentrate. Increased presence of these monomers induces a more solid-like species, where internal environments encourage the ordering of the monomers by restricting their movements. Thus, this phase funnels all the monomers towards a specific orientation, from which the rest of the monomers could then follow to achieve the crystalline structures. The following is a review of such a phenomenon as replicated by the previously characterized disease relevant peptides Aβ42 and PHF6 which can produce paracrystalline assemblies, or structures with medium-range order, which have been observed in biological systems and in empirical setting. While the rules that govern a peptide assembly pathway's sensitivity to the nucleus orientation is not yet known, understanding how different external factors like pH could influence peptide self-organization may shed light on this elusive mechanism.

Chapter 2.1: Intrinsically disordered proteins as an extension of Anfinsen's Dogma

The classic demonstration of stepwise RNase A denaturation to scramble its disulfide bonds, which hampers the enzyme's ability to cleave RNA, was done by Christian

Anfinsen, who established the structure-function paradigm in proteins.[3] A class of proteins known as intrinsically disordered proteins (IDPs) could be seen as an extension of this dogma – by exploiting the structural flexibility of their disordered domains, IDPs can sample a variety of configurations, allowing them to associate with different binding partners and to exert distinct functions. An essential IDP that is commonly dubbed as "guardian of the genome," p53 plays a key role in all manners of gene quality control, from recognition of DNA damage, arresting cell growth, and even inducing apoptosis.[ref] It is no surprise, then, that p53 exploits its intrinsic disorder to participate in all these regulatory functions. In healthy cells, p53 is expressed at low levels and deactivated by MDM2, but in the event of stress-induced DNA damage, p53 can quickly dissociate from MDM2 and instead bind with DNA to signal other proteins for repair (Figure 2.1).[1, 4] Directly probing these protein-protein or protein-DNA interactions would require knowing what binding partners to test ahead of time, but what about investigating interactions with other moieties that have not yet been established? In this case, a bottom-up approach which seeks to define rules that IDPs follow to modulate their interactions with different biopolymers could shed light on previously unknown interactions.

Amyloid beta-42 (Aβ42) is an intrinsically disordered peptide associated with Alzheimer's Disease (AD) and is a peptide that exists in various isoforms, which tune their solubility. Previously, it was thought that the insoluble form of Aβ aggregates was what caused the neurotoxicity, and that its accumulation in plaques may be causing cognitive decline. Recent investigations, including those that involve the FDA-approved drug aducanumab, showed that even clearance of such insoluble plaques did not improve cognitive function in patients diagnosed with dementia and mild cognitive impairments.

These findings suggest that perhaps it was the soluble and not the insoluble aggregates that could be neurotoxic. While the mechanistic details of how or even whether this peptide contributes to neurotoxicity remain unresolved, Aβ42 does have to prefer β-sheet conformation to induce neurotoxicity. The propensity for β-sheet configuration can be narrowed down to the 17th to 21st residues LVFFA, which are bookended by positively charged K and negatively charged E, which can associate with the same domain on another Aβ42 strand to form intermolecular cross-β fibrils.[5-9]

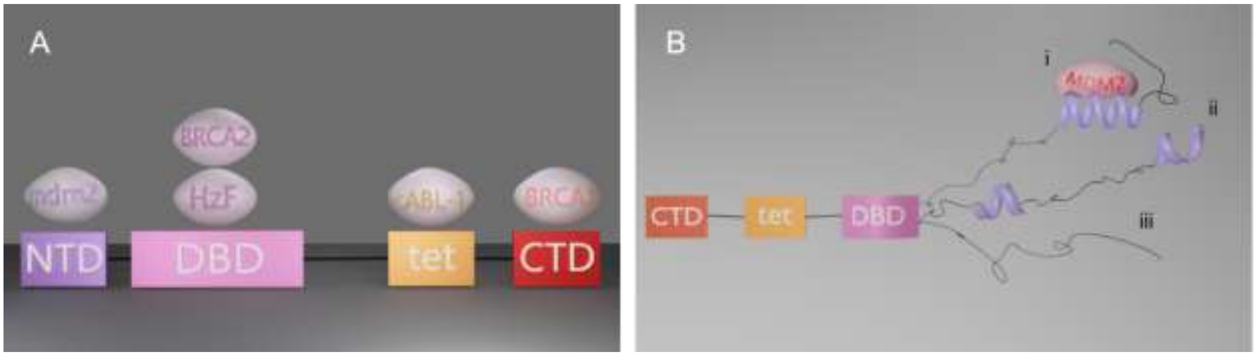

Figure 2.5 Illustration of the variety of binding partners p53 is known to interact with, drawn as white pearls. p53, here, is sub-divided in to 4 domains: N-terminal (NTD, purple), DNA-binding (DBD, pink), tetramerization (tet, yellow), and C-terminal domains (CTD, red). The intrinsically disordered N-terminus is shown to be sampling a variety of transient helicities (i-iii), where the strongest helical propensity (i) could bind with MDM2. Figure is adapted from Gordon, C. et al.[1]

Upon truncation to just the 16th to 22nd residues to make KLVFFAE (E22) or the 14th to 21st residues to make HHQALVFFA (K16A), these short peptides still have high propensity for cross-β architecture to form paracrystalline fibrils. These assemblies are sensitive to external stimuli like pH changes and metal additions, which induce the peptides to undergo global structural re-configurations.[2, 10] The sensitivity and dynamics of these assemblies make such short peptides a great candidate for modeling disordered domains to establish guidelines for their interactions, akin to the sticker-spacer model which classify protein residues by their “sticker” or “spacer” character and how they play a role in induction of phase separation.[11]

Chapter 2.2: Limiting conformational space for sampling

It is thought that the phase separation that IDP clusters undergo improves spatial control over conformational sampling. Empirical data have shown that the internal condensate environment is distinct from solvent conditions and that this difference accounts for the boundaries around each biomolecular condensate despite it lacking true membranes.[12-15] The crowded nature of these condensates imposes physical constraints on the disordered region’s degree of freedom as well as slowing down the overall motion of the proteins inside, increasing the duration time for conformational sampling, which could allow for higher probability to associate with their binding partners. This hypothesis is commonly demonstrated by the nucleolus, a transient membraneless organelle responsible for ribosome synthesis, is composed of 3 sub-compartments that are only divided by distinct biophysical properties like their viscosities. Each of these spaces are occupied by different DNA- or RNA-binding proteins and their associated DNA or RNA and are responsible for different functions: the fibrillar center participates in rDNA transcription, the dense fibrillar component participates in rRNA processing, and the granular components facilitates ribosome assembly.[15, 16] [ref]

Much like the nucleolus example, peptide monomers in solution will move freely upon dissolution and begin to localize into small clusters to maximize hydrophobic interactions, which drive solvent out of these clusters, forming biopolymer condensates. The environment within these condensates, although restrictive, will still allow for some degree of conformational sampling. However, unlike the nucleolus example, where condensates do not then undergo liquid-solid phase transition, the conformation that is most occupied within peptide condensates will reach a critical threshold to undergo a phase transition. If we viewed the most frequently sampled conformation within the condensate as a "nucleus" which seeds the subsequent paracrystalline assemblies, we can then ask the question of how such a nucleus could be stabilized, and whether environmental factors like pH or salinity could play a role in nucleus stabilization.

Chapter 2.3: Stabilizing a nucleus

E22, which also undergoes 2-step nucleation events, forms heterogeneous higher order structures at initial timepoints when dissolved in an acetonitrile/water environment.[10] These heterogeneous structures, which include particles, fibers, sheets, and ribbons (Figures 2.2 a,e), at these early timepoints highlight the different nuclei that were propagated out of the particle phase. Conformations most stabilized within the particles may not be favored in the free solvent environment, as seen in the proceeding days after initial dissolution, where one single morphology predominates the entire TEM grid (Figures 2.2 d,h). These micrographs also suggest that external solvent environment, that is the space outside of the particles, contributes significantly to nucleus stability once the assembly undergoes liquid-solid phase transition (Figures 2.2 b-c, f-g). The nucleus most favored by the free solvent, fibers at neutral pH and nanotubes at acidic pH, predominates the overall morphological population and act as a seed for other nuclei, which had formed unfavorable paracrystalline assemblies. These unfavorable assemblies disassemble into peptide monomers and undergo the 2-step nucleation process again – this time with a strong nucleus that already exists as paracrystalline assemblies.

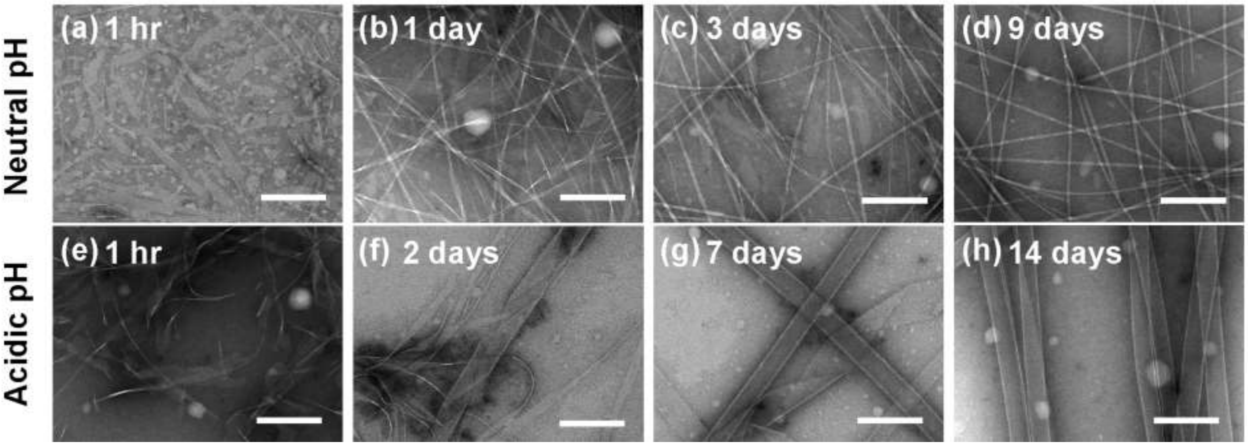

Figure 2.6 Ac-KLVFFAE-NH_2 (E22) nucleation is impacted by pH. E22 samples different conformations at early timepoints (**a-b, e-f**), and external solvent conditions contribute to stabilizing nucleus for fibrillar assembly at neutral pH (**a-d**) or nanotube assembly (**e-h**). Scale bars are 200 nm. Panels are adapted from Hsieh, M. et al.[2]

The overall morphological differences in the two environments could be attributed to the forces that favor electrostatic complementarity across Lys and Glu residues in neutral pH or hydrophobic interactions across Val, Ala, and Phe residues in acidic pH, where Glu is charge neutral (Figures 2.3 a,b). This hypothesis was tested through isotope-edited infrared (IE-IR) spectroscopy, where the use of isotopically labeled Phe, [1-^{13}C]F, was used to generate Ac-KLV[1-^{13}C]FFAE-NH_2 as well as Ac-KLV[1-^{13}C]FFAQ-NH_2. Because IR spectroscopy relies on the vibrational modes of molecules that produce a dipole moment, this technique is sensitive to isotopic substitutions, which directly impact vibrational frequencies of the substituted element. Vibrations on C=O and N-H bonds, known as Amide I and Amide II, respectively, both produce a dipole moment, which make them an important marker to establish peptide configuration. Upon heavy isotope substitution, the Amide I stretch, which has been reported to be at ~1650cm^{-1}, will be split and red-shifted. This splitting is due to the existence of 2 hydrogen-bound populations consisting of ^{12}C=O and ^{13}C=O that each interact with N-H bonds, while the bathochromic shift is attributed to the higher isotopic mass lowering the normal mode frequency.

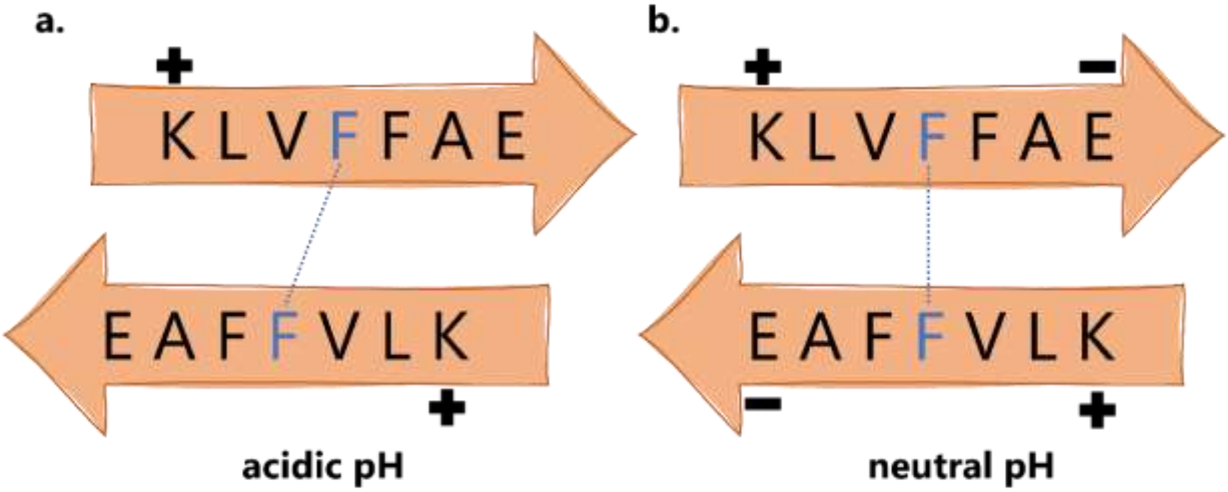

Figure 2.7 pH influences E22 sheet orientation. Ac-KLV[1-^{13}C]FFAE forms either antiparallel, out-of-register β-sheets at acidic pH (a) or antiparallel, in-register β-sheets at neutral pH (b). The blue "F" indicates the ^{13}C label on the first phenylalanine residue. Depending on the configuration, in- or out-of-registry, the distances between the two isotopes differ and can be measured via IR spectroscopy.

A quick scan to establish the basis sets for parallel, antiparallel in-register, antiparallel out-of-register, and unassembled peptides were done by assembling Ac-KLV[1-^{13}C]FFAQ-NH$_2$ in neutral pH, Ac-KLV[1-^{13}C]FFAE-NH$_2$ in neutral pH, Ac-KLV[1-^{13}C]FFAE-NH$_2$ in acidic pH, and Ac-KLV[1-^{13}C]FFAE-NH$_2$ with 1,1,1,3,3,3-hexafluoroisopropanol (HFIP), respectively. Ac-KLV[1-^{13}C]FFAQ-NH$_2$ is known to assemble as parallel β-sheets, owing to the hydrogen bonding propensity of Gln residues, commonly referred to as “Q-tract.” HFIP is an agent known to significantly interfere with biopolymer assemblies, preventing them from achieving extended order by disrupting hydrogen bonding among the peptides, thus ensuring free, unassembled peptides. Following the electrostatic complementarity hypothesis, we can then suppose that at neutral pH, where Glu is deprotonated, Ac-KLV[1-^{13}C]FFAE-NH$_2$ forms anti-parallel, in-register β-sheets, and that at acidic pH, where Glu is protonated, Ac-KLV[1-^{13}C]FFAE-NH$_2$ forms antiparallel, out-of-register β-sheets, as illustrated in Figure 2.4. These basis sets were then used to deconvolute Ac-KLV[1-^{13}C]FFAE-NH$_2$ assemblies at both neutral and acidic pH over time (Figures 2.5).

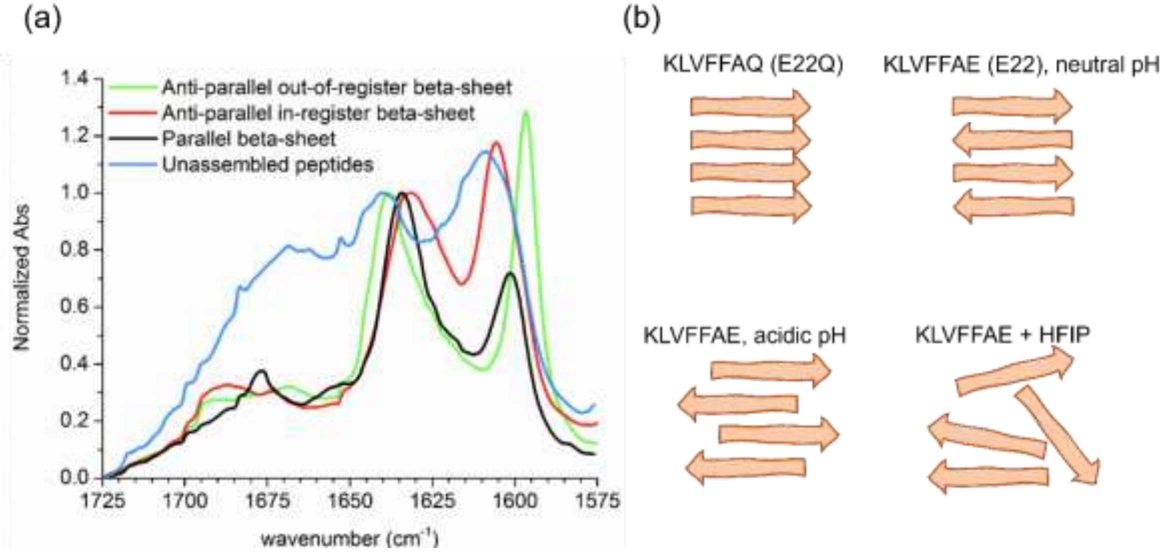

Figure 2.8 Different E22 congeners can adopt distinct sheet orientation. (a) Basis sets establishing peak splitting profiles in parallel (E22Q, black line), antiparallel (E22, neutral pH, red line), antiparallel out-of-register (E22, acidic pH, green line), and unassembled peptides (E22 with HFIP, blue line). (b) Illustrations of the distinct β-sheet orientation with each peptide. Panel (a) is adapted from Hsieh, M., et al.[2]

Deconvolution of Ac-KLV[1-^{13}C]FFAE-NH$_2$ assemblies at neutral pH revealed that, although the antiparallel, out-of-registry configuration predominates the initial timepoints, this configuration does not remain throughout the entire course of assembly; rather, the out-of-registry profile decreases at the midpoint, while antiparallel, in-registry configuration begins to appear and later dominates the overall IR profile (Figures 2.5 c, d). In the neutral pH case, the out-of-registry configuration could be viewed as a kinetically stable structure that is stabilized by the hydrophobic internal environment within the particles, thus favoring the hydrophobic interactions along the residues, while the in-registry configuration is the thermodynamically stable structure stabilized by the free solvent conditions, where electrostatic complementarity is favored. On the other hand, there does not appear to be a significant global registry change. Much like E22 assembled at neutral pH, initial timepoints reveal a predominantly out-of-registry profile and trace populations of other configurations present. These trace populations disappear over time, leaving only the antiparallel, out-of-registry component to dominate. Overall, this phenomenon corroborates the idea that a nucleus favored within the particle may not be favored in the free solvent. Since the low pH of the solvent would protonate the Glu residue, there is no electrostatic complementarity that would outcompete the interactions of the more hydrophobic residues of the peptide.

The dynamics of peptide assemblies and this nucleus selection is not exclusive to E22. As it has been shown, congeners of E22, such as H-HHQALVFFA-NH$_2$ (K16A) and Pep-KG (Ac-KLVIIAG-NH$_2$) can also have distinct nuclei that can be captured by a binding partner like metal ions and oligonucleotides to propagate morphologies wholly different from the peptides when assembled on their own. The following thesis is a series of observations of just how dynamic and structurally plastic these cross-β architectures can be. While higher order structures achieved by clusters of IDPs to form condensates or even whole transcriptomes do not constitute cross-β architecture, understanding how subtle changes in a biopolymer's environment will allow us to better understand the code which rule over conformational selection in such phenomena.

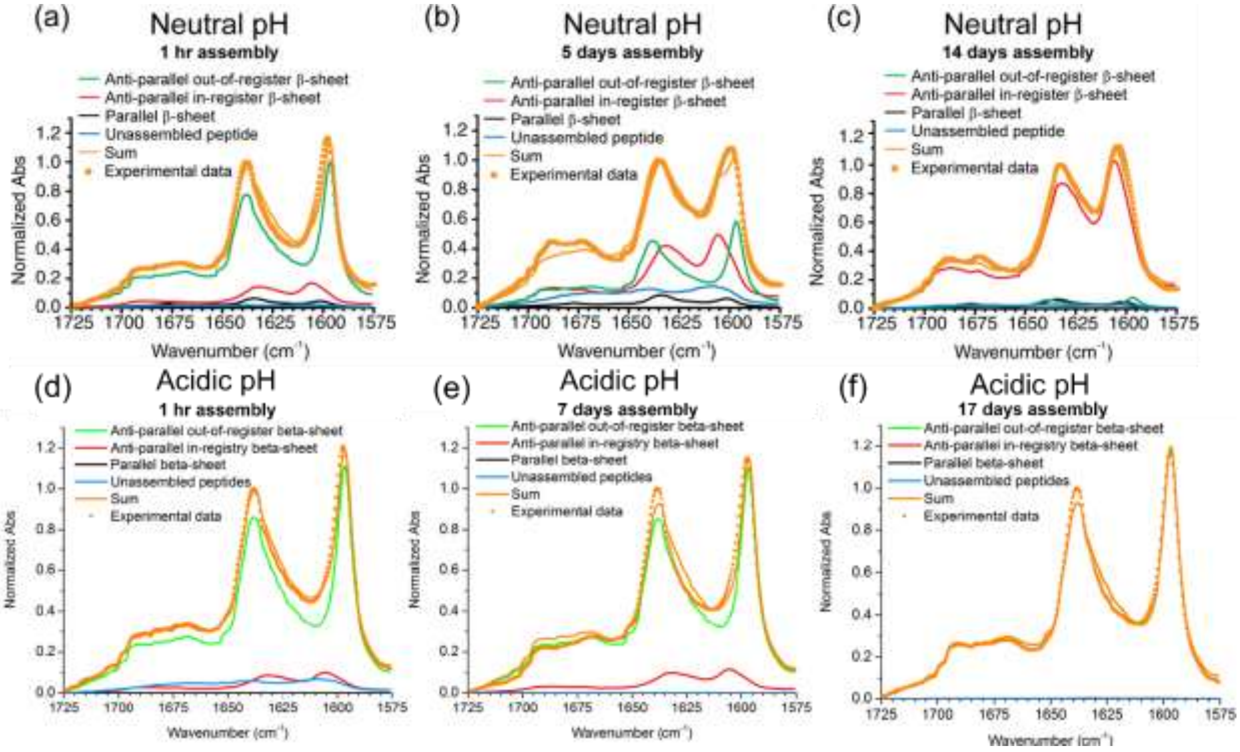

Figure 2.9 β-sheet configurations adopted by different truncated Aβ congeners produce distinct IR profiles. (a, d) E22 assembled in either neutral or acidic conditions reveal predominantly antiparallel, out-of-register configurations at initial timepoints, but those assembled at neutral pH experience a dramatic shift over time to form mostly antiparallel, in-register configuration (b, e), while those assembled at acidic conditions remain as antiparallel, out-of-register configurations (c, f). Panels are adapted from Hsieh, M., et al.[2]

References

1. Gordon, C.K., R. Luu, and D. Lynn, *Capturing nested information from disordered peptide phases*. Peptide Science, 2021. **113**(2): p. e24215.
2. Hsieh, M.C., et al., *Multistep Conformation Selection in Amyloid Assembly*. J Am Chem Soc, 2017. **139**(47): p. 17007-17010.
3. Anfinsen, C.B., et al., *THE KINETICS OF FORMATION OF NATIVE RIBONUCLEASE DURING OXIDATION OF THE REDUCED POLYPEPTIDE CHAIN*. Proceedings of the National Academy of Sciences, 1961. **47**(9): p. 1309-1314.
4. Kim, D.H., et al., *The Mechanism of p53 Rescue by SUSP4*. Angew Chem Int Ed Engl, 2017. **56**(5): p. 1278-1282.
5. Johnstone, E.M., et al., *Conservation of the sequence of the Alzheimer's disease amyloid peptide in dog, polar bear and five other mammals by cross-species polymerase chain reaction analysis*. Brain Res Mol Brain Res, 1991. **10**(4): p. 299-305.
6. Balbach, J.J., et al., *Amyloid fibril formation by A beta 16-22, a seven-residue fragment of the Alzheimer's beta-amyloid peptide, and structural characterization by solid state NMR*. Biochemistry, 2000. **39**(45): p. 13748-59.
7. Lakdawala, A.S., et al., *Dynamics and fluidity of amyloid fibrils: a model of fibrous protein aggregates*. J Am Chem Soc, 2002. **124**(51): p. 15150-1.
8. Mehta, A.K., et al., *Facial symmetry in protein self-assembly*. J Am Chem Soc, 2008. **130**(30): p. 9829-35.

9. Liang, Y., et al., *Cross-strand pairing and amyloid assembly*. Biochemistry, 2008. **47**(38): p. 10018-26.

10. Hsieh, M.-C., et al., *Multistep Conformation Selection in Amyloid Assembly*. Journal of the American Chemical Society, 2017. **139**(47): p. 17007-17010.

11. Martin, E.W., et al., *Valence and patterning of aromatic residues determine the phase behavior of prion-like domains*. Science, 2020. **367**(6478): p. 694-699.

12. Shin, Y. and C.P. Brangwynne, *Liquid phase condensation in cell physiology and disease*. Science, 2017. **357**(6357).

13. Wang, J., et al., *A Molecular Grammar Governing the Driving Forces for Phase Separation of Prion-like RNA Binding Proteins*. Cell, 2018. **174**(3): p. 688-699.e16.

14. Boeynaems, S., et al., *Spontaneous driving forces give rise to protein-RNA condensates with coexisting phases and complex material properties*. Proc Natl Acad Sci U S A, 2019. **116**(16): p. 7889-7898.

15. Feric, M., et al., *Coexisting Liquid Phases Underlie Nucleolar Subcompartments*. Cell, 2016. **165**(7): p. 1686-1697.

16. Alberti, S., et al., *Granulostasis: Protein Quality Control of RNP Granules*. Front Mol Neurosci, 2017. **10**: p. 84.

Chapter 3: Generalized rules for peptide assemblies as informed by disease-relevant peptides

Original text: Gordon, C.K., R. Luu, and D. Lynn, *Capturing nested information from disordered peptide phases*. Peptide Science, 2021. **113**(2): p. e24215

Experiments involving specific biomarkers often associated with AD pathology have informed some rules that govern biopolymer associations. For example, shared structural motifs could dictate whether two polypeptides could associate in a mutualistic way. Even simplified peptides that were stripped down to only their β-sheet motifs were enough to propagate highly stable paracrystalline structures. Clearly, this cross-β structure plays an important role for cross-polymer associations, and as it turns out, the initial β-sheet orientation, in either parallel or antiparallel, could significantly modulate the assembly pathways. To further expand on these rules, a better understanding of the nucleation pathway is needed.

Chapter 3.1: Energetic contributions regulating cross-β assembly

For peptides, the growth of cross-β assemblies occurs along three distinct surfaces: (a) the registry and orientation of backbone H-bonding depends on side-chain cross-strand pairing in a fashion energetically related to nucleic acid base-pairing; (b) sheet-sheet stacking energetics driven by sheet-facial complementarity,[3] analogous to base-pair stacking in nucleic acid duplexes; and (c) the charged external surface of cross-β assemblies that results from precisely stacked sheets, much like the surface phosphates of nucleic acid duplexes that regulate higher-order aggregation. As in nucleic acids, all three surfaces contribute to templating assembly, with π-stacking and H-bonding among nucleobases dominating the association energetics in nucleic acid templated assemblies.[4, 5] Others and we have explored the cross-β determinants using simple synthetic substitutions within the nucleating core of the Aβ peptide of Alzheimer's disease to regulate assembly. Molecular modeling grounded the suggestion that amino acid substitution could impact cross-strand pairing within the cross-β laminate to control registry of the β-sheet.[6] Extending those models to incorporate pyrimidine-pyrimidine base pairing led to an i-motif stabilizing the 1 nm leaflet spacing to give homogeneous nanotubes.[7] Sheet surface complementarity proved to be critical for the control of fiber, ribbon, and nanotube morphology[8, 9] and can be understood through the tensions associated with leaflet curvature.[10] However, the most impactful determinant of assembled architecture proved to be the associations of the external surfaces of the cross-β leaflets. As shown in Figure 3.1, peptides differing by a single methylene (Ac-KLVFFAL-NH_2 vs Ac-KLVFFAV-NH_2) at the C-terminus give nanotubes with drastically different

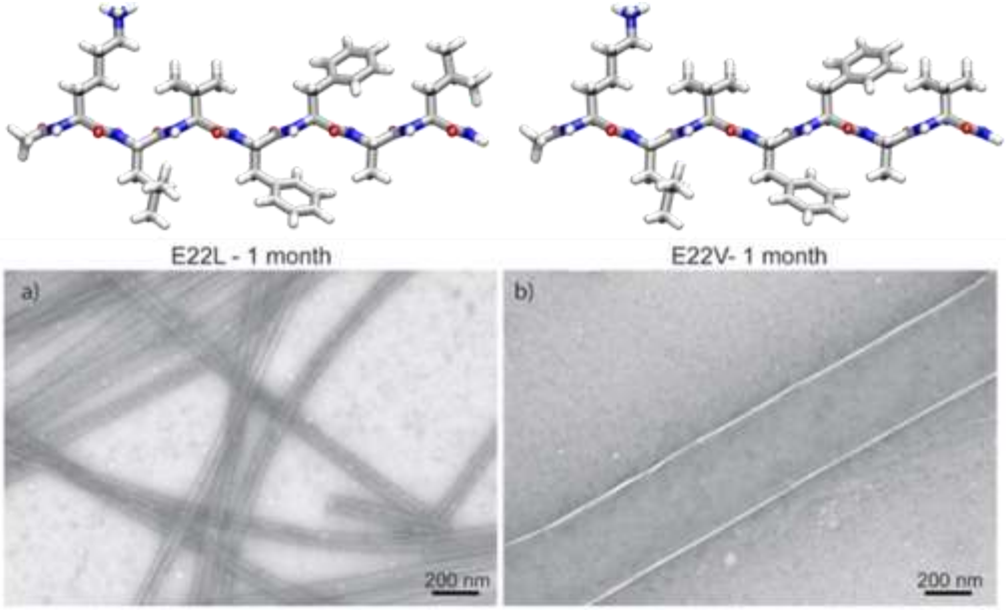

Figure 3.10 TEM micrographs of, A, Ac-KLVFFAE-NH2 and, B, Ac-KLVFFAV-NH2 peptides (1.3 mM) assembled at acidic pH in 40% MeCN and 0.1% TFA. The nanotube diameters registered at 38 and 278 nm, respectively. Modified from Gordon, C. et al.[1]

diameters. When mixed, these peptides assemble separately, giving the same two nanotubes. This observation suggests that this subtle change in structure controls the nucleation at the leaflet interface that propagates into the distinct nanotubes.

Chapter 3.2: The assembly pathway

With nucleation energetics regulating structural specificity, understanding the entire peptide assembly pathway may lead to regulation strategies for the templated information. Initial molecular simulations had highlighting strand dynamics of these peptides in solution,[11] and careful evaluation of early timepoints identified two-step nucleation through LLPS, resulting in condensates similar to the nucleolus case previously mentioned.[4, 12] Much like the distinct biophysical properties exhibited by the three subcompartments of a nucleolus, these early solute-rich phases provide a distinct environment that favors condensation reactions in aqueous media.[13] Reducing the C-terminus of a tripeptide to the aldehyde, NFF-CHO, indeed generates a dynamic chemical condensation network in where the aldehyde captures the N-terminal asparagine side chain of another monomer to make an N,N-acetal dimer.[13] This dynamic network further oligomerizes, and at a critical concentration, nucleates the solute-rich phase transition. The resulting growing particle phase allows for further chain-length extension via acetal polymerization, and at another critical threshold, a stable cross-β nucleus forms and autocatalytically templates a homochiral monodisperse peptide oligomer as the exclusive product. The diversity of nuclei forming within the LLPS state has been explored spectroscopically with another peptide, H-HHQALVFFA-NH_2, that forms particles suitable for detailed analyses.[14] As shown in Figure 3.2, multiple single β-sheets exist in the initial particle phase, but based on the energetics outlined above, only a single cross-β nucleus propagates from what appears to be a dynamic mixture of competing single sheets. To the extent that this level of dynamic preordered nuclei generally exists in these LLPS peptide phases, they could cooperatively bind to external templates. Seeding LLPS particles with pre-assembled peptide templates has been generally used for selective propagation of cross-β assemblies,[13] consistent with this mechanism for efficient IDP recognition of distinct ligands through local preordered nuclei. Unlike p53 that reversibly binds distinct templates, these short peptides propagate the selected nucleus, amplifying the information as shown in Figure 3.2. Such nucleation events remain reversible as propagation in solution, a very different physical environment relative to the LLPS where the stable nucleus originates, allows for conformational mutation via the propagation of defects that appear due to changes in cross-β packing energetics as the fiber propagates beyond the particle and into solution.[15, 16] So, these fibrous assemblies also remain dynamic with the cross-β assembly susceptible to feedback structural plasticity at the growing ends. The resulting fibrous surfaces of the cross-β assemblies also change with these conformational mutations, adding specificity to the feedback, including as a template capable of directed oligomerization of other substrates.[3] The peptide Ac-KLVFFAL-NH2 self-assembles into nanotubes, creating a surface lined with recessed hydrophobic grooves formed from anti-parallel, out-of-register β-sheets. This surface binds aromatic substrates along the template. In this case, the aromatic residues are proximal to a lysine residue which has been shown to catalyze retro-aldol carbon-carbon cleavage as well as imine condensation polymerization.[3] Such reactions have the potential to operate within a cooperative network, providing an opportunity for positive and/or negative informational feedback to regulate the chemistry for these dynamic assemblies.

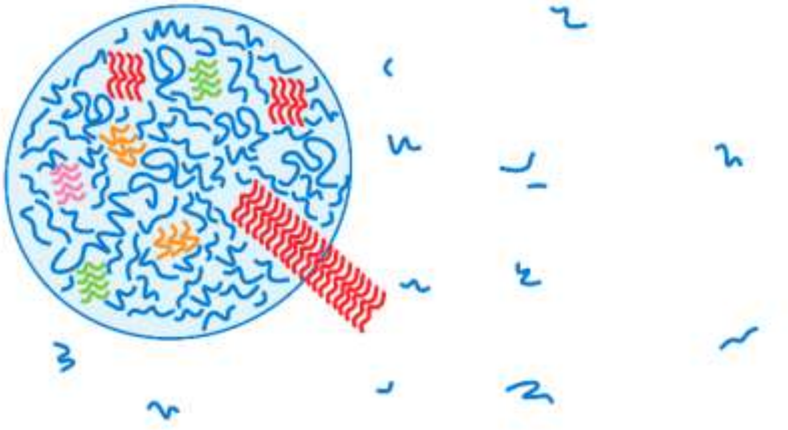

Figure 3.11 Proposed model for two-step amyloid nucleation. Peptide strands (blue) collapse into solute-rich particle phases. Within the particles, strands sample distinct β-sheets (orange, pink, green, blue lines). Liquid–solid phase transition occurs through sheet lamination in the particle, propagating the selected structure (red). Image is adapted from Gordon, C., et al.[1]

Chapter 3.3: Template-directed co-assembly

Like the conformational biasing that exists in the peptide LLPS shown in Figure 2,[14] the ability of IDPs to limit protein conformational sampling and cooperatively bind different specific templates is critical for their function.[17-19] The condensed peptide phases then serve as a good model for this mechanism, and the diversity of their potential ligands has been tested with surfaces that stabilize cross-β assembly along the three surfaces described above. Given the importance of C-terminal residues and counterions [20, 21] at the leaflet interface for nucleation as well as the role that nucleic acids in charge-complementary [2, 22] in nucleolus and ribonucleoprotein co-assembly, attempts to capture the cross-β assemblies of the peptide LLPS with RNA have been explored.[4, 23] As shown in Figure 3.3, Ac-KLVIIAG-NH2 (Pep-KG) and Ac-RLVIIAG-NH2 (Pep-RG) assemble naturally into cross-β fibers, but are templated onto ribbons with polyphosphate and RNA at 4 °C and nanotubes at 37 °C.[2] Again these templates nucleate co-assembly within the LLPS. Templating requires a strand of at least six nucleotides (phosphates) to form homogeneous nanotubes at 37 °C, establishing a critical role for cooperatively in templating co-assembly.

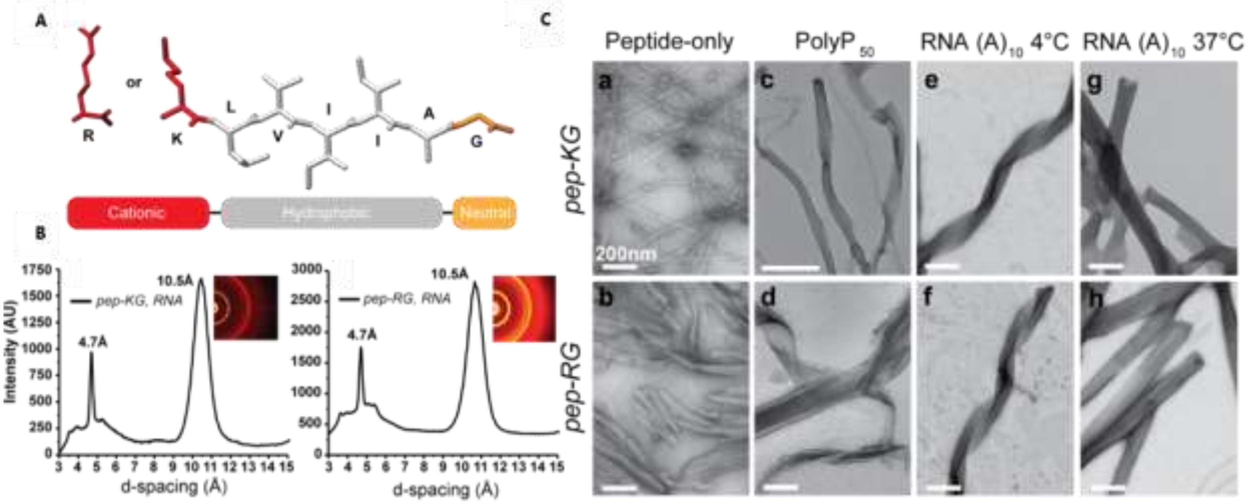

Figure 3.12 A, Molecular structure of pep-RG or pep-KG, with chemical properties as noted. B, Powder X-ray diffraction of co-assembled peptides and nucleic acids, indicating cross-ß architecture with the hallmark intersheet and interleaflet distances of 4.7 and 10 Å, respectively. Adapted from Reference 5, © 2020 The Authors. Published by Wiley-VCH Verlag GmbH & Co. KGaA.[2]

As shown in Figure 3.4, nucleic acids extend the bilayer to stabilize multilamellar assemblies by templating the leaflet interface to give a remarkable co-assembly. Given that peptides can template their own synthesis [13] and that the cross-β leaflet surfaces can be engineered to catalyze various condensation reactions,[3] the structure model in

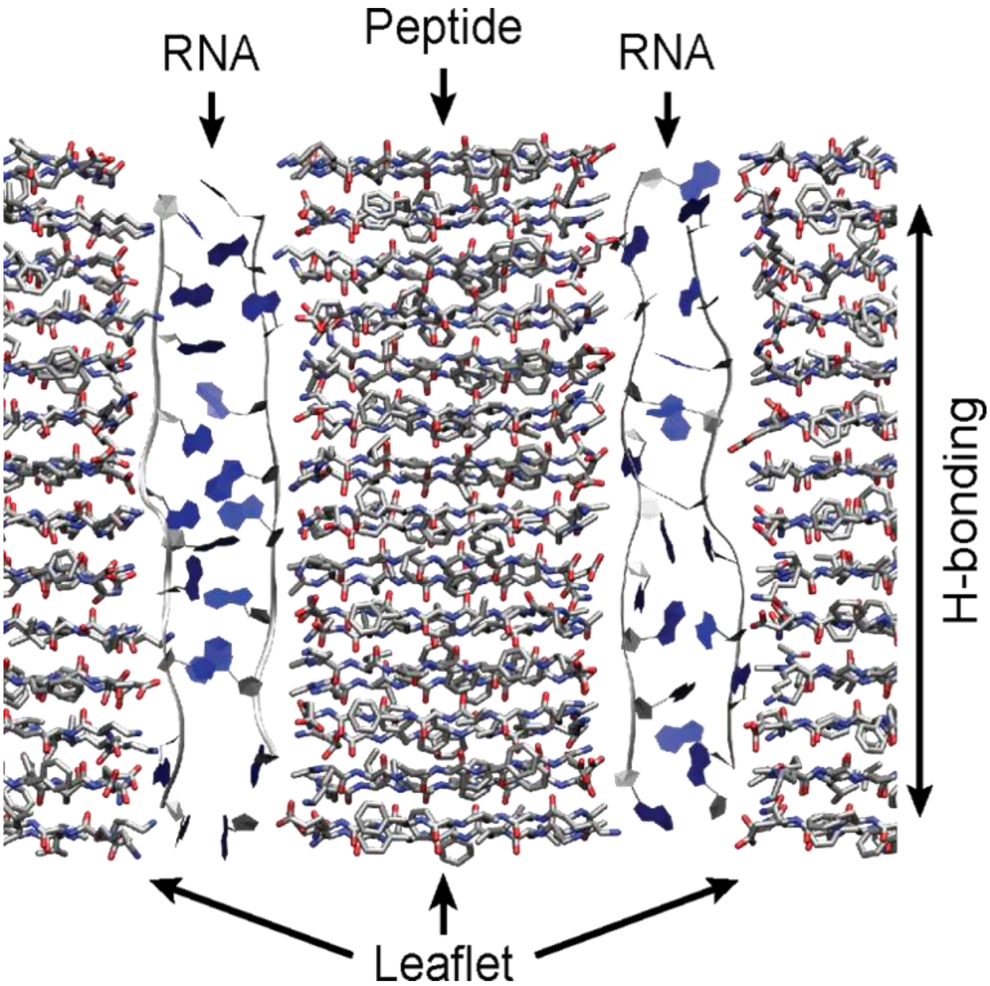

Figure 3.13 MD simulations of peptide/RNA interface. Viewed along β-sheet stacking direction with RNA arrayed along peptide H-bond direction, showing single RNA strands for clarity between peptide cross-β leaflets. RNA backbone is highlighted as gray ribbon and nucleobase as filled blue polygons.

Figure 4 suggests an opportunity for not only co-assembly, but also for cooperative production of polymeric materials as driven by phase transitions. The emerging codes for assembly, combining the structural and functional properties of polypeptide cross-β materials [20, 24] and helical assemblies [25, 26] will continue to enable the novel construction [27] of polymeric materials that extend and regulate molecular information for applications in health and disease.

Chapter 3.4: Generalization of electrostatic complementarity at the leaflet interface

Environmental factors like pH can be significant enough factors to globally alter peptide-rich paracrystalline assemblies, favoring antiparallel out-of-registry E22 assemblies in acidic pH and antiparallel in-registry E22 assemblies in neutral pH.[28] Further investigations to short, charged E22 congeners such as Ac-KLVFFAL-NH_2 (E22L) and Ac-pYLVFFAL-NH_2 illustrate the importance of the interleaflet space that exists at the β-sheet interface. Positively charged E22L can form bilayer nanotube morphology, where the interleaflet space between the layers is rich in positively charged residues. This space, then, could favorably incorporate trifluoroacetate ions, similar to the incorporation of nucleic acids by Pep-KG as illustrated in Figure 4. On the other hand, negatively charged Ac-pYLVFFAL-NH_2, which also forms bilayer nanotubes, can incorporate triethylamine ions in its interleaflet space that is rich with negatively charged phosphotyrosine residues.

This charge complementarity can be generalized with other similar short peptide models, like Ac-HLVIIAG-NH_2 as well. Ac-HLVIIAG-NH_2, inspired by Pep-KG, was initially designed for depolymerization of activated phosphate substrates, also displays charge complementarity with polyanionic templates. The peptide, when assembled in 25 mM MES buffer at pH 5.5, results in fibrillar morphology. Using the Henderson Hasselbach equation, we assume about half of all histidines in the assembly are protonated due to the side chain pK_a of ~6, allowing for enough positive charges attributed by protonated side chain for recruitment by the polyphosphate template as well as facilitating the hydrolysis of activated phosphate substrates by the neutral histidine, as illustrated in Scheme 3.1.

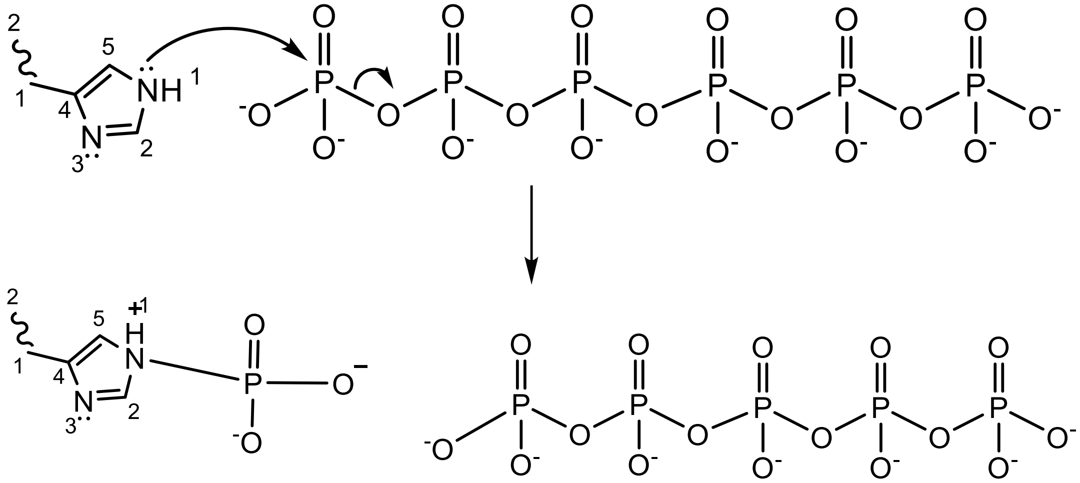

Scheme 3.1 Hydrolysis of polyphosphate by neutral histidine.

Synthesis of the polyphosphate substrate as described by literature [29] resulted in largely heterogeneous lengths of polymers as shown by ^{31}P NMR. Thus, we opted to co-assemble Ac-HLVIIAG-NH_2 with sodium trimetaphosphate (TMP), a 3-member cyclic inorganic phosphate, instead. The cyclic nature of this substrate should increase the probability for depolymerization due to ring strain. Additionally, Ac-HLVIIAG-NH_2 was also co-assembled with long strands adenines (PolyA25) as a morphological comparison. Given that DNA-templated Pep-KG resulted in multilamellar nanotube assembly, Ac-HLVIIAG-NH_2 should also result in multilamellae due to electrostatic interactions along the leaflet interfaces. As expected, PolyA25 templated Ac-HLVIIAG-NH_2 assembly did result in multilamellar architecture that is largely heterogeneous (Figure 3.5a), while peptides assembled with TMP yielded densely bundled, short fibers (Figure 3.5b). However, Ac-HLVIIAG-NH_2 assembled on its own resulted in long fibers with leaf-like structures that could be sheets which had not yet twisted to form fibers (Figure 3.5c).

As CD spectroscopy data suggest, the assembly pathway of Ac-HLVIIAG-NH_2 differed significantly in the presence of the two different templates. Given that CD spectroscopy relies on conformationally dependent electronic energy transitions, namely the nπ* (nonbonding to antibonding) and ππ* (bonding to antibonding) transitions, structural predictions of polypeptides and proteins can be made. Typically, spectra of β-pleated sheets will exhibit positive ellipticity at 208 nm and intense negative ellipticity at 218 nm. Previous literature has dissected distinct β characters and their associated electronic transitions which can be observed with CD spectroscopy, making identification of β-pleated sheets, β-turns, and a mixture of the two possible.[30] CD spectra in Figure 6a suggest that, while Ac-HLVIIAG-NH_2 exhibits strong β character with and without templates, the presence of PolyA25 template may induce a distinct, more twisted β architecture as noted by the large $\lambda_{208\ nm}/\lambda_{218\ nm}$ ratio, while Ac-HLVIIAG-NH_2 assembled

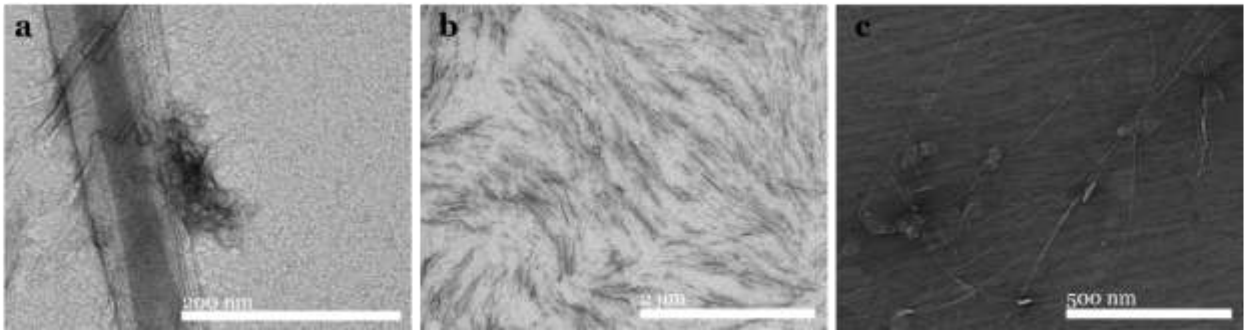

Figure 3.14 TEM micrographs of Ac-HLVIIAG-NH_2 assembly in the presence of PolyA25 template (a), TMP template (b), and no template (c). Micrographs were prepared within 24 hours of assembly. Scale bars are as indicated in each panel.

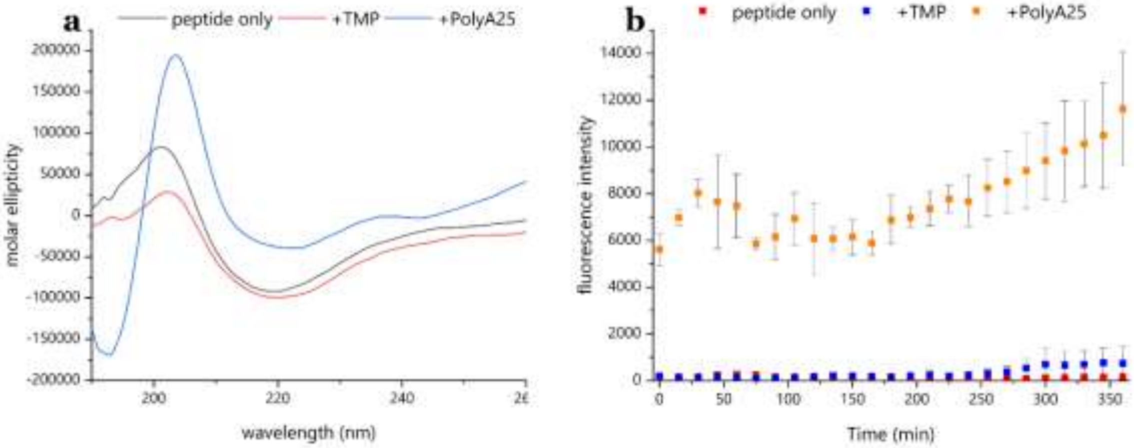

Figure 3.15 Structural probing of Ac-HLVIIAG-NH_2 at early timepoints. CD spectroscopy (a) revealed distinct β character for each assembly. Ac-HLVIIAG-NH_2 assembled with PolyA25 template (blue) exhibit strong β-turn character, with a high $\lambda_{206}/\lambda_{218}$ ratio, while both peptide alone and peptide assembled with TMP template exhibit the typical β-pleated sheet character with the $\lambda_{206}/\lambda_{218}$ ratio being closer to 1. ThT fluorescence assays (b) showed significant increase in ThT fluorescence immediately in Ac-HLVIIAG-NH_2 assemblies with PolyA25 template, but not with TMP template or Ac-HLVIIAG-NH_2 assembled alone.

alone or with TMP template displays the more typical β-pleated sheet conformation, with equal nπ* and ππ* contributions. The rate of formation of these cross-β structures were compared between the three assemblies across the first 6 hours of assembly by monitoring thioflavin T fluorescence intensities. Thioflavin T (ThT) is a small molecule known to fluoresce upon binding with ordered β-sheets, a hallmark of amyloids. When free, ThT has a freely rotating phenyl ring, but when ThT is bound between the ordered β-sheets within a cross-β configuration, the rotation is restricted, forcing the small molecule to release the energy through fluorescence. Thus, the fluorescence intensity of

ThT is directly correlated to the presence of ordered β-sheets. ThT fluorescence data demonstrated a markedly accelerated growth in cross-β assembly in PolyA25 templated Ac-HLVIIAG-NH_2 within the first 360 minutes of assembly, while TMP templated Ac-HLVIIAG-NH_2 closely tracked the growth pattern of Ac-HLVIIAG-NH_2 assembly (Figure 3.6). Taken together, both sets of data suggest that long strands of DNA could better template Ac-HLVIIAG-NH_2 than could TMP.

Conclusion

Paracrystalline assemblies arising from peptides can be stabilized by cross-β architecture, which holds especially true for Aβ42 and its congeners.[31-33] The energetic contributions due to hydrophobic residues' facial complementarity, charged residues' electrostatics, and hydrogen-bonding along the peptide backbone aid in this structural stabilization. These factors, however, can be sensitive to even the most subtle substitutions, as the difference between a leucine and a valine residue – a single methyl group, was enough to change the global morphology from a nanotube with 30 nm diameter to a nanotube with 300 nm diameter, respectively.

Furthermore, associations between two different biopolymers, polypeptides and oligonucleotides, are largely guided by electrostatic complementarity as demonstrated by Pep-KG and nucleic acids can be generalized. Ac-HLVIIAG-NH_2, despite its predictably less positive charge contribution, still exhibits charge passivated template-directed assembly with PolyA25, albeit in a more heterogeneous manner. This heterogeneity could be attributed to the split distribution of protonated, positively charged and charge-neutral histidine residues, the first of which is the most likely candidate for interacting with negatively charged species like PolyA25 and TMP. Understanding this nuance could then better inform the development of reactive bio-inspired materials.

Materials and methods

Synthesis of Ac-HLVIIAG-NH₂

Ac-HLVIIAG-NH_2 was synthesized on Rink amide-MBHA (Anaspec) solid support via a CEM Liberty Blue Automated Microwave Peptide Synthesizer (Serial # LB2447) with 1M N,N′-Diisopropyl carbodiimide (DIC; CAS# 693-13-6 AAPPTEC) as the activator, Oxyma Pure (CAS# 3849-21-6 CEM) as the activator base, and 20% Piperidine (CAS# 110-89-4 Sigma-Aldrich) as the deprotection solution. Amino acids were coupled using 0.25 mmol standard coupling (75°C 210W for 15s followed by 90°C 30W for 110s) and deprotected using 0.25 mmol standard deprotection (75°C 175W 15s, 90°C 30W 50s). The amino acids used were as follows: fmoc-trt-histidine, fmoc-leucine, fmoc-valine, fmoc-isoleucine, fmoc-alanine, fmoc-glycine, and fmoc-glutamic acid, and each one dissolved in dimethylformamide (DMF; CAS# 68-12-2 Sigma-Aldrich). The N-terminus was acetylated with a 20% acetic anhydride (CAS# 108-24-7 Sigma-Aldrich) in DMF solution and the 0.25 mmol N-terminal acetylation method (60°C 50W 30s, 25°C 0W 30s, 60°C 50W 30s, 25°C 0W 30s). Upon completion of synthesis, the resin beads were rinsed with dichloromethane (DCM) then let dry via vacuum filtration for cleavage from solid support which was carried out using a cocktail of 9:0.5:0.3:0.2 ratios of trifluoroacetic acid (TFA CAS# 76-05-1 Chem Impex)/thioanisole (CAS# 100-68-5 Sigma-Aldrich)/1,2-ethanedithiol (CAS# 540-63-6 Sigma-Aldrich)/anisole (CAS# 100-66-3 Sigma-Aldrich), where 10 mL of the cocktail was used in each of two vials and the 0.25 mmol of peptide attached to resin was evenly distributed across the two vials. The resin beads were submerged in the cocktail and were continuously perturbed using an orbital shaker at low intensity for to allow for homogeneous coverage of the beads with the cleaving reagents, and the reaction vessels were left for 3 hours at room temperature. Upon completion, the beads are filtered from the peptides via gravity filtration immediately into cold (-20°C) ether (CAS# 60-29-7 Fischer Scientific). At this point, the ether should become warm and cloudy due to mass precipitation of the peptides, and the mixture is then spun down at 4000 RCF for 15 minutes at 4°C to improve precipitation. The ether supernatant was discarded, and the gel-like pellet was washed with more cold ether for centrifugation, a process that is repeated twice more. The pellet was stored in vacuo pending RP-HPLC purification, which involved the use of a semi-preparative C18 column and an acetonitrile and water gradient, using 0.1% trifluoroacetic acid as a counterion.

Preparation of Ac-HLVIIAG-NH_2 assemblies

After HPLC purification and subsequent lyophilization, Ac-HLVIIAG-NH_2 was ready to be weighed and dissolved in 40% acetonitrile in water to achieve a final peptide concentration of 2 mM and probe sonicated for 30 seconds to prevent premature assembly. Stock solutions of PolyA25 were made by dissolving PolyA25 in water to achieve a final DNA concentration of 80 µM. Stock solutions of TMP were made fresh each time within 24 hours of each assembly by dissolving commercially available TMP (CAS #: 7785-84-4, Sigma Aldrich) in 40% acetonitrile in water to achieve a final concentration of 0.66 mM. Ac-HLVIIAG-NH_2 assembly without templates were done by adding equal volumes of 2 mM peptide solution and 40% acetonitrile in water. Templated Ac-HLVIIAG-NH_2 assemblies were made by adding equal volumes of 2 mM peptide solution and either 80 µM PolyA25 solution or 0.66 mM TMP solution to achieve a charge ratio of 1 : 1 with respect to peptide : template. All assemblies were incubated at 37°C and kept for up to 2 months.

Peptide secondary structure analysis via CD spectroscopy

Circular Dichroism (CD) analyses were recorded on a Jasco-810 Spectropolarimeter. Samples were micro-pipetted onto a 50µL Hellma Analytics quartz cell with a 0.1 mm path length (Model # 106-0.10-40). Spectra were measured by averaging 3 scans from 260-190 nm with a 0.2 nm data pitch and 100 nms-1 scanning speed. Molar ellipticity was calculated with the equation $[\theta] = \theta/(10 \times c \times l)$ where c is the peptide concentration in moles/L and l is the pathlength of the cuvette in cm.

Thioflavin T kinetics assay

Samples for Thioflavin T fluorescence analyses were prepared by combining 74 µL of each sample, 100 µL of 40% acetonitrile, and 1 µL of 10 mM Thioflavin T (CAS# 2390-54-7 purchased from Sigma-Aldrich) and measured in the wells of a 96 well plate (Microplate, 96 well, PS, F-bottom, µCLEAR, black, med. binding, Greiner Bio-one). Thioflavin T fluorescence was determined with a BioTek Synergy Mx plate reader (Serial# 250843) every 15 minutes for up to 24 hours, with short shaking before each read. The excitation wavelength was 444 nm and fluorescence were measured at 484 nm. A well containing 1 µL 10 mM ThT in 40% MeCN and 174 µL 40% MeCN was used as a baseline. The plate was held at 37°C for all 24 hours.

References

1. Gordon, C.K., R. Luu, and D. Lynn, *Capturing nested information from disordered peptide phases*. Peptide Science, 2021. **113**(2): p. e24215.
2. Rha, A.K., et al., *Electrostatic Complementarity Drives Amyloid/Nucleic Acid Co-Assembly*. Angew Chem Int Ed Engl, 2020. **59**(1): p. 358-363.
3. Omosun, T.O., et al., *Catalytic diversity in self-propagating peptide assemblies*. Nature Chemistry, 2017. **9**(8): p. 805-809.
4. Anthony, N.R., et al., *Mapping amyloid-beta(16-22) nucleation pathways using fluorescence lifetime imaging microscopy*. Soft Matter, 2014. **10**(23): p. 4162-72.
5. Lynn, D.G., et al., *Conformational evolution: the wiggling of peptides into amyloid*. Structure, 2003. **11**(3): p. 242.
6. Liang, Y., et al., *Cross-strand pairing and amyloid assembly*. Biochemistry, 2008. **47**(38): p. 10018-26.
7. Liu, P., et al., *Nucleobase-directed amyloid nanotube assembly*. J Am Chem Soc, 2008. **130**(50): p. 16867-9.
8. Lu, K., et al., *Macroscale assembly of peptide nanotubes*. Chem Commun (Camb), 2007(26): p. 2729-31.
9. Mehta, A.K., et al., *Facial symmetry in protein self-assembly*. J Am Chem Soc, 2008. **130**(30): p. 9829-35.
10. Guo, Q., et al., *Shape selection and multi-stability in helical ribbons*. Applied Physics Letters, 2014. **104**(21): p. 211901.
11. Lakdawala, A.S., et al., *Dynamics and fluidity of amyloid fibrils: a model of fibrous protein aggregates*. J Am Chem Soc, 2002. **124**(51): p. 15150-1.

12. Liang, Y., D.G. Lynn, and K.M. Berland, *Direct Observation of Nucleation and Growth in Amyloid Self-Assembly*. Journal of the American Chemical Society, 2010. **132**(18): p. 6306-6308.
13. Chen, C., et al., *Design of multi-phase dynamic chemical networks*. Nature Chemistry, 2017. **9**(8): p. 799-804.
14. Rengifo, R.F., et al., *Liquid-Like Phases Preorder Peptides for Supramolecular Assembly*. ChemSystemsChem, 2020. **2**(6): p. e2000007.
15. Hsieh, M.C., D.G. Lynn, and M.A. Grover, *Kinetic Model for Two-Step Nucleation of Peptide Assembly*. J Phys Chem B, 2017. **121**(31): p. 7401-7411.
16. Liang, C., et al., *Kinetic Intermediates in Amyloid Assembly*. Journal of the American Chemical Society, 2014. **136**(43): p. 15146-15149.
17. Chi, S.W., et al., *Structural details on mdm2-p53 interaction*. J Biol Chem, 2005. **280**(46): p. 38795-802.
18. Kim, D.H. and K.H. Han, *PreSMo Target-Binding Signatures in Intrinsically Disordered Proteins*. Mol Cells, 2018. **41**(10): p. 889-899.
19. Kim, D.H., et al., *The Mechanism of p53 Rescue by SUSP4*. Angew Chem Int Ed Engl, 2017. **56**(5): p. 1278-1282.
20. Dong, J., et al., *Engineering metal ion coordination to regulate amyloid fibril assembly and toxicity*. Proceedings of the National Academy of Sciences, 2007. **104**(33): p. 13313-13318.
21. Hane, F. and Z. Leonenko, *Effect of Metals on Kinetic Pathways of Amyloid-β Aggregation*. Biomolecules, 2014. **4**(1): p. 101-116.

22. Boeynaems, S., et al., *Spontaneous driving forces give rise to protein-RNA condensates with coexisting phases and complex material properties*. Proc Natl Acad Sci U S A, 2019. **116**(16): p. 7889-7898.

23. Chotera, A., et al., *Functional Assemblies Emerging in Complex Mixtures of Peptides and Nucleic Acid-Peptide Chimeras*. Chemistry, 2018. **24**(40): p. 10128-10135.

24. Ni, R., et al., *Remodeling Cross-β Nanotube Surfaces with Peptide/Lipid Chimeras*. Angewandte Chemie International Edition, 2012. **51**(27): p. 6635-6638.

25. Hughes, S.A., et al., *Ambidextrous helical nanotubes from self-assembly of designed helical hairpin motifs*. Proceedings of the National Academy of Sciences of the United States of America, 2019. **116**(29): p. 14456-14464.

26. Merg, A.D., et al., *Seeded Heteroepitaxial Growth of Crystallizable Collagen Triple Helices: Engineering Multifunctional Two-Dimensional Core-Shell Nanostructures*. Journal of the American Chemical Society, 2019. **141**(51): p. 20107-20117.

27. Forman-Kay, J.D., R.W. Kriwacki, and G. Seydoux, *Phase Separation in Biology and Disease*. J Mol Biol, 2018. **430**(23): p. 4603-4606.

28. Hsieh, M.C., et al., *Multistep Conformation Selection in Amyloid Assembly*. J Am Chem Soc, 2017. **139**(47): p. 17007-17010.

29. Wazer, J.R.V., *Structure and Properties of the Condensed Phosphates. III. Solubility Fractionation and Other Solubility Studies*. Journal of the American Chemical Society, 1950. **72**(2): p. 647-655.

30. Brahms, S., et al., *Identification of beta,beta-turns and unordered conformations in polypeptide chains by vacuum ultraviolet circular dichroism*. Proc Natl Acad Sci U S A, 1977. **74**(8): p. 3208-12.

31. Johnstone, E.M., et al., *Conservation of the sequence of the Alzheimer's disease amyloid peptide in dog, polar bear and five other mammals by cross-species polymerase chain reaction analysis*. Brain Res Mol Brain Res, 1991. **10**(4): p. 299-305.

32. Balbach, J.J., et al., *Amyloid fibril formation by A beta 16-22, a seven-residue fragment of the Alzheimer's beta-amyloid peptide, and structural characterization by solid state NMR*. Biochemistry, 2000. **39**(45): p. 13748-59.

33. Petkova, A.T., et al., *Self-Propagating, Molecular-Level Polymorphism in Alzheimer's ß-Amyloid Fibrils*. Science, 2005. **307**(5707): p. 262-265.

Chapter 4: Polyanion order controls liquid-to-solid phase transition in peptide/nucleic acid co-assembly

Original publication source: Gordon-Kim, C.[1], Rha, A.[1], Poppitz, G., et al. Polyanion order controls liquid-to-solid phase transition in peptide/nucleic acid co-assembly. *Front. Mol. Biosci.*, 14 November 2022

Chapter 4.1: Oligonucleotide diversity in biomolecular condensates

A gross majority of bulk cellular RNA is comprised of rRNA and mRNA, where each transcript type is processed differently.[1-3] 10% of mRNA transcripts have been found sequestered within stress granules and other protein-rich coacervates. [4] The functions of these cellular membraneless organelles range from storage granules to processing hubs chaperoning mRNA through the critical stages of cellular stress, division, and differentiation.[5-8] The multifaceted functions that RNP granules play depends on dynamic structural plasticity of these co-assemblies.[9-15] For example, the cooperative interactions between arginine residues of the RNA binding domain and the tyrosine residues from the prion-like domains (PLD) of FUS are critical for the dual effects of ATP concentrations that both induces and inhibits initial phase transitions at different concentrations by controlling these interactions.[16, 17]

The nucleating core of the Alzheimer's disease-associated Aβ42 peptide, the sequence KLVFFAE, has been extensively studied as a separate peptide and shown to have strong cross-β propensity: independently undergoing 2-step nucleation that includes condensation and subsequent self-assembly into cross-β fibers, which can allow for the inclusion of other polymers between the leaflets (Figure 4.1). There is now evidence that these peptide condensates are preordered within the condensates for nucleation, highlighting the remarkable potential environmental control over the final assembled morphology.[10, 13, 18-26] Indeed, subtle changes in amino acid sequence greatly impact the rates of nucleation and propagation along the three potential cross-β assembly growth planes. The Aβ motif congener Ac-KLVIIAG-NH2 (Pep-KG) is derived from KLVFFAE, with the phenylalanine dyad replaced by isoleucine and the terminal glutamate replaced by glycine. Pep-KG was designed to have a lower propensity for nucleation relative to KLVFFAE by replacing the phenylalanine with isoleucine residues and only retaining a single cationic residue for charge-driven phase separation templated by polyanions. These changes allowed for nucleic acid passivation of the leaflet interface by nucleic acids with the subsequent assembly of distinct antiparallel β-sheets organized as multilamellar

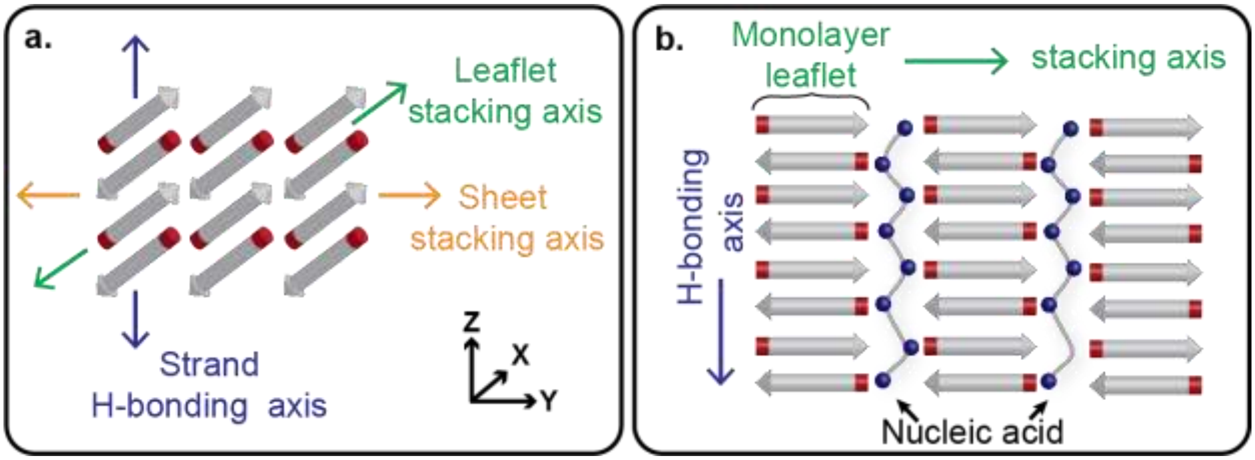

Figure 4.16 Cross-β architecture allows for packing of other polymers in between the leaflets. Hydrogen bonding across amides from consecutive peptide strands contribute to leaflet formation in the z-axis, while side chain interactions contribute to the stacking of β-Sheets along the y-axis (**A**). The leaflets, where the peptide termini are positioned, have been shown to accommodate polyanionic species like polyphosphates and oligonucleotides (**B**).

cross-β nanotubes.[27] RNA, DNA, and polyphosphate (p50) all nucleate assembly, consistent with electrostatics playing significant roles in these 2-step transitions much like ATP with FUS.[28] While the final peptide cross-β assembly with phosphate pacification are well ordered, the nucleic acid backbone is ordered electrostatically in respect to the peptide assembly, with consistent distances between Pep-KG lysines and nucleic acid phosphates as shown by previous solid state NMR data.[27]

Given the role of ATP as a trivalent binder regulating FUS assembly and the range of cellular processes that depend on RNA structural dynamics within RNP granules, we have now explored this single motif as a reporter for the role that nucleic acid conformations may play in the 2-step nucleation process.[29-33] Nucleic acid conformations dictate the ordering of phosphate charges along the backbone and significantly impacts the initial nucleation of supramolecular co-assembly. This ordered nucleation sets the stage for the propagation of unique paracrystalline order. Using this insight, we have designed nucleic acid-peptide chimeras to create novel architectures that exploit both the plasticity of the peptide motifs as well as the nucleic acid templates. These results provide a foundation for strategies focused on the construction of nucleic-acid-based functional materials with cross-β assembles and could further inform the diverse and dynamic controls underlying ribonucleoprotein granule function. This knowledge will prove useful in the rapidly evolving field of biomaterials, drawing parallels between exploiting the energetics of coacervate materials and bottom-up approaches for materials design.

Chapter 4.2: Double-stranded DNA more effectively templates cross-β peptide assembly

It has been demonstrated that charged monomer sequence patterns can influence complex coacervate formation in synthetic polymers, but how nucleic acid polymer conformations impact peptide coacervation remains unknown. To investigate the role higher-order nucleic acid structure plays in nucleating 2-step peptide assembly, the single stranded dodecamer (5'-CGCGAATTCGCG-3', ssDNA) and its Drew-Dickerson B-DNA duplex (dsDNA) were each incubated with the single sticker/spacer motif, Pep-KG (Ac-KLVIIAG-NH2).[34-38] The structures formed by this DNA sequence has been extensively studied for decades and is short enough to limit conformational sampling throughout the studies. Furthermore, previous studies have demonstrated that the nanotube morphology are independent of oligonucleotide sequence and length, provided that there are at least 6 consecutive nucleotides.[27] As shown in Figure 4.2a top panel, Pep-KG alone undergoes 2-step nucleation, transitioning through initial condensates to fibrous assemblies within a day of dissolution and remains as such (Figure 4.2d) indefinitely, as previously reported.[27] In comparison, when Pep-KG is assembled in the presence of DNA templates at a 1:1 charge ratio, the rate of assembly is dramatically accelerated as reported by thioflavin T (ThT) fluorescence (Figure 4.2g). While both dsDNA and ssDNA templates dramatically impact Pep-KG assembly, dsDNA rapidly templates helical ribbons while ssDNA shows much greater heterogeneity at early time points (Figure 4.2 b,c). However, with longer incubation times, both ssDNA and dsDNA template the assembly of similar multilamellar ribbon morphology that ultimately transitions into nanotubes (Figure 4.2 e,f).

To evaluate whether the initial coacervation step might be impacted by the charge ordering of the template, the fluorescent probe 2-aminopurine (2AP) (Ex. 310 nm/Em. 370 nm) was synthetically incorporated into the center of the dodecamer sequence, 5’-CGCG(2AP)ATTCGCG-3’. As shown in Fig. 2h, the fluorescence is immediately quenched in all the peptide co-assemblies to a level similar to that of the dsDNA, significantly less than the ssDNA alone. These data establish that ssDNA does not self-assemble under

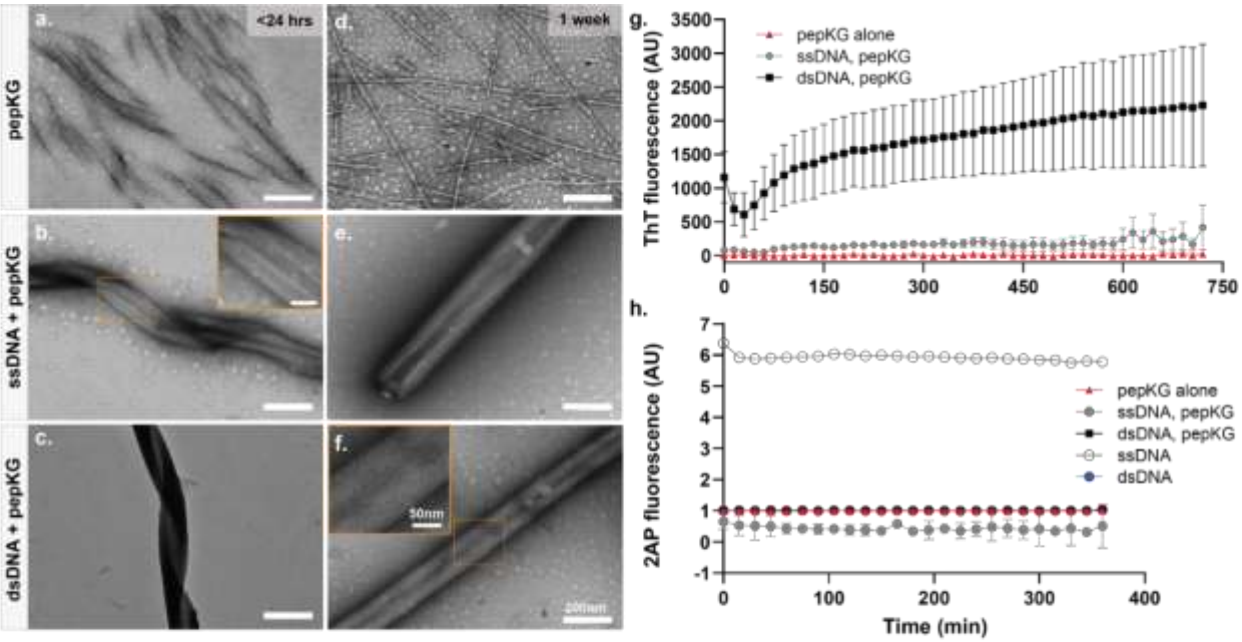

Figure 4.17 Pep-KG assembly rate is accelerated when templated with dsDNA. TEM image panels (**A–C**): Pep-KG assembled alone, Pep-KG assembled with ssDNA, and Pep-KG assembled with dsDNA, respectively, within 1 day of initial dissolution. Panels (**D–F**) were taken after 1 week of incubation. All peptides and DNA templates were dissolved in 40% MeCN at 1 mM Pep-KG concentration and continuously incubated at 37°C. Measurements of ThT fluorescence (**G**) indicates cross-β growth of the assembly within the first 12 h and (**H**) 2AP fluorescence within the first 6 h of assembly. Each fluorescence measurement was done at 37°C incubation across all timepoints. All error bars are 95% CI values and all samples for 2AP and ThT fluorescence are n = 3.

these conditions, and rapidly condenses with the oppositely charged peptide. This immediate 2AP quenching in ssDNA is consistent with long, synthetic, same-charge monomers in polymers exhibiting strong charge interactions in complex coacervate condensation.[39]

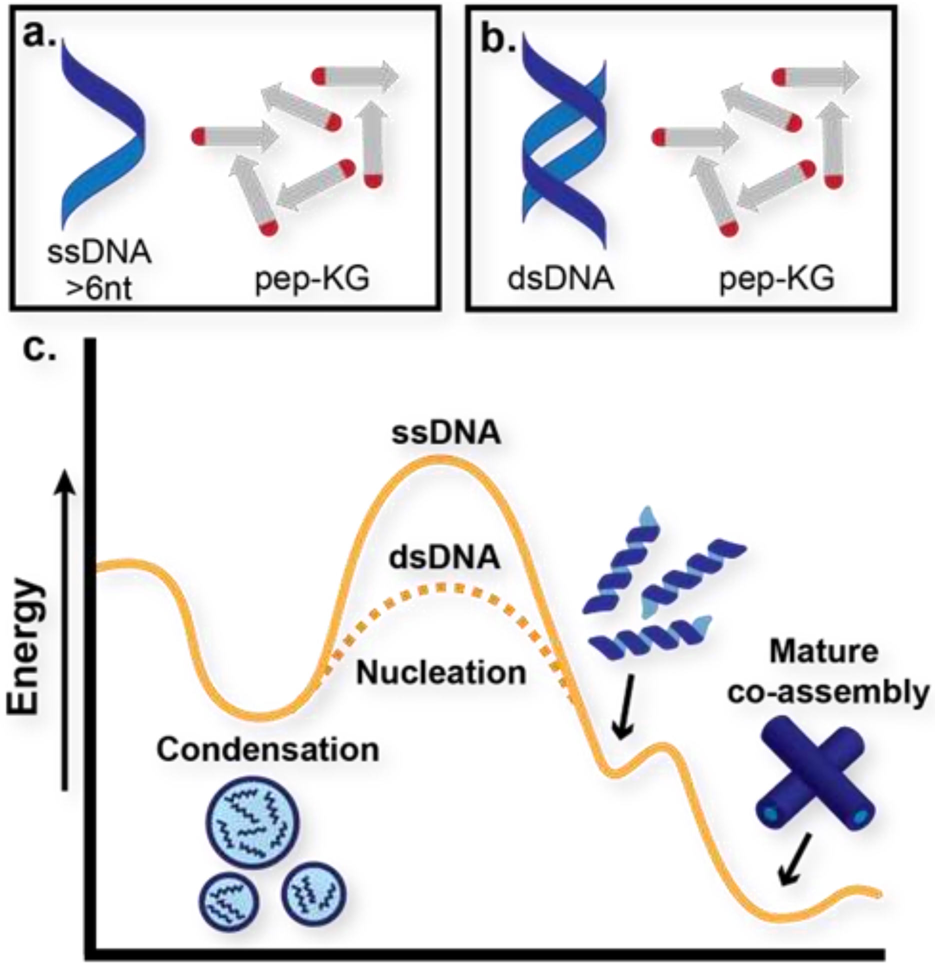

Figure 4.18 Proposed energy diagram of distinct pathways that Pep-KG may undergo through context-dependent co-assemblies. (**A**) and (**B**) denote Pep-KG assembly templated by ssDNA and dsDNA, respectively. Proposed energy diagram (**C**) illustrates dsDNA templates lower the energetics of nanotube assembly relative to ssDNA templates, as demonstrated by ThT fluorescence experiments.

The dsDNA template rapidly nucleates and propagates paracrystalline peptide assembly (Figure 4.2 g), but the initial ThT fluorescence drops during the first hour, and then grows cooperatively. This initial drop could be the result of breathing modes and fraying at the ends of the template as it enters the peptide condensate.[40, 41] The apparent autocatalytic growth has been previously seen with rearrangements that alter ThT binding as the growing assembly moves beyond the initial biomolecular condensate.[18, 42] The ssDNA also templates peptide ordering, but only beginning after 6 hours of incubation as monitored by ThT fluorescence (Figure 4.2 g). Taken together, these results indicate that although both single-stranded and double-stranded DNA function as polyanionic templates capable of nucleating peptide assembly, double-stranded DNA accelerates the formation of paracrystalline assemblies. Given what we know about the assembly pathway of Pep-KG, we believe this to be because dsDNA is more effectively recruiting Pep-KG monomers within the particle phase and more rapidly forming a stable nucleus which then propagates out of the particle into ribbons and finally nanotubes (Figure 4.3).

Chapter 4.3: Electrostatic ordering underlies template effectiveness

The dsDNA template contains twice the number of phosphates as the ssDNA template, and this difference may contribute to the difference in nucleation efficiency. However, the number of charges is not the only difference when comparing dsDNA to ssDNA, as the duplexed DNA also exhibits a significant surface area increase, which impacts the spatial ordering of the charges. Thus, to determine whether the number of phosphates or their order contributes most significantly to nucleation efficiency, we compared dA3, the 5’-phosphorylated linear adenine ssDNA, and trimetaphosphate

(TMP), a constrained cyclic 6-membered phosphate ring with the same number of charges as dA3 (Figure 4.4a). Consistent with the previously reported results, incubation of dA3 with Pep-KG gave heterogeneous fibrillar morphologies (Figure 4.4b), while TMP

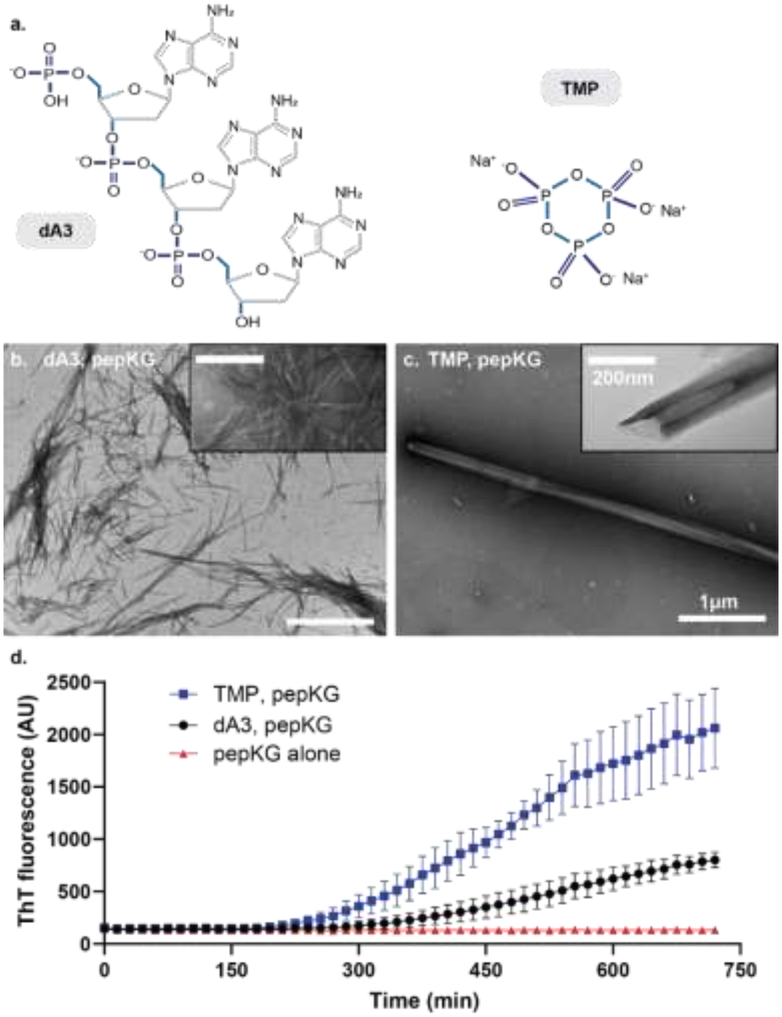

Figure 4.19 TMP and PolydA$_3$ nucleate Pep-KG assembly differently**.** (**A**) Structures of A3 (left) and TMP (right). Micrographs of Pep-KG assembled in the presence of A3 (**B**) and in the presence of TMP (**C**). Both images were taken within 1 day of dissolution in 40% MeCN at 37°C. Both samples consisted of 1 mM Pep-KG and 333 µM dsDNA and 333 µM TMP. (D) ThT fluorescence of Pep-KG/dA3 and Pep-KG/TMP samples within the first 12 h. Error bars represent 95% CI values, and all samples are n = 3.

rapidly nucleates Pep-KG into the nanotube morphology seen with dsDNA and ssDNA templates (Fig 4.4c).[27]

These co-assemblies were also monitored for 12 hours following dissolution via ThT fluorescence (Figure 4d). Here, the TMP-templated sample assembled more rapidly than dA3-templated and non-templated assemblies. Considering the distinct ordering of the charged phosphates in TMP, these data suggest that in addition to charged monomers, conformational charge ordering, in TMP covalently constrained, is most critical for nucleating paracrystalline ordering. Whereas dsDNA accelerates the formation of nanotubes relative to ssDNA but the DNA and Pep-KG assembly pathway is overall the same (Figure 4.3), the TMP and Pep-KG assembly pathway is totally distinct from the assemblies formed with dA3 (Figures 4.4b, c).

Chapter 4.4: Propagation of cross-β co-assemblies is sensitive to electrostatic interference

Given the electrostatic ordering achieved by dsDNA during templated peptide cross-β nucleation, we sought to compare ss/dsDNA as templates for propagation. Propagation rates have been obtained via imaging approaches, but because of the complexity these electrostatic-driven processes, we investigated propagation control with passivating salts. $MgCl_2$ inhibits both nucleation and propagation in these co-assemblies, and here LiCl was selected because of Li^+'s small size, single charge, and minimal impact on more complex DNA structures.[43] Propagation was assessed via ThT kinetics at low and high concentrations of LiCl. The influence of LiCl concentrations on the relative growth rates showed little difference at high LiCl concentrations (Figure 4.5). This observation is most consistent with ssDNA and dsDNA being equally effective in co-assembly propagation in stark contrast to their effect on nucleation. Additional imaging approaches will be necessary to define these rates more precisely.

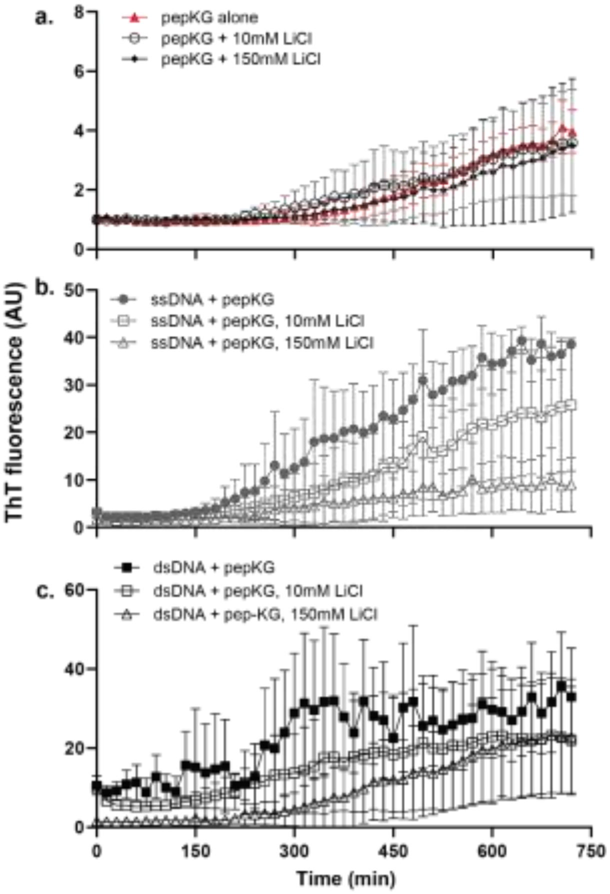

Figure 4.5. Pep-KG association with DNA can be modulated by LiCl. Cross-β assembly of Pep-KG, Pep-KG/ssDNA, and Pep-KG/dsDNA (**a**, **b**, **c**, respectively) monitored by ThT fluorescence in the presence of different LiCl concentrations, 10mM and 150 mM. All assemblies were incubated in 40% MeCN at 37°C with dsDNA and ssDNA added at a 1:1 charge ratio, 41.6 µM dsDNA and 83.3 µM ssDNA, with 5µM ThT that was added at the beginning of the assembly. It should be noted that, while ThT has been the standard probe for identifying the presence of cross-β assembly, it is unclear whether it plays a role in stabilization of the architecture. Thus, all assembly rates discussed here are relative to the baseline Pep-KG incubated with ThT. Error bars are 95% CI values and all samples are n=3..

Chapter 4.5: Seeding with quadruplex DNA/peptide chimeras

Given the effect of ordered charged templates on nanotube nucleation and the accommodation of ordered phosphate-containing molecules within propagating cross-β peptide assemblies, we sought to exploit these findings to construct functional sites along the peptide nanotube. Guanine quadruplexes (GQ) contain planes of four Hoogsteen base-paired guanine bases with phosphates defining the connecting edges. The bimolecular parallel quadruplex-forming DNA, GGTG4TGG, which requires two GQ DNA strands for assembly, organizes to form four stacked guanine quartets with well-ordered charges running along the corners of the GQ planes and potential for extended GQ stacking (Figure 4.6 a,b). [44-46] As shown in Figure 4.6 c, this DNA sequence assembles to give the characteristic CD signature of a parallel GQ.[45, 47, 48]

To enhance templating by this GQ template, GGTG4TGG was conjugated to the N-terminal residue side chain of the accompanying peptide via a Cu(I)-catalyzed click reaction. Initial peptide synthesis required replacement of the N-terminal lysine of Pep-KG with N-acetylated glutamic acid to give Ac-ELVIIAG-NH2. Further alkyne modification of the glutamic acid side chain was achieved following esterification using N-Hydroxysuccinimide (NHS) and amidation with propargylamine to give Ac-EmLVIIAG-NH2 (Scheme 1). Preparation of the GQ DNA included the addition of a 5' azide-modified T4 linker, N3-TTTTGGTG4TGG. These alterations provided flexibility for chimera-associated quadruplex formation (T4 linker) and enabled peptide-DNA click-conjugation via triazole linkage (Scheme 4.1).[44, 45, 49, 50] The click reaction gave rise to the guanine quadruplex peptide conjugate (GQPC), with linkage between the modified glutamic acid sidechain and the 5'-end of the GQ DNA.

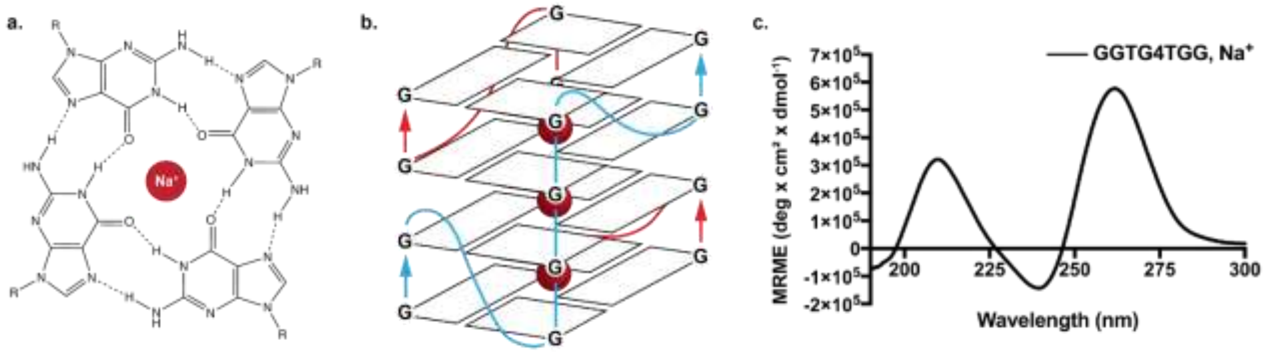

Figure 4.6. Ions like Na+ are conducive to guanine quadruplex formation. Metal cations, including K+ and Na+, facilitate guanine quartet formation through coordination with O6 atoms that project into the internal cavity (**a**). Metal cations are arranged equidistant from guanine quartets in the quadruplex, aligning the eight oxygen atoms in a symmetric tetragonal bipyramidal configuration. The sequence GGTG4TGG used in this study requires two DNA strands to associate for proper quadruplex folding and gives the depicted parallel guanine quadruplex (**b**). CD of GGTG4TGG in the presence of Na+ gives the expected parallel quadruplex signature with a maximum positive ellipticity at 260 nm (**c**).

To improve the propensity for supramolecular assembly and direct quadruplex formation, peptide concentrations and temperature were optimized. We found that below 0.4mM, Pep-KG nucleates slowly and when combined with GQPC, produced few visible assemblies by electron microscopy. At concentrations above 0.4mM, pep-KG and GQPC gave heterogenous co-assemblies. Therefore, 0.4mM Pep-KG was used during the co-assembly process (Figure 4.7 a). Due to the small reaction sizes, a maximum concentration of 10μM GQPC was achieved and combined completely with 0.4mM pep-KG. Pep-KG and GQPC were combined in sodium phosphate buffer (pH 7.4), heated to 95°C for five minutes to melt any existing nuclei, and returned to room temperature by decreasing the sample temperature at a rate of 2°C/minute to promote quadruplex formation. GQPC/pep-KG co-assemblies, in which the charge ratio was not 1:1 but rather the overall concentration ratio was 40:1, resulted in conical nanostructures by TEM (Figure 4.7 B, C). Similar to dsDNA and ssDNA-directed assembly, GQPC-templated assembly initially formed ribbons with the narrow end of the conical nanotubes closing first (Figure 4.7 C).

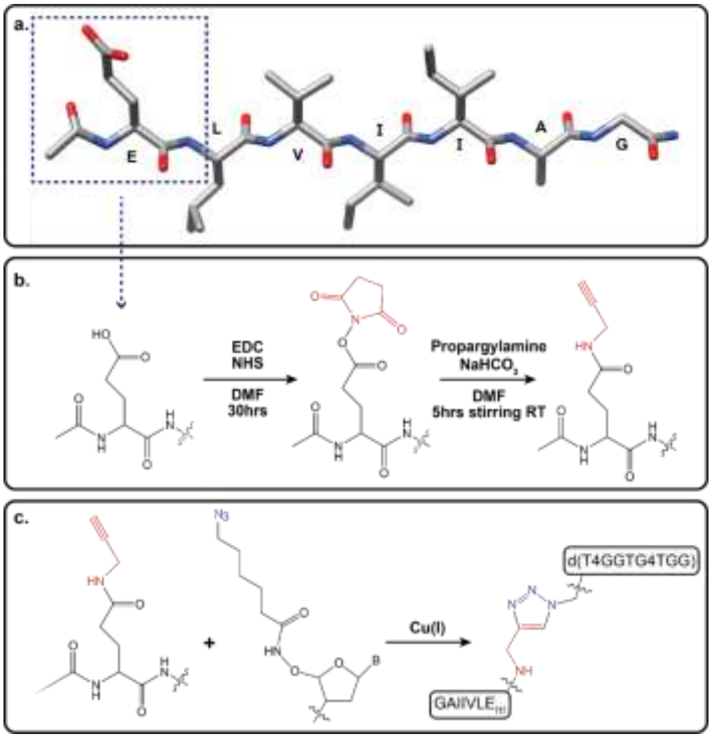

Scheme 4.1. Alkynylation of terminal glutamic acid (Ac-EmLVIIAG-NH$_2$) and click reaction with azide-modified guanine quadruplex DNA (d(T4GGTG4TGG). Primary peptide sequence for Ac-ELVIIAG-NH2. Dotted box outlines terminal glutamic acid residue (**a**). Alkyne modification of carboxylic acid moiety of terminal glutamate via amide linkage (Ac-EmLVIIAG-NH2, where "m" denotes modification of glutamate) (**b**). Cu(I) catalyzed click reaction of Ac-EmLVIIAG-NH2 and 5'-azide-modified ssDNA (d(T4GGTG4TGG)) gave the guanine quadruplex peptide conjugate (GQPC) through triazole formation (**c**).

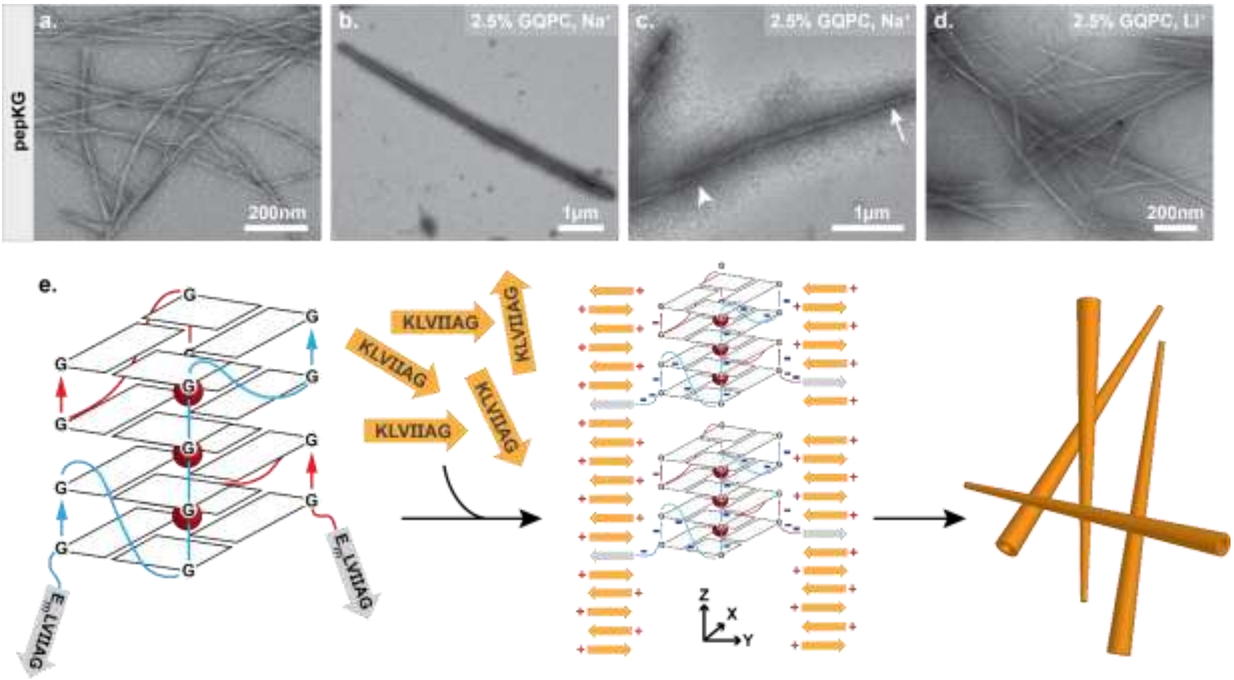

Figure 4.7. Guanine quadruplex folding is necessary for tapered nanotube morphology. Pep-KG (0.4 mM) assembled in sodium phosphate buffer results in bundled fiber formation (**a**). Co-assembly of GQPC (2.5% molar equivalent) and pep-KG (0.4mM) yields tapered conical assemblies resembling nanotubes in sodium phosphate buffer (**b**). Like previously described nanotubes, GQPC/Pep-KG co-assemblies form ribbons first. The tapered ends of GQPC/pep-KG co-assemblies close first (tapered end, arrow; wide end, arrowhead) (**c**). LiPO4 buffer used in place of NaPO4 resulted in a mixture of both non-tapered nanotubes and fibers (**d**), suggesting that GQ formation is essential for conical tube morphology as depicted in the proposed co-assembly mechanism (**e**).

The resulting conical nanotube is distinct from the multilamellar nanotubes found with ssDNA, dsDNA, or TMP templates. Most notably, the chimeric template nucleated GQPC/Pep-KG co-assembly at low concentrations (10 μM GQPC) and formed nanotubes with a width greater than that observed for either the ssDNA or dsDNA template visualized by TEM. Cross-β nanotube assemblies arise from growth along the lamination (sheet stacking) axis as well as the β-sheet H-bonding axis, and the covalently attached GQ-DNA was designed to impact nucleation along both growth axes by favoring initial GQ assembly.[19, 51] We hypothesize that early selection for guanine quadruplex formation coupled with low GQPC concentration, positioned GQPC conjugates at the tapered end of mature conical assemblies and facilitated further GQPC/Pep-KG templating. Future studies will be required to further elucidate the structural characteristics of the GQPC/Pep-KG co-assemblies. In addition to favored GQ formation, the sodium phosphate buffer may promote nanotube assembly through neutralization of the leaflet interface, similar to the previous study by Li et al. where salt passivation of nanotube bilayers was documented.[52] Electrostatic force microscopy (EFM) of GQPC/Pep-KG co-assemblies was consistent with a strong positive external surface charge for the tapered nanotubes, placing the positive N-terminal lysine of Pep-KG on the surface and sequestration of the quadruplex DNA within the nanotube interior (Figure S9).

GQPC/Pep-KG nanotubes contain strong peptide β-sheet CD signatures (Figure S4), however the GQ seeds are below the limit of detection, thus fluorescent spectroscopy was used to probe GQ formation. As shown in Figure 4.8, when combined with GQPC/Pep-KG co-assemblies the quadruplex-specific fluorophore ISCH-oa1 gives a 16-fold increase in fluorescence over Pep-KG assemblies or dye alone and a 4-fold increase in fluorescence over a dsDNA control.[53] Unlike sodium phosphate, lithium does not stabilize quadruplex assembly, and co-assembly of GQPC/Pep-KG in lithium phosphate buffer results in heterogeneous, thin-walled nanotubes and fibers without conical tube tapering (Figure 4.7D).[48, 54] Altogether, these results support the incorporation of GQPC and assembly of parallel GQs within the conical GQPC/Pep-KG co-assemblies (Figure 4.7E).

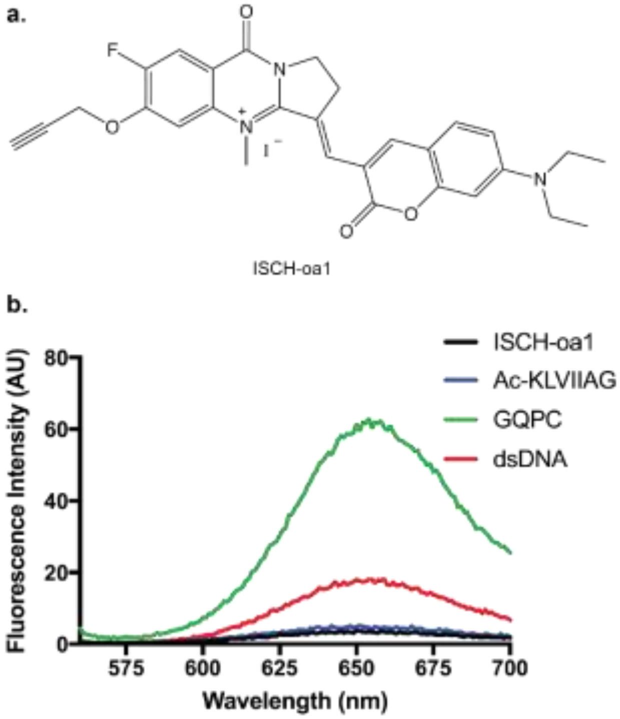

Figure 4.8. Guanine quadruplexes are present in GQPC/Pep-KG tapered nanotubes. ISCH-oa1 (**a**) was used as a fluorescent marker of guanine quadruplex folding and presence in conical co-assemblies. In the presence of GQ, ISCH-oa1 showed a marked fluorescence increase relative to ISCH-oa1 alone or in the presence of other DNA moieties (**b**). GQPC indicates GQPC/Pep-KG co-assemblies formed in the presence of Na+. Ac-KLVIIAG indicates Pep-KG alone.

Conclusion

Varying ATP concentrations in cells can work to control protein condensation,[33, 55, 56] and biphasic control of PLD proteins like FUS in membraneless compartments relies on electrostatic and π-cation interactions that, in a concentration-dependent manner, both condenses and dissolves protein condensates.[17, 55] Phosphate salts are also strongly kosmotropic and are known to induce crystalline order in other biomolecular condensates.[57] Furthermore, previous work has used the nucleating core of the Aβ peptide of Alzheimer's disease as a scaffold to elucidate the importance of electrostatic interactions in nucleic acid/amyloid co-assembly.[27] This motif forms an initial biomolecular condensate which biases conformational sampling, enabling both self-templating and pre-organization of the condensate for external templated assembly.[42, 58] Most interestingly, while ssDNA and RNA effectively templated precise peptide ordering, the nucleic acid had no higher-order structure and this motivated our investigation of more ordered templates. Based on this evidence, a minimal model was developed to explore the importance of polyanion structural ordering in the formation and selection of nuclei during liquid to solid transitions.

Our model system now establishes that structured nucleic acid assemblies provide a significantly lower threshold for effective templating as well as a framework for exploring the structural rules underpinning the early dynamics of membraneless organelles. Specifically, we found that the different ordering of phosphate groups on a polyanionic template modulates the liquid to solid phase transition from coacervate droplets to paracrystalline assemblies, either accelerating the formation of a stable nucleus which propagates out of the condensate or totally altering which nucleus is selected for within the condensate. This finding highlights the versatility of the cross-β architecture in accommodating various single-stranded and higher-order nucleic acid structures. Furthermore, our experiments with non-stoichiometric amounts of peptide-DNA chimera allow for seeding of distinct structures beyond co-assemblies, effectively separating nucleation with environmental agents from propagation. Finally, in the rapidly evolving field of biomaterials, the utilization of a specific material for nucleation and a different monomer for paracrystalline assembly propagation may provide avenues for design and incorporation of unique functional sites along amyloid-mimetic materials.

Materials and Methods

Synthesis of Ac-KLVIIAG-NH_2 (Pep-KG) and Ac-ELVIIAG-NH_2 (Pep-EG)

Pep-KG was synthesized on Rink amide-MBHA (Anaspec) solid support via a CEM Liberty Blue Automated Microwave Peptide Synthesizer (Serial # LB2447) with 1M N,N′-Diisopropyl carbodiimide (DIC; CAS# 693-13-6 AAPPTEC) as the activator, Oxyma Pure (CAS# 3849-21-6 CEM) as the activator base, and 20% Piperidine (CAS# 110-89-4 Sigma-Aldrich) as the deprotection solution. Amino acids were coupled using 0.25 mmol standard coupling (75°C 210W for 15s followed by 90°C 30W for 110s) and deprotected using 0.25 mmol standard deprotection (75°C 175W 15s, 90°C 30W 50s). The amino acids used were as follows: fmoc-boc-lysine, fmoc-leucine, fmoc-valine, fmoc-isoleucine, fmoc-alanine, fmoc-glycine, and fmoc-glutamic acid, and each one dissolved in dimethylformamide (DMF; CAS# 68-12-2 Sigma-Aldrich). The N-terminus was acetylated with a 20% acetic anhydride (CAS# 108-24-7 Sigma-Aldrich) in DMF solution and the 0.25 mmol N-terminal acetylation method (60°C 50W 30s, 25°C 0W 30s, 60°C

50W 30s, 25°C 0W 30s). Upon completion of synthesis, the resin beads were rinsed with dichloromethane (DCM) then let dry via vacuum filtration for cleavage from solid support which was carried out using a cocktail of 9:0.5:0.3:0.2 ratios of trifluoroacetic acid (TFA CAS# 76-05-1 Chem Impex)/thioanisole (CAS# 100-68-5 Sigma-Aldrich)/1,2-ethanedithiol (CAS# 540-63-6 Sigma-Aldrich)/anisole (CAS# 100-66-3 Sigma-Aldrich), where 10 mL of the cocktail was used in each of two vials and the 0.25 mmol of peptide attached to resin was evenly distributed across the two vials. The resin beads were submerged in the cocktail and were continuously perturbed using an orbital shaker at low intensity for to allow for homogeneous coverage of the beads with the cleaving reagents, and the reaction vessels were left for 3 hours at room temperature. Upon completion, the beads are filtered from the peptides via gravity filtration immediately into cold (-20°C) ether (CAS# 60-29-7 Fischer Scientific). At this point, the ether should become warm and cloudy due to mass precipitation of the peptides, and the mixture is then spun down at 4000 RCF for 15 minutes at 4°C to improve precipitation. The ether supernatant was discarded, and the gel-like pellet was washed with more cold ether for centrifugation, a process that is repeated twice more. The pellet was stored in vacuo pending HPLC purification and then a desalting protocol using a reverse phase Sep-Pak column.

Preparation of GQ/Pep-KG conjugate

Desalted Pep-EG (20 mg) and 33.5 mg N-hydroxysuccinimide (CAS# 6066-82-6 Sigma-Aldrich) were dissolved in minimal amount of DMF (approximately 2 mL). 55.8 mg EDC (1-Ethyl-3-(3-dimethylaminopropyl)carbodiimide; CAS# 25952-53-8 Sigma-Aldrich) was added afterward, and the solution were left to stir at room temperature overnight, up to 36 hours. Completion of this reaction generated an imide-peptide species at 851 Da

(Figure S1). 100 μL 0.2M NaHCO3 was then added to the solution, and 0.15 mmol propargylamine (CAS# 2450-71-1 Sigma-Aldrich) was added immediately after the pH was raised. This reaction was left to stir for 5 hours and propargylamine coupling, which generates Ac-EmLVIIAG-NH2, was confirmed via mass spectrometry (Figure S2). This crude product was used without further purification for conjugation with 5'-azide modified GQ DNA (T4GGTG4TGG) via azide-alkyne click reaction using 4 nmol GQ DNA, excess of Ac-EmLVIIAG-NH2 (4 μL), 4 μL 2M triethylamine-acetate buffer at pH 7, and 4 μL of saturated ascorbic acid for activation of 10mM Cu(II)-TBTA in 55% aqueous DMSO (Lumiprobe, MD, USA) was added last (4 μL). This reaction was run at room temperature for up to 48 hours and the peptide/DNA conjugate was precipitated with ethanol. Despite the excess of peptide, only peptide/DNA conjugates were recovered using this protocol involving 2 mL of 2M MgCl2 and a fourfold excess of 200 proof ethanol. The solution was shaken vigorously prior to placing in an ice bath for one hour. As the solution became turbid during the incubation period, the sample was spun down at 13,000 rpm for 20 minutes to give a gel-like pellet. After decanting the supernatant, the pellet was resuspended and washed with 70% ethanol and then spun down once more at 13,000 rpm for 10 minutes to give the peptide/DNA chimera. The ethanol was decanted, the pellet was analyzed by Urea-PAGE electrophoresis and mass spectroscopy, and the final sample was stored in vacuo until co-assembly with Pep-KG.

Assembly of Pep-KG with and without templates

All assembled samples were prepared using desalted Pep-KG following HPLC purification. Pep-KG was assembled at a final concentration of 1 mM both in the presence and the absence of polyanionic templates. Templates were added to satisfy a 1:1 charge ratio with

Pep-KG, which contributes a single positive charge. Assemblies were done with the following charge assumptions: the Drew-Dickerson dodecamer single stranded sequence d(CGCGAATTGCGC) contributed a charge of -12, whereas the double stranded counterpart of the same sequence had -24 charges. Both dA3 and trimetaphosphate contributed a -3 charge each. A solution of double the concentration of each template, relative to the template's final concentration, was prepared using 40% MeCN, where an equal volume of 2 mM Pep-KG in 40% MeCN was then added to the template solutions that were pre-incubated at 37°C. As an example, an initial solution of 400 µL 0.66 mM trimetaphosphate was prepared in 40% MeCN, where 400 µL 2 mM Pep-KG in 40% MeCN was added to it. All samples were incubated at 37°C throughout the assembly times of up to 2 weeks.

ThT fluorescence assay

Samples for Thioflavin T fluorescence analyses were prepared by combining 74 µL of each sample, 100 µL of 40% acetonitrile, and 1 µL of 10 mM Thioflavin T (CAS# 2390-54-7 purchased from Sigma-Aldrich) and measured in the wells of a 96 well plate (Microplate, 96 well, PS, F-bottom, µCLEAR, black, med. binding, Greiner Bio-one). Thioflavin T fluorescence was determined with a BioTek Synergy Mx plate reader (Serial# 250843) every 15 minutes for up to 24 hours, with short shaking before each read. The excitation wavelength was 444 nm and fluorescence was measured at 484 nm. A well containing 1 µL 10 mM ThT in 40% MeCN and 174 µL 40% MeCN was used as a baseline. The plate was held at 37°C for all 24 hours.

Sample preparation for TEM imaging

Each selected sample (8 µL) was pipetted onto a carbon-film coated, 200 mesh copper grid (CF200-Cu purchased from Electron Microscopy Services) The sample was then negative stained with 8 µL of the supernatant of a 2% w/v Uranyl acetate in water solution that had been centrifuged at 12,000 RCF for 10 minutes (CAS# 541-09-3 purchased from Electron Microscopy Solutions). Loaded electron microscopy grids were visualized with a Hitachi HT7700 transmission electron microscope at 80 kV.

Sample preparation for EFM imaging

Aliquots (10 µL) of GQPC assemblies in 40% acetonitrile were deposited on gold film upon Si/SiO2 substrate and then dried over 12 hours. All micrographs were taken by Park System XE-100 AFM in tapping mode. To probe for charge surface of our assemblies, a charge bias of +1 V was applied between the electrically conductive Pt-Ir coated tip, with 2.7 N/m force constant, (Mountain View, CA, AppNano) and the sample.

Characterization of assemblies via CD spectroscopy

Circular Dichroism (CD) analyses were recorded on a Jasco-810 Spectropolarimeter. Samples were micro-pipetted onto a 50µL Hellma Analytics quartz cell with a 0.1 mm path length (Model # 106-0.10-40). Spectra were measured by averaging 3 scans from 260-190 nm with a 0.2 nm data pitch and 100 nms-1 scanning speed. Molar ellipticity was calculated with the equation $[\theta] = \theta/(10 \times c \times l)$ where c is the peptide concentration in moles/L and l is the pathlength of the cuvette (cm).

CD melting experiments

43 µL of each sample was loaded onto a 50 µL Hellma Analytics quartz cell with 0.1 mm path length (Model # 106-0.10-40) while taking care to minimize bubbles inside the

cuvette, and the edge of the cuvette was wrapped in parafilm to minimize evaporation. Each melting trial was conducted using a Jasco J-1500 (Serial # B043361638) Spectropolarimeter starting at 37°C and ending at 92°, changing 1°C every minute and accumulating 3 scans from 260-190 nm every 5°C interval. The data pitch was 0.2 nm, the scanning speed used was 200 nm min-1.

Fluorescence spectroscopy for analyzing ISCH-oa1 binding

ISCH-oa1 were all measured at 1 μM final concentration, both in the presence and in the absence of peptides or GQ DNA. Each sample was measured in 3 mm path length quartz cuvette (Müllheim, Germany, Hellma Analytics) using Cary Eclipse Fluorescence Spectrophotometer (Santa Clara, CA, Agilent). Excitation was set to 550 nm, and emission spectra were acquired from 560 nm to 700 nm. Raw data were normalized to f/f0, where f is fluorescence of each sample, and f0 is fluorescence of ISCH-oa1 probe at 1 μM concentration.

Supplementary figures

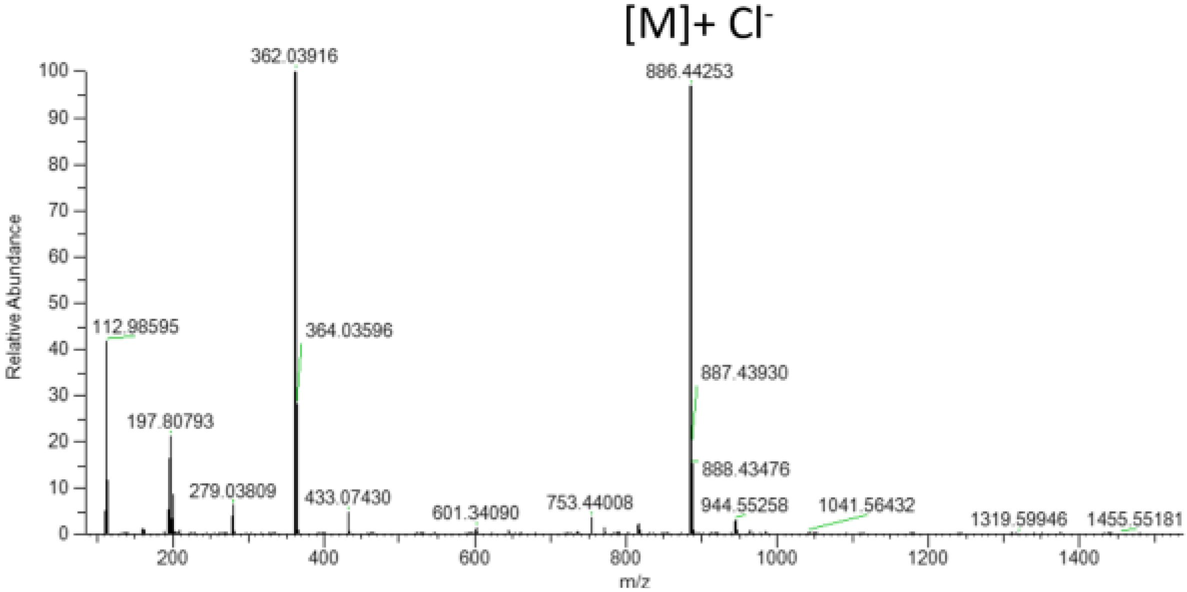

Figure S1. ESI spectra of peptide imide product generated by EDC/NHS coupling with Pep-EG

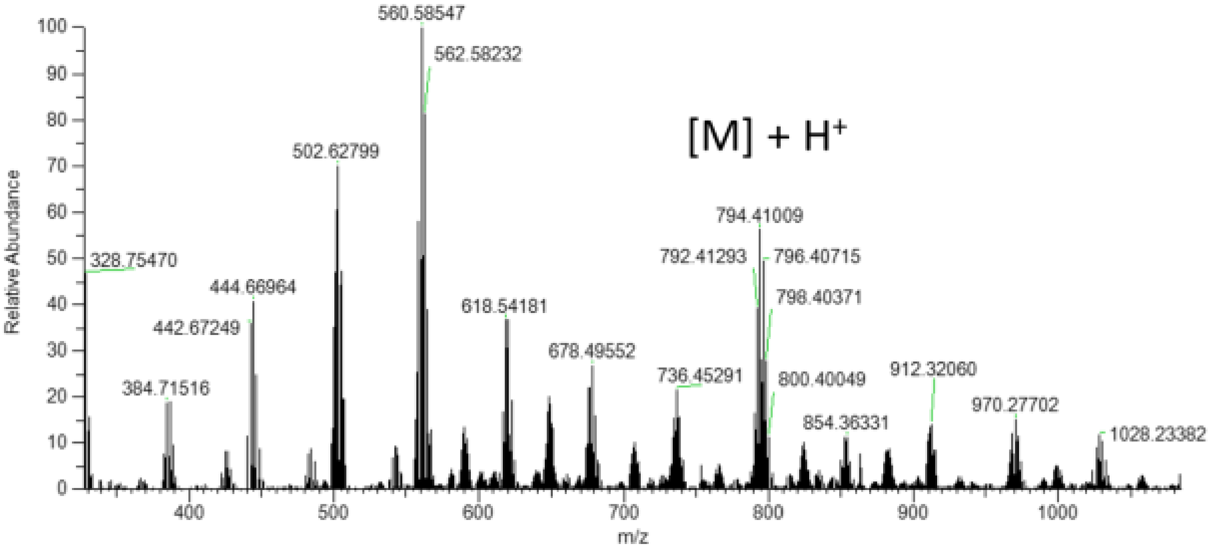

Figure S2. ESI spectra of alkynylated pep-EG after reacting crude imide peptide with propargylamine

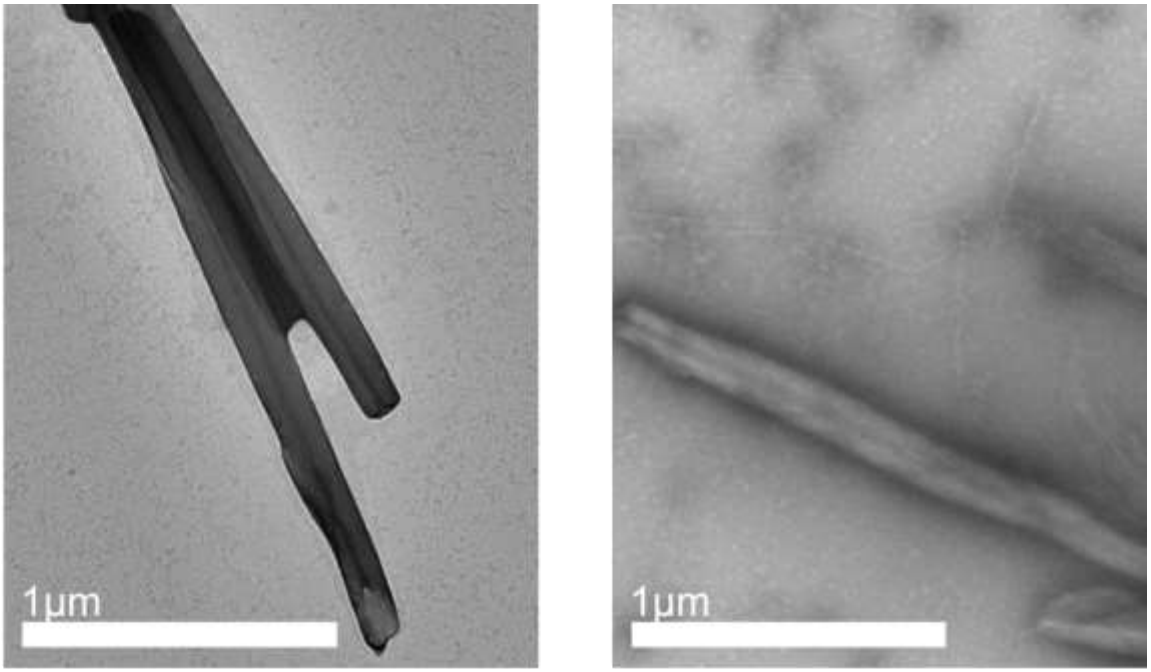

Pep-KG/TMP Pep-KG/dsDNA

Figure S3. (left) Co-assembly of pep-KG (1 mM) with sodium trimetaphosphate (TMP, 333 μM). (right) Co-assembly of pep-KG with dsDNA (41.7 μM). Both figures show thick-walled nanotube morphology.

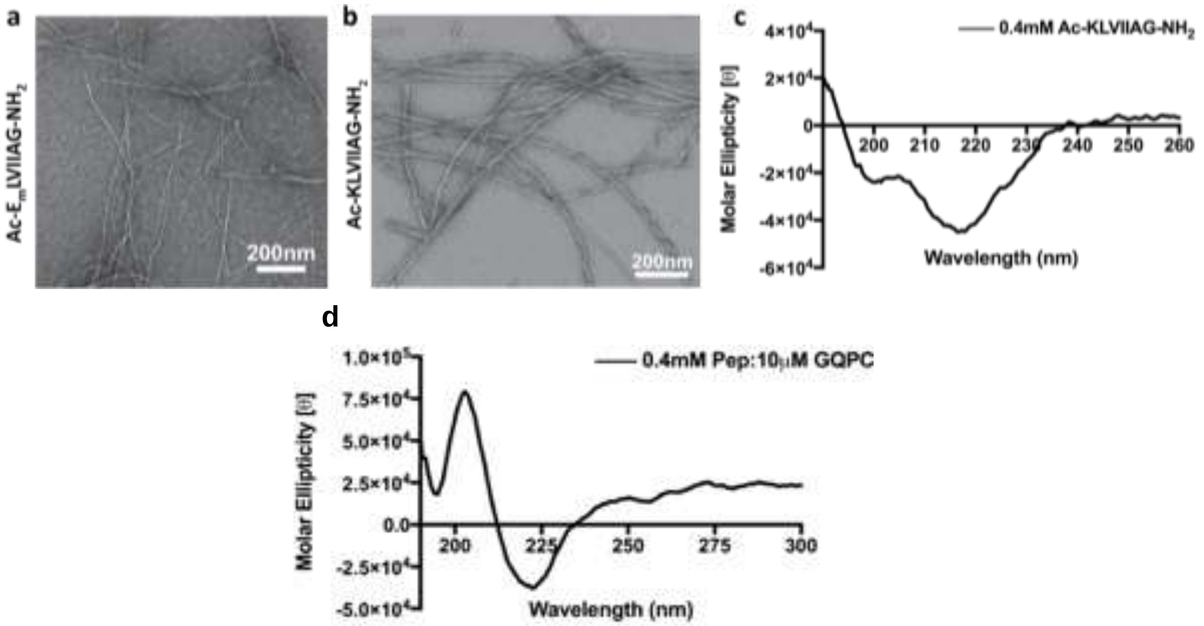

Figure S4. TEM images of assembled Ac-E$_m$LVIIAG-NH$_2$ (a) and pep-KG (b) showing fiber morphology. c. CD spectra of pep-KG at slightly above its critical peptide assembly concentration of 0.3 mM. d. CD spectra of GQPC/pep-KG, a pep-KG assembly seeded with 2.5% GQPC relative to overall pep-KG concentration.

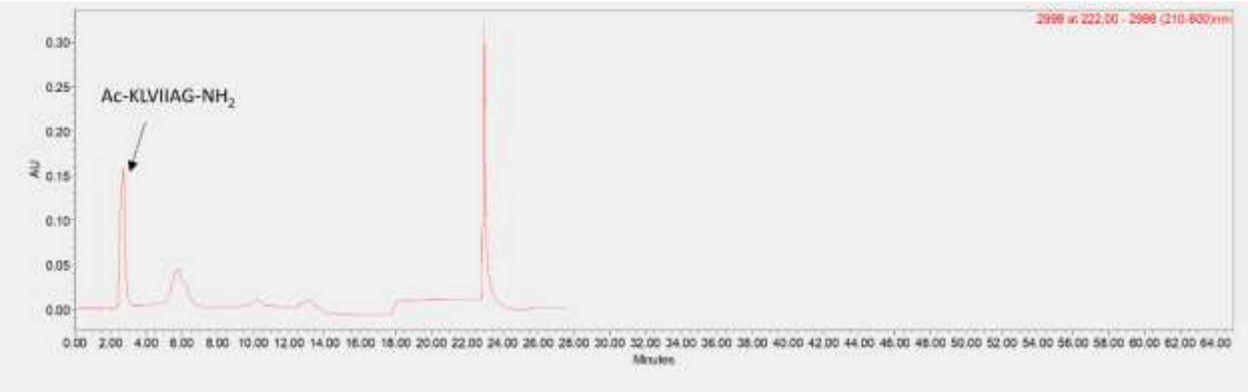

Figure S5. HPLC purification of Ac-KLVIIAG-NH$_2$, where the peptide elutes at 31% acidic MeCN

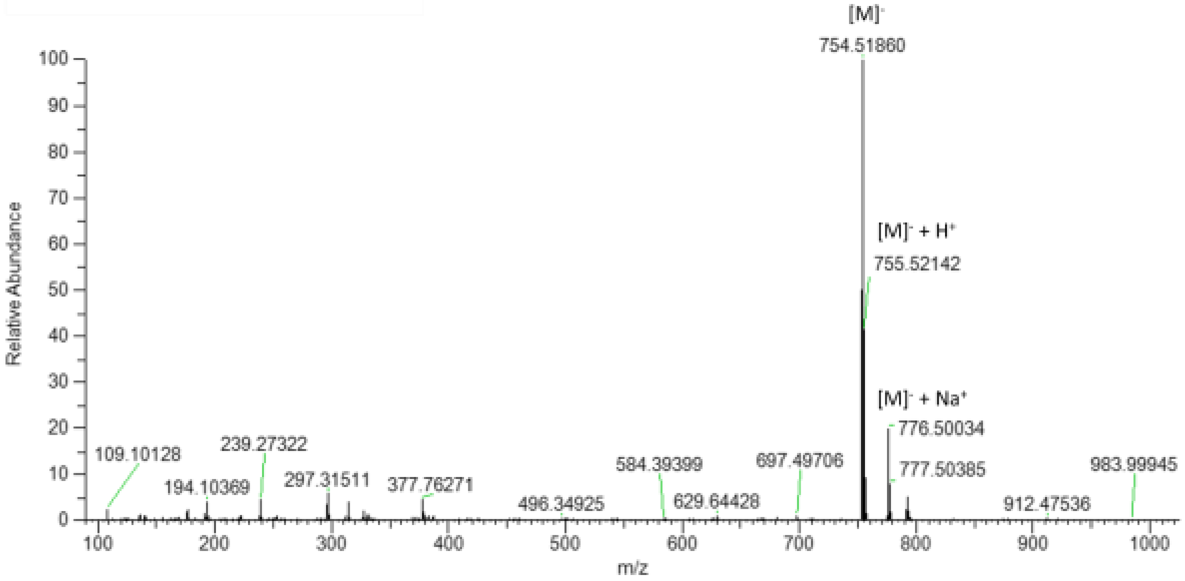

Figure S6. ESI spectra of Ac-KLVIIAG-NH$_2$ after HPLC purification

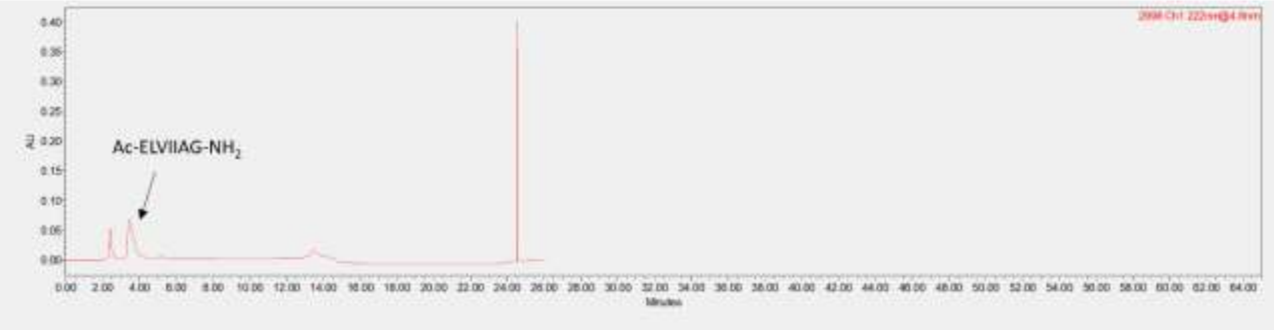

Figure S7. HPLC purification of Ac-ELVIIAG-NH$_2$, where the peptide elutes at 29% MeCN

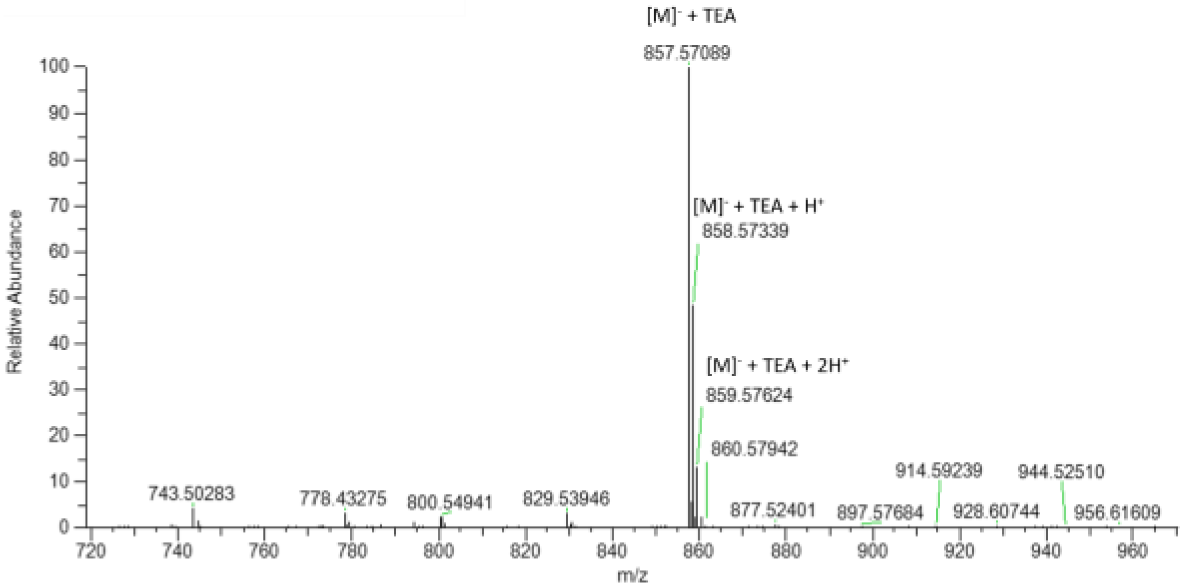

Figure S8. ESI spectra of Ac-ELVIIAG-NH_2 after HPLC purification

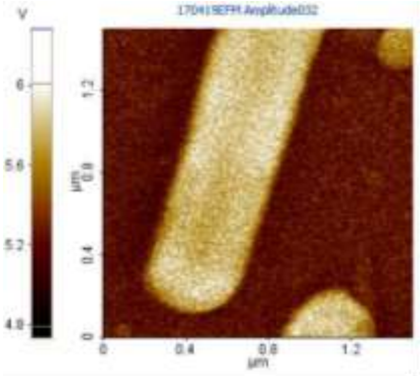

Figure S9. EFM of mature GQPC/Pep-KG co-assemblies.

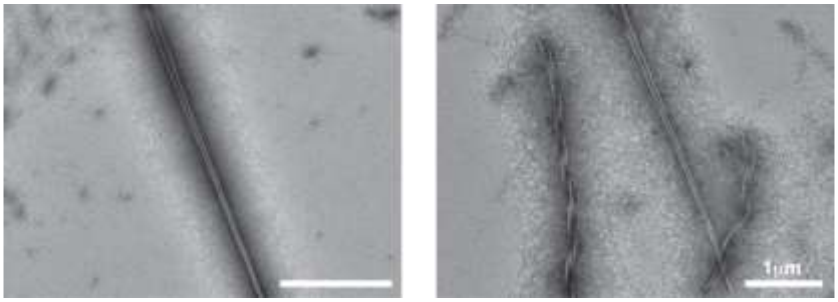

Figure S10. TEM images of GQPC/pep-KG assembled in 40% MeCN at 37°C after 7 day incubation.

References

1. Rosenow, C., et al., *Prokaryotic RNA preparation methods useful for high density array analysis: comparison of two approaches*. Nucleic Acids Research, 2001. **29**(22): p. e112-e112.
2. Deng, Z.-L., et al., *Rapid and accurate identification of ribosomal RNA sequences via deep learning*. Nucleic Acids Research, 2022. **50**(10): p. e60-e60.
3. Waldron, C. and F. Lacroute, *Effect of growth rate on the amounts of ribosomal and transfer ribonucleic acids in yeast*. Journal of Bacteriology, 1975. **122**(3): p. 855-865.
4. Khong, A., et al., *The Stress Granule Transcriptome Reveals Principles of mRNA Accumulation in Stress Granules*. Mol Cell, 2017. **68**(4): p. 808-820 e5.
5. Tauber, D., G. Tauber, and R. Parker, *Mechanisms and Regulation of RNA Condensation in RNP Granule Formation*. Trends Biochem Sci, 2020. **45**(9): p. 764-778.
6. Alberti, S., et al., *Granulostasis: Protein Quality Control of RNP Granules*. Front Mol Neurosci, 2017. **10**: p. 84.
7. Shin, Y. and C.P. Brangwynne, *Liquid phase condensation in cell physiology and disease*. Science, 2017. **357**(6357).
8. Alberti, S., A. Gladfelter, and T. Mittag, *Considerations and Challenges in Studying Liquid-Liquid Phase Separation and Biomolecular Condensates*. Cell, 2019. **176**(3): p. 419-434.
9. Banani, S.F., et al., *Biomolecular condensates: organizers of cellular biochemistry*. Nat Rev Mol Cell Biol, 2017. **18**(5): p. 285-298.

10. Gordon, C.K., R. Luu, and D. Lynn, *Capturing nested information from disordered peptide phases*. Peptide Science, 2021. **113**(2): p. e24215.

11. Conicella, A.E., et al., *TDP-43 alpha-helical structure tunes liquid-liquid phase separation and function*. Proc Natl Acad Sci U S A, 2020. **117**(11): p. 5883-5894.

12. Carey, J.L. and L. Guo, *Liquid-Liquid Phase Separation of TDP-43 and FUS in Physiology and Pathology of Neurodegenerative Diseases*. Front Mol Biosci, 2022. **9**: p. 826719.

13. Hallegger, M., et al., *TDP-43 condensation properties specify its RNA-binding and regulatory repertoire*. Cell, 2021. **184**(18): p. 4680-4696 e22.

14. Boeynaems, S., et al., *Spontaneous driving forces give rise to protein-RNA condensates with coexisting phases and complex material properties*. Proc Natl Acad Sci U S A, 2019. **116**(16): p. 7889-7898.

15. Dutagaci, B., et al., *Charge-driven condensation of RNA and proteins suggests broad role of phase separation in cytoplasmic environments*. eLife, 2021. **10**: p. e64004.

16. Wang, J., et al., *A Molecular Grammar Governing the Driving Forces for Phase Separation of Prion-like RNA Binding Proteins*. Cell, 2018. **174**(3): p. 688-699.e16.

17. Ren, C.-L., et al., *Uncovering the molecular mechanism for dual effect of ATP on phase separation in FUS solution*. Science Advances, 2022. **8**(37): p. eabo7885.

18. Hsieh, M.C., et al., *Multistep Conformation Selection in Amyloid Assembly*. J Am Chem Soc, 2017. **139**(47): p. 17007-17010.

19. Mehta, A.K., et al., *Facial symmetry in protein self-assembly*. J Am Chem Soc, 2008. **130**(30): p. 9829-35.

20. Childers, W.S., et al., *Phase networks of cross-beta peptide assemblies*. Langmuir, 2012. **28**(15): p. 6386-95.

21. Mehta, A.K., et al., *Context dependence of protein misfolding and structural strains in neurodegenerative diseases*. Peptide Science, 2013. **100**(6): p. 722-730.

22. Liang, C., et al., *Kinetic Intermediates in Amyloid Assembly*. Journal of the American Chemical Society, 2014. **136**(43): p. 15146-15149.

23. Uversky, V.N., *Intrinsic disorder-based protein interactions and their modulators*. Curr Pharm Des, 2013. **19**(23): p. 4191-213.

24. Mollica, L., et al., *Binding Mechanisms of Intrinsically Disordered Proteins: Theory, Simulation, and Experiment*. Front Mol Biosci, 2016. **3**: p. 52.

25. Arai, M., et al., *Conformational propensities of intrinsically disordered proteins influence the mechanism of binding and folding*. Proceedings of the National Academy of Sciences, 2015. **112**(31): p. 9614-9619.

26. Kim, D.H. and K.H. Han, *PreSMo Target-Binding Signatures in Intrinsically Disordered Proteins*. Mol Cells, 2018. **41**(10): p. 889-899.

27. Rha, A.K., et al., *Electrostatic Complementarity Drives Amyloid/Nucleic Acid Co-Assembly*. Angew Chem Int Ed Engl, 2020. **59**(1): p. 358-363.

28. Hsieh, M.C., D.G. Lynn, and M.A. Grover, *Kinetic Model for Two-Step Nucleation of Peptide Assembly*. J Phys Chem B, 2017. **121**(31): p. 7401-7411.

29. Brazda, V., et al., *Cruciform structures are a common DNA feature important for regulating biological processes*. BMC Mol Biol, 2011. **12**: p. 33.

30. Flores, J.K. and S.F. Ataide, *Structural Changes of RNA in Complex with Proteins in the SRP*. Front Mol Biosci, 2018. **5**: p. 7.

31. Chilinski, M., K. Sengupta, and D. Plewczynski, *From DNA human sequence to the chromatin higher order organisation and its biological meaning: Using biomolecular interaction networks to understand the influence of structural variation on spatial genome organisation and its functional effect*. Semin Cell Dev Biol, 2022. **121**: p. 171-185.
32. Sanchez de Groot, N., et al., *RNA structure drives interaction with proteins*. Nat Commun, 2019. **10**(1): p. 3246.
33. Saurabh, S., et al., *ATP-responsive biomolecular condensates tune bacterial kinase signaling*. Science Advances, 2022. **8**(7): p. eabm6570.
34. Marky, L.A., et al., *Salt-dependent conformational transitions in the self-complementary deoxydodecanucleotide d(CGCAATTCGCG): evidence for hairpin formation*. Biopolymers, 1983. **22**(4): p. 1247-57.
35. Dickerson, R.E. and H.R. Drew, *Kinematic model for B-DNA*. Proc Natl Acad Sci U S A, 1981. **78**(12): p. 7318-22.
36. Drew, H.R. and R.E. Dickerson, *Structure of a B-DNA dodecamer. III. Geometry of hydration*. J Mol Biol, 1981. **151**(3): p. 535-56.
37. Dickerson, R.E. and H.R. Drew, *Structure of a B-DNA dodecamer. II. Influence of base sequence on helix structure*. J Mol Biol, 1981. **149**(4): p. 761-86.
38. Drew, H.R., et al., *Structure of a B-DNA dodecamer: conformation and dynamics*. Proc Natl Acad Sci U S A, 1981. **78**(4): p. 2179-83.
39. Chang, L.-W., et al., *Sequence and entropy-based control of complex coacervates*. Nature Communications, 2017. **8**(1): p. 1273.
40. Peyrard, M., S. Cuesta-Lopez, and G. James, *Nonlinear analysis of the dynamics of DNA breathing*. J Biol Phys, 2009. **35**(1): p. 73-89.

41. Leroy, J.L., et al., *Characterization of base-pair opening in deoxynucleotide duplexes using catalyzed exchange of the imino proton*. J Mol Biol, 1988. **200**(2): p. 223-38.

42. Rengifo, R.F., et al., *Liquid-Like Phases Preorder Peptides for Supramolecular Assembly*. ChemSystemsChem, 2020. **2**(6): p. e2000007.

43. Wen, J., et al., *Hofmeister series and ionic effects of alkali metal ions on DNA conformation transition in normal and less polarised water solvent*. Molecular Physics, 2014. **112**(20): p. 2707-2719.

44. Do, N.Q., et al., *G-quadruplex structure of an anti-proliferative DNA sequence*. Nucleic Acids Res, 2017. **45**(12): p. 7487-7493.

45. Ahmed, S., et al., *Formation of G-wires, bimolecular and tetramolecular quadruplex: Cation-induced structural polymorphs of G-rich DNA sequence of human SYTX gene*. Biopolymers, 2018. **109**(5): p. e23115.

46. Ilc, T., et al., *Formation of G-Wires: The Role of G:C-Base Pairing and G-Quartet Stacking*. The Journal of Physical Chemistry C, 2013. **117**(44): p. 23208-23215.

47. Kypr, J., et al., *Circular dichroism and conformational polymorphism of DNA*. Nucleic Acids Res, 2009. **37**(6): p. 1713-25.

48. Bhattacharyya, D., G. Mirihana Arachchilage, and S. Basu, *Metal Cations in G-Quadruplex Folding and Stability*. Front Chem, 2016. **4**: p. 38.

49. Hazel, P., et al., *Loop-length-dependent folding of G-quadruplexes*. J Am Chem Soc, 2004. **126**(50): p. 16405-15.

50. Vondruskova, J., et al., *Role of loops in the guanine quadruplex formation by DNA/RNA hybrid analogs of G4T4G4*. Int J Biol Macromol, 2008. **43**(5): p. 463-7.

51. Lu, K., et al., *Exploiting amyloid fibril lamination for nanotube self-assembly*. J Am Chem Soc, 2003. **125**(21): p. 6391-3.
52. Li, S., et al., *Design of Asymmetric Peptide Bilayer Membranes*. J Am Chem Soc, 2016. **138**(10): p. 3579-86.
53. Chen, S.B., et al., *Visualization of NRAS RNA G-Quadruplex Structures in Cells with an Engineered Fluorogenic Hybridization Probe*. J Am Chem Soc, 2016. **138**(33): p. 10382-5.
54. Venczel, E.A. and D. Sen, *Parallel and antiparallel G-DNA structures from a complex telomeric sequence*. Biochemistry, 1993. **32**(24): p. 6220-8.
55. Patel, A., et al., *ATP as a biological hydrotrope*. Science, 2017. **356**(6339): p. 753-756.
56. Aida, H., Y. Shigeta, and R. Harada, *The role of ATP in solubilizing RNA-binding protein fused in sarcoma*. Proteins: Structure, Function, and Bioinformatics, 2022. **90**(8): p. 1606-1612.
57. Malay, A.D., et al., *Spider silk self-assembly via modular liquid-liquid phase separation and nanofibrillation*. Sci Adv, 2020. **6**(45).
58. Chen, C., et al., *Design of multi-phase dynamic chemical networks*. Nature Chemistry, 2017. **9**(8): p. 799-804.

Chapter 5: Concluding remarks

Therapeutic advancements in modern medicine are often preceded by the elucidation of disease progression and physiological response in animal models. These observations were then used to extrapolate possible responses induced in their human counterparts. Therefore, the more closely related the model system is to humans, the stronger the degree of extrapolation, making non-human primates a gold standard to study diseases relevant to humans – from viral infections to addictions.[1-4] However, when it comes to AD pathology, nonhuman primate models fail to account for the link between proteinaceous plaque accumulations of Aβ42 and tau and the subsequent cognitive decline associated with AD phenotype. This disconnect drives the search for an alternative model system.

The novel development of an iPSC model for tracking AD pathology at its earliest timepoints was an exciting feature of this dissertation. Successful reproduction of global genotypic changes and a specific phenotypic profile associated with AD in otherwise "healthy" organoids not only suggest that iPSCs could be a suitable model for tauopathy but also that a cell-to-cell spread initiated by a propagating agent, a propagon, could be transferred *ex vivo*. Although this propagon has not yet been identified, some of its interactions with clinically known biomarkers such as Aβ42 and tau could pare down the list of potential candidates. Moreover, I have now shown strong evidence which suggests that Aβ42 and tau have the potential to mutualistically interact, amplifying the assembly propensity of the biopolymers. This interaction could be owed to the β-sheet motif that is mutually shared by each species, thus even minimalistic β-sheet versions of each polypeptide were sufficient enough to proliferate paracrystalline structures. While the experiments that probed the heterpolymer interactions focused on the purportedly nonpathological congener of tau or PHF6, future work involving both the full-length and the hypothetically pathogenic phosphorylated PHF6 would provide a clearer picture to possible mutualism in the disease context. Given that phosphorylation along the microtubule binding region, which contains both PHF6 and PHF6*, has been found to yield disease-linked tau-tau interactions, understanding whether Aβ42's effects on PHF6 could be swayed will give better insight to the disease state.[5-7]

Furthermore, the observation of apolipoprotein E, ApoE, complexes in isolates derived from real AD brain tissues was also a surprising insight, as many decades of AD research have been hinting at ApoE's possible role in the disease etiology.[8-12] While vast amounts of resources have been exhausted to target amyloid and tau assembly proliferation as therapeutic strategies with little clinical improvements or any improvements in disease prognosis, perhaps this finding could provide new insight to future neurodegenerative disease work that aims to target ApoE interactions. Current literature has shown some evidence for possible direct interactions between ApoE and Aβ42 that influences the latter's propensity for self-assembly.[11, 13, 14] These interactions have been attributed to specifically to lipid-free ApoE ε4 binding to Aβ42 precisely within the $A\beta42_{12\text{-}28}$ region, which includes the well-studied E22 motif that I have extensively characterized throughout this dissertation. Now that ApoE complexes have been observed in the AD brain tissue-derived isolates, probing synthetic ApoE and Aβ42 *in vitro* could also further dissect the link between the two species and their implications in the early disease state.

Additionally, findings that elucidate disease-relevant biopolymer associations also unraveled new rules which drive them. Generalized rules like the "sticker-spacer" model have informed the field of intrinsically disordered proteins on better prediction of disorder-to-order states by assigning residues as either a sticker that cross-links or a spacer that dictates spacing.[15] Such an overarching model had not yet been developed to predict distinct biopolymer interactions like proteins and nucleic acids. From the PHF6-Aβ42 experiments, I learned of a trend that peptide assemblies follow – that the ordering of the initial nucleus will influence the overall assembly pathway, and I applied this trend to a minimalistic peptide-oligonucleotide model system. Previous studies with Pep-KG and DNA strands of varying lengths showed that electrostatic complementarity between a positively charged lysine and a negatively charged phosphate group is the main driver for their mutualistic association. One caveat to the complementarity rule is that the oligonucleotide nucleus must possess more than 5 negatively charged phosphates, suggesting that there is a minimal threshold for mutualistic assembly. With oligonucleotide lengths being a preliminary criteria for nucleus ordering, I turned to another nucleus with charge ordering that is distinct from, so far, the linearly ordered oligonucleotides. Trimetaphosphate, with only 3 negative charges which are all attributed to the phosphate groups that are arranged in a 6-member ring, proved sufficient in nucleating mutualistic interactions with Pep-KG, something that a 3-base long oligonucleotide could not.[16] This suggests that, just like the homopolymer peptide interactions, heteropolymer mutualistic interactions can also be predicted by their seed.

Finally, although experiments with Pep-KG which could result in multilamellar nanotubes are less disease relevant, they still provide value to understanding overall biological mutualistic cross-talk. As one example, while there is now a strong link between Aβ42-rich plaques and the development of AD symptoms, little is known about any functional roles that Aβ42 may play.[17-19] There are few studies that show *in vitro* interactions of Aβ42 and DNA, showing that cross-talk is possible, but so far there have been no real way to predict such interactions.[20, 21] Studies with Pep-KG, which favor peptide-DNA interactions over peptide-peptide interactions, outline what such heteropolymer interactions could look like, narrowing down the possibilities. Furthermore, structural analysis of Aβ42 shows that the peptide adopts a cross-β architecture, a design that contributes to the overall plaque stability, and in the works described above, I have shown how structurally plastic this architecture could be – being able to accommodate salts and complex DNA structures alike. Findings like this can clarify the vague nature of what all could be involved in disease relevant paracrystalline formation. For example, while I have demonstrated the increased presence of highly ordered aggregates in AD brain tissue when compared to the healthy brain tissue, it is not yet clear whether the aggregates could exclusively consist of AD biomarkers like Aβ42 or a mixture of other biopolymers, which at this point cannot exclude oligonucleotides. The inclusion of other species, though, could be a result of their accommodation between the leaflet spacings, as I have shown with various forms of DNA, further expanding the possible roles of Aβ42 as a polyanion-binding polypeptide.

References

1. Weerts, E.M., W.E. Fantegrossi, and A.K. Goodwin, *The value of nonhuman primates in drug abuse research*. Exp Clin Psychopharmacol, 2007. **15**(4): p. 309-27.
2. Heuer, E., et al., *Nonhuman primate models of Alzheimer-like cerebral proteopathy*. Curr Pharm Des, 2012. **18**(8): p. 1159-69.
3. Singh, V.K. and A.O. Olabisi, *Nonhuman primates as models for the discovery and development of radiation countermeasures*. Expert Opin Drug Discov, 2017. **12**(7): p. 695-709.
4. Estes, J.D., S.W. Wong, and J.M. Brenchley, *Nonhuman primate models of human viral infections*. Nat Rev Immunol, 2018. **18**(6): p. 390-404.
5. Buée, L., et al., *Tau protein isoforms, phosphorylation and role in neurodegenerative disorders*. Brain Res Brain Res Rev, 2000. **33**(1): p. 95-130.
6. Gong, C.X. and K. Iqbal, *Hyperphosphorylation of microtubule-associated protein tau: a promising therapeutic target for Alzheimer disease*. Curr Med Chem, 2008. **15**(23): p. 2321-8.
7. Passarella, D. and M. Goedert, *Beta-sheet assembly of Tau and neurodegeneration in Drosophila melanogaster*. Neurobiol Aging, 2018. **72**: p. 98-105.
8. Frisoni, G.B., et al., *The prevalence of apoE-ε4 in Alzheimer's disease is age dependent*. Journal of Neurology, Neurosurgery & Psychiatry, 1998. **65**(1): p. 103-106.

9. LaDu, M.J., et al., *Apolipoprotein E and apolipoprotein E receptors modulate A beta-induced glial neuroinflammatory responses*. Neurochem Int, 2001. **39**(5-6): p. 427-34.

10. Liu, C.C., et al., *Apolipoprotein E and Alzheimer disease: risk, mechanisms and therapy*. Nat Rev Neurol, 2013. **9**(2): p. 106-18.

11. Kanekiyo, T., H. Xu, and G. Bu, *ApoE and Aβ in Alzheimer's disease: accidental encounters or partners?* Neuron, 2014. **81**(4): p. 740-54.

12. Huang, Y. and R.W. Mahley, *Apolipoprotein E: structure and function in lipid metabolism, neurobiology, and Alzheimer's diseases*. Neurobiol Dis, 2014. **72 Pt A**: p. 3-12.

13. Garai, K., et al., *The Binding of Apolipoprotein E to Oligomers and Fibrils of Amyloid-β Alters the Kinetics of Amyloid Aggregation*. Biochemistry, 2014. **53**(40): p. 6323-6331.

14. Liu, S., et al., *Targeting Apolipoprotein E/Amyloid β Binding by Peptoid CPO_Aβ17-21 P Ameliorates Alzheimer's Disease Related Pathology and Cognitive Decline*. Sci Rep, 2017. **7**(1): p. 8009.

15. Martin, E.W., et al., *Valence and patterning of aromatic residues determine the phase behavior of prion-like domains*. Science, 2020. **367**(6478): p. 694-699.

16. Gordon-Kim, C., et al., *Polyanion order controls liquid-to-solid phase transition in peptide/nucleic acid co-assembly*. Frontiers in Molecular Biosciences, 2022. **9**.

17. Johnstone, E.M., et al., *Conservation of the sequence of the Alzheimer's disease amyloid peptide in dog, polar bear and five other mammals by cross-species polymerase chain reaction analysis*. Brain Res Mol Brain Res, 1991. **10**(4): p. 299-305.

18. Roher, A.E., et al., *beta-Amyloid-(1-42) is a major component of cerebrovascular amyloid deposits: implications for the pathology of Alzheimer disease*. Proc Natl Acad Sci U S A, 1993. **90**(22): p. 10836-40.

19. Findeis, M.A., *The role of amyloid beta peptide 42 in Alzheimer's disease*. Pharmacol Ther, 2007. **116**(2): p. 266-86.

20. Camero, S., et al., *Specific binding of DNA to aggregated forms of Alzheimer's disease amyloid peptides*. Int J Biol Macromol, 2013. **55**: p. 201-6.

21. Maloney, B. and D.K. Lahiri, *The Alzheimer's amyloid β-peptide (Aβ) binds a specific DNA Aβ-interacting domain (AβID) in the APP, BACE1, and APOE promoters in a sequence-specific manner: Characterizing a new regulatory motif*. Gene, 2011. **488**(1): p. 1-12.